Effect of Ambient Oxidation on Chemical Composition and Structural Properties of Iron Nanoparticles for Hyperthermia and Medical Imaging

A Dissertation Presented for the
Doctor of Philosophy
Degree
The University of Tennessee, Knoxville

Adam Wesley Evans
December 2020

Copyright © 2020 by Adam Wesley Evans
All rights reserved.

DEDICATION

To my mother, who taught me strength

To my father, who taught me gentleness

To my brother, who taught me compassion

ACKNOWLEDGEMENTS

I would like to especially thank my academic advisor, Dr. Jacqueline Johnson, for her leadership and direction throughout my time at UTSI. She picked my application out of those bound for UT Knoxville and invited me to the Space Institute: a place I had not heard of before, but one that proved to be a great fit. She allowed me to travel the world in the name of science, and I am grateful for the opportunity she provided.

I would like to thank Drs. Saeed Kamali, Feng-Yuan Zhang, and Claudia Rawn for their participation in my Dissertation Committee. I greatly appreciate them taking the time to read this dissertation and offer their advice, critique, and input.

My knowledge of Mössbauer spectroscopy would be naught without the kind ear, expertise, and input from Dr. Charles Johnson. Thank you for the education and mentorship.

This work would not be possible without the assistance of the knowledgeable faculty and staff at UTSI. I would like to thank Doug Warnberg, Alexander Terekhov, Dr. Brain Canfield, Dr. Lino Costa, and Kathleen Lansford for their help in the Center for Laser Applications throughout my time at this institution.

My fellow groupmates have been my favorite part of the UTSI experience. I would like to thank Dr. Lee Leonard for the example he set and guidance he provided, Dr. Julie King for her diverse and delicious confections, immaculate organization skills and genuine friendship, Chad Bond for our Hawaii adventures and his sense of humor, Dr. Hien-Yoong Hah for the long discussions and impromptu Tullahoma meals, Austin Thomas for being partners during our China trip, Anna Bull for the desserts once Julie graduated and her cheerful disposition,

Aleia Williams for her attentive ear, and the numerous interns throughout the years for their genuine interest. I will reminisce on my time here fondly.

Finally, I would like to thank Dr. Adam Rondinone and Michelle Pawel at the Oak Ridge National Laboratory Center for Nanophase Material Science for providing lab space and expertise in nanoparticle synthesis during the first two years of this project.

ABSTRACT

With magnetization saturation roughly twice that of iron oxide nanoparticles, metallic iron nanoparticles (also termed zero-valent iron nanoparticles) have desirable properties for use as a magnetic resonance imagining (MRI) contrast agent as well as a medium for hyperthermia treatment of cancer. Metallic iron nanoparticles, however, are difficult to synthesize and maintain due to their high degree of reactivity and proclivity for oxidation. The main goal of this study was to investigate how ambient oxidation affects the chemical composition and structural properties of metallic iron nanoparticles initially synthesized through a facile reduction reaction of iron (III) chloride with sodium borohydride. A metallic iron nanoparticle with tunable oxidation would combine the biocompatibility of iron oxide with the magnetic strength of metallic iron.

Metallic iron nanoparticles were examined via transmission electron microscopy (TEM), scanning electron microscopy (SEM), dynamic light scattering (DLS), powder X-ray diffraction (XRD), and Mössbauer spectroscopy to determine their morphology and structure. Relaxometry experiments were conducted to investigate the potential of as-made metallic iron nanoparticles as an MRI contrast agent. Imaging data revealed nanoparticles in the range of 10-80 nm that are arranged as either spheroids or sintered aggregates. X-ray diffraction confirmed the presence of metallic iron, while Mössbauer measurements revealed core-shell nanoparticles containing a metallic iron core covered by amorphous iron and iron oxides. Oxide percentage increased as nanoparticles were left to age under ambient conditions. Oxidation rate slowed once an adequate passivation layer was formed. Polyethylene glycol (PEG) coating of nanoparticles retarded oxidation rate, thereby preserving the metallic iron content and desirable magnetic properties of the nanoparticles.

TABLE OF CONTENTS

Chapter I Introduction 1
Iron Oxide Nanoparticles vs Metallic Iron Nanoparticles 2
Metallic Iron Nanoparticle Applications 3
Magnetic Resonance Imaging (MRI) Contrast Agent 3
Hyperthermia 5
Previous Iron Nanoparticle Work at UTSI 8
Reduction of Iron (II) Chloride 9
Thermal Decomposition of Iron Pentacarbonyl 9
Summary of Work 10
Chapter II Experimental Methods 13
Iron Nanoparticle Synthesis 14
Syringe Pump Reduction of Iron (III) Chloride 14
Dropwise Reduction of Iron (III) Chloride 16
Sample Washing and Magnetic Separation 18
Vacuum Filtration 18
Nanoparticle Drying and Glovebox Storage 22
Ambient Oxidation of Metallic Iron Nanoparticles 26
Materials Characterization 26
Transmission Electron Microscopy 26
Scanning Electron Microscopy 26
X-ray Diffraction 28
Dynamic Light Scattering 28
Mössbauer Spectroscopy 31
Magnetic Resonance Relaxometry 31
Chapter III Results and Discussion 35
General Material Characterization 36
Transmission Electron Microscopy (TEM) 36
Scanning Electron Microscopy (SEM) 41
X-ray diffraction (XRD) 45
Dynamic Light Scattering (DLS) 48
General Mössbauer Spectroscopy 64
Mössbauer Spectroscopy Oxidation Time Studies 86
AE001: Syringe Pump $FeCl_3$ Reduction in Air 86
AE007: Dropwise $FeCl_3$ Reduction in Argon Flow 89
AE003: Syringe Pump $FeCl_3$ Reduction in Nitrogen Flow 90
AE013A/B: Syringe Pump $FeCl_3$ Reduction in Argon Flow with PEG Coating 96
AE014A/B: Syringe Pump $FeCl_3$ Reduction in Argon Flow with PEG Coating 103
Relaxometry 112
Chapter IV Conclusions 114
References 116
Appendix 122

Vita.....131

LIST OF TABLES

Table 1. Synthesis parameters and sample work up procedures used for each sample 19
Table 2. Iron nanoparticle crystallite size determined through Scherrer equation calculations 46
Table 3. Table of AE001 DLS results 51
Table 4. Table of AE003 as-made DLS results 52
Table 5. Table of AE004 DLS results 54
Table 6. Table of AE006 DLS results 55
Table 7. Table of AE007 DLS results 56
Table 8. Table of AE008 DLS results 57
Table 9. Table of AE009 DLS results 59
Table 10. Table of AE010 DLS results 60
Table 11. Table of AE011 DLS results 61
Table 12. Table of AE013B DLS results 62
Table 13. Table of AE014A DLS results 63
Table 14. Values of hyperfine parameters derived from fitting as-made AE001, AE002, and AE003 metallic iron nanoparticles post-synthesis. B_{hf} is the hyperfine magnetic field, δ is the isomer shift, ΔE_Q is the quadrupole splitting, and Γ is the linewidth (FWHM). Typical errors are ±0.5 mm/s for B_{hf}, ±0.02 mm/s for δ, ΔE_Q, and Γ and ±3% for relative area 66
Table 15. Values of hyperfine parameters derived from fitting as-made AE005, AE006, and AE011 metallic iron nanoparticles post-synthesis. B_{hf} is the hyperfine magnetic field, δ is the isomer shift, ΔE_Q is the quadrupole splitting, and Γ is the linewidth (FWHM). Typical errors are ±0.5 mm/s for B_{hf}, ±0.02 mm/s for δ, ΔE_Q, and Γ and ±3% for relative area 72
Table 16. Values of hyperfine parameters derived from fitting as-made AE007 and AE008 metallic iron nanoparticles post-synthesis. B_{hf} is the hyperfine magnetic field, δ is the isomer shift, ΔE_Q is the quadrupole splitting, and Γ is the linewidth (FWHM). Typical errors are ±0.03 mm/s for B_{hf}, ±0.5 mm/s for δ, ΔE_Q, and Γ and ±3% for relative area 75
Table 17. Values of hyperfine parameters derived from fitting as-made AE009 and AE010 metallic iron nanoparticles post-synthesis. B_{hf} is the hyperfine magnetic field, δ is the isomer shift, ΔE_Q is the quadrupole splitting, and Γ is the linewidth (FWHM). Typical errors are ±0.03 mm/s for B_{hf}, ±0.5 mm/s for δ, ΔE_Q, and Γ and ±3% for relative area 77
Table 18. Values of hyperfine parameters derived from fitting as-made AE013A and AE014A metallic iron nanoparticles post-synthesis. B_{hf} is the hyperfine magnetic field, δ is the isomer shift, ΔE_Q is the quadrupole splitting, and Γ is the linewidth (FWHM). Typical errors are ±0.5 mm/s for B_{hf}, ±0.02 mm/s for δ, ΔE_Q, and Γ and ±3% for relative area 81
Table 19. Values of hyperfine parameters derived from fitting as-made AE013B and AE014B metallic iron nanoparticles post-synthesis. B_{hf} is the hyperfine

magnetic field, δ is the isomer shift, ΔE_Q is the quadrupole splitting, and Γ is the linewidth (FWHM). Typical errors are ±0.03 mm/s for B_{hf}, ±0.5 mm/s for δ, ΔE_Q, and Γ and ±3% for relative area 84
Table 20. Values of hyperfine parameters derived from fitting AE001 metallic iron nanoparticles prepared at lengths of room temperature ambient oxidation. B_{hf} is the hyperfine magnetic field, δ is the isomer shift, ΔE_Q is the quadrupole splitting, and Γ is the linewidth (FWHM). Typical errors are ±0.03 mm/s for B_{hf}, ±0.5 mm/s for δ, ΔE_Q, and Γ and ±3% for relative area 88
Table 21. Values of hyperfine parameters derived from fitting AE007 metallic iron nanoparticles prepared at lengths of room temperature ambient oxidation. B_{hf} is the hyperfine magnetic field, δ is the isomer shift, ΔE_Q is the quadrupole splitting, and Γ is the linewidth (FWHM). Typical errors are ±0.5 mm/s for B_{hf}, ±0.02 mm/s for δ, ΔE_Q, and Γ and ±3% for relative area 92
Table 22. Values of hyperfine parameters derived from fitting AE003 metallic iron nanoparticles prepared at one-hour intervals of room temperature ambient oxidation. B_{hf} is the hyperfine magnetic field, δ is the isomer shift, ΔE_Q is the quadrupole splitting, and Γ is the linewidth (FWHM). Typical errors are ±0.5 mm/s for B_{hf}, ±0.02 mm/s for δ, ΔE_Q, and Γ and ±3% for relative area 95
Table 23. Values of hyperfine parameters derived from fitting AE013A PEG-coated metallic iron nanoparticles and after one hour of ambient oxidation. B_{hf} is the hyperfine magnetic field, δ is the isomer shift, ΔE_Q is the quadrupole splitting, and Γ is the linewidth (FWHM). Typical errors are ±0.5 mm/s for B_{hf}, ±0.02 mm/s for δ, ΔE_Q, and Γ and ±3% for relative area 99
Table 24. Values of hyperfine parameters derived from fitting AE013B uncoated metallic iron nanoparticles and after one hour of ambient oxidation. B_{hf} is the hyperfine magnetic field, δ is the isomer shift, ΔE_Q is the quadrupole splitting, and Γ is the linewidth (FWHM). Typical errors are ±0.5 mm/s for B_{hf}, ±0.02 mm/s for δ, ΔE_Q, and Γ and ±3% for relative area 102
Table 25. Values of hyperfine parameters derived from fitting AE014A PEG-coated metallic iron nanoparticles prepared at 30-min intervals of room temperature ambient oxidation. B_{hf} is the hyperfine magnetic field, δ is the isomer shift, ΔE_Q is the quadrupole splitting, and Γ is the linewidth (FWHM). Typical errors are ±0.5 mm/s for B_{hf}, ±0.02 mm/s for δ, ΔE_Q, and Γ and ±3% for relative area 106
Table 26. Breakdown of AE014A's total metallic iron and iron oxide percentages over time 107
Table 27. Values of hyperfine parameters derived from fitting AE014B uncoated metallic iron nanoparticles prepared at 30-min intervals of room temperature ambient oxidation. B_{hf} is the hyperfine magnetic field, δ is the isomer shift, ΔE_Q is the quadrupole splitting, and Γ is the linewidth (FWHM). Typical errors are ±0.5 mm/s for B_{hf}, ±0.02 mm/s for δ, ΔE_Q, and Γ and ±3% for relative area 110
Table 28. Breakdown of AE014B's total metallic iron and iron oxide percentages over time 111

Table 29. Table of T_2 and T_1 relaxation time results 113
Table A30. Values of hyperfine parameters derived from fitting as-made AE005 uncoated metallic iron nanoparticles at 6K and 293K. B_{hf} is the hyperfine magnetic field, δ is the isomer shift, ΔE_Q is the quadrupole splitting, and Γ is the linewidth (FWHM). Typical errors are ±0.5 mm/s for B_{hf}, ±0.02 mm/s for δ, ΔE_Q, and Γ and ±3% for relative area 123
Table A31. Values of hyperfine parameters derived from fitting AE007 48-hour oxidized metallic iron nanoparticles at 6K and 293K. B_{hf} is the hyperfine magnetic field, δ is the isomer shift, ΔE_Q is the quadrupole splitting, and Γ is the linewidth (FWHM). Typical errors are ±0.5 mm/s for B_{hf}, ±0.02 mm/s for δ, ΔE_Q, and Γ and ±3% for relative area 124
Table A32. Values of hyperfine parameters derived from fitting as-made AE008 uncoated metallic iron nanoparticles at 6K and 293K. B_{hf} is the hyperfine magnetic field, δ is the isomer shift, ΔE_Q is the quadrupole splitting, and Γ is the linewidth (FWHM). Typical errors are ±0.5 mm/s for B_{hf}, ±0.02 mm/s for δ, ΔE_Q, and Γ and ±3% for relative area 125
Table A33. Values of hyperfine parameters derived from fitting as-made AE011 uncoated metallic iron nanoparticles at 6K and 293K. B_{hf} is the hyperfine magnetic field, δ is the isomer shift, ΔE_Q is the quadrupole splitting, and Γ is the linewidth (FWHM). Typical errors are ±0.5 mm/s for B_{hf}, ±0.02 mm/s for δ, ΔE_Q, and Γ and ±3% for relative area 126
Table A34. Values of hyperfine parameters derived from fitting as-made AE013A PEG-coated and as-made AE013B uncoated metallic iron nanoparticles. B_{hf} is the hyperfine magnetic field, δ is the isomer shift, ΔE_Q is the quadrupole splitting, and Γ is the linewidth (FWHM). Typical errors are ±0.03 mm/s for B_{hf}, ±0.02 mm/s for δ, ΔE_Q, and Γ and ±3% for relative area 129
Table A35. Values of hyperfine parameters derived from fitting AE013A PEG-coated and uncoated metallic iron nanoparticles after one hour of ambient oxidation. B_{hf} is the hyperfine magnetic field, δ is the isomer shift, ΔE_Q is the quadrupole splitting, and Γ is the linewidth (FWHM). Typical errors are ±0.03 mm/s for B_{hf}, ±0.02 mm/s for δ, ΔE_Q, and Γ and ±3% for relative area 130

LIST OF FIGURES

Figure 1. Example of the effect two different theoretical coatings (A: oxygen permeable, B: oxygen resistant) have on the oxidation of metallic iron nanoparticles. As iron oxide (FeOx) percentage increases over time, nanoparticle biocompatibility increases and magnetic resonance enhancement decreases. A balance needs to be achieved between metallic iron content and oxidation rate to maximize these two properties. 4
Figure 2. Schematic of the magnetic resonance imaging (MRI) process with hydrogen protons in blue, their magnetic moments in red, and radio frequency (RF) pulses in green. a) Magnetic moments of hydrogen protons orientating randomly in the absence of an applied magnetic field b) Protons aligning parallel and antiparallel to the direction of the applied magnetic field B_0 c) Application of RF pulses flipping lower energy parallel protons into the higher energy antiparallel orientation d) Emission of the RF signal as the protons relax to their equilibrium state e) Magnetic moments of hydrogen protons returning to random orientation once the applied magnetic field is removed.....6
Figure 3. Defect of the blood-brain barrier after stroke shown in MRI. T1-weighted images: left image without contrast medium, right image with contrast medium administration. Image from Hellerhoff, Bluthirnschranke nach Infarkt nativ und KM, CC BY-SA 3.0 7
Figure 4. Transmission electron microscopy (TEM) image of nanoparticles produced through iron (II) chloride reduction and coated with polyethylene glycol (left image) and Brij 30 (right image) (reproduced with permission of J.E. King [35]) 11
Figure 5. Transmission electron microscopy (TEM) image of longer synthesis reaction time affecting size and uniformity of resulting nanoparticles. Left image: 20-minute reaction time. Right image: 40-minute reaction time. (reproduced with permission of J.E. King [35]) 12
Figure 6. Apparatus for syringe pump FeNP synthesis with and without PEG coating (AE013-AE014) 15
Figure 7. $FeCl_3$ solution reacting with $NaBH_4$ solution down the length of the separatory funnel before falling into the reaction flask for PEG coating.....17
Figure 8. Example of sample color change throughout synthesis. a) Initial $FeCl_3$ dissolved in H_2O/EtOH solution. b) Black FeNPs precipitating into solution mid-synthesis. c) FeNP “island” forming over magnetic stir bar once synthesis is complete. Throughout synthesis, the solution has transformed from a homogeneous rust-orange color to black nanoparticles floating in a yellow-tinted solution. 19
Figure 9. Magnetic separation of an iron nanoparticle solution post-synthesis. Once the nanoparticles have settled close to the magnet, the remaining reaction liquid is removed and either deionized water or absolute ethanol is introduced to wash the particles before the process is repeated. Inset:

separation of solution into layers (FeNP, water, reaction byproducts) after 5 minutes on a magnet 20
Figure 10. Vacuum filtration apparatus for removing solids from a suspension .. 21
Figure 11. An overview of the vacuum filtration process: a) Wet FeNPs being washed with EtOH and H_2O b) Semi-dry caked FeNPs post-filtration c) Removing FeNPs from filter paper before further drying in the glovebox furnace 23
Figure 12. MBRAUN glovebox with argon atmosphere for long-term FeNP sample storage and drying. Inset: programmable furnace used to dry nanoparticles while inside the glovebox 24
Figure 13. a) Aggregated FeNP immediately after drying in the glovebox furnace. b) Final dried FeNP powder created from fracturing aggregated FeNP structures 25
Figure 14. As-made AE007 FeNPs (left) vs AE007 FeNPs oxidized in air for 2 hours 27
Figure 15. FEI Tecnai Osiris Transmission Electron Microscope at VINSE. Image reused with permission 27
Figure 16. UTSI's Phillips X'Pert X-ray Diffractometer 29
Figure 17. NanoPlus DLS apparatus. Inset: DLS cuvette sample holder 30
Figure 18. Example of Mössbauer sample holders 32
Figure 19. Room temperature Mössbauer apparatus 32
Figure 20. Low temperature Mössbauer apparatus with cryostat 33
Figure 21. Example of NMR tubes filled with various concentrations of nanoparticle solution for relaxometry measurements 34
Figure 22. Agglomerated AE001 metallic iron nanoparticles. Dark regions correspond to iron, while lighter regions are iron oxide. The arrow indicates the presence of an iron oxide shell 37
Figure 23. AE001 metallic iron nanoparticle superstructure with silica coating. Dark areas are iron while lighter areas are either iron oxide or silica coating/nanobeads. Insets give a 2x zoom view of agglomeration and coating adherence 38
Figure 24. Agglomeration of AE001 metallic iron nanoparticles at a smaller scale length. Both crystalline metallic iron and crystalline iron oxide are apparent 39
Figure 25. Transmission electron microscopy (TEM) of AE003 uncoated metallic iron nanoparticles. Dark areas are iron while lighter areas are of an iron oxide shell caused by oxidation of the nanoparticle surface 40
Figure 26. SEM image of AE008 metallic iron nanoparticles arranging as sintered aggregates 42
Figure 27. SEM image of AE008 metallic iron nanoparticles arranging as sintered aggregates 43
Figure 28. a) SEM image of AE008 metallic iron nanoparticles arranging as sintered aggregates b) Backscattered electron image of same region

allowing for differentiation between core and shell. Numbered areas indicate the location of core-shell diameter measurements 44
Figure 29. XRD results for AE005 metallic iron nanoparticles synthesized through dropwise $FeCl_3$ reduction with $NaBH_4$. Below the sample spectrum is the pattern for body-centered cubic (bcc) α-Fe (JCPDS # 87-0722)..... 46
Figure 30. XRD results for AE007 metallic iron nanoparticles synthesized through dropwise $FeCl_3$ reduction with $NaBH_4$. Samples were characterized at three separate lengths of ambient oxidation. Below the sample spectra are the patterns for body-centered cubic (bcc) α-iron (JCPDS # 87-0722) and face-centered cubic (fcc) metallic aluminum (JCPDS # 89-4037)..... 47
Figure 31. XRD results for AE008 metallic iron nanoparticles synthesized through dropwise $FeCl_3$ reduction with $NaBH_4$. Below the sample spectrum are the patterns for body-centered cubic (bcc) α-iron (JCPDS # 87-0722) and face-centered cubic (fcc) metallic aluminum (JCPDS # 89-4037)..... 49
Figure 32. AE001 DLS results 51
Figure 33. AE003 as-made DLS results..... 52
Figure 34. AE004 DLS results 54
Figure 35. AE006 DLS results 55
Figure 36. AE007 DLS results 56
Figure 37. AE008 DLS results 57
Figure 38. AE009 DLS results 59
Figure 39. AE010 DLS results 60
Figure 40. AE011 DLS results 61
Figure 41. AE013B DLS results 62
Figure 42. AE014A DLS results 63
Figure 43. Stacked ^{57}Fe Mössbauer spectra of as-made AE001, AE002, and AE003 iron nanoparticles measured at 293 K. Each sample followed the same basic synthesis route (syringe pump $FeCl_3$ reduction with KBH_4 solution) with the following distinctive features: AE001 was synthesized in air with silica coating, AE002 was synthesized in a nitrogen flow with silica coating, and AE003 was synthesized as a 5x larger batch in a nitrogen flow with no silica coating. 65
Figure 44. Stacked ^{57}Fe Mössbauer spectra of as-made AE005, AE006, and AE011 iron nanoparticles measured at 293K. Each sample followed the same basic synthesis route ($FeCl_3$ reduction in air with dropwise $NaBH_4$ solution, subsequent furnace drying) with the following distinctive features: AE005's dropwise synthesis lasted 35 min, AE006's dropwise synthesis lasted 15 min, and AE011's dropwise synthesis lasted 8 min. Not pictured: AE004 71
Figure 45. Stacked ^{57}Fe Mössbauer spectra of as-made AE007 and AE008 iron nanoparticles measured at 293K. Each sample followed the same basic synthesis route: $FeCl_3$ reduction in argon with dropwise $NaBH_4$ solution, vacuum filtration, and subsequent furnace drying..... 75

Figure 46. Stacked ^{57}Fe Mössbauer spectra of as-made AE009 and AE010 iron nanoparticles measured at 293K. Each sample followed the same basic synthesis route: $FeCl_3$ reduction in argon with dropwise $NaBH_4$ solution, vacuum filtration, and subsequent furnace drying.....77
Figure 47. Stacked ^{57}Fe Mössbauer spectra of as-made PEG-coated AE013A and AE014A iron nanoparticles measured at 293K. Each sample followed the same basic synthesis route: syringe pump $FeCl_3$ reduction with $NaBH_4$ solution followed by vacuum filtration and glovebox furnace drying.....80
Figure 48. Stacked ^{57}Fe Mössbauer spectra of as-made AE013B and AE014B iron nanoparticles measured at 293K. Each sample followed the same basic synthesis route: syringe pump $FeCl_3$ reduction with $NaBH_4$ solution followed by vacuum filtration and glovebox furnace drying. 83
Figure 49. Stacked ^{57}Fe Mössbauer spectra of AE001 iron nanoparticles three separate time intervals (as-made, 72 hrs, 2 weeks) throughout an oxidation process in air, measured at 293 K 87
Figure 50. Stacked ^{57}Fe Mössbauer spectra of AE007 FeNPs at three time intervals (as-made, 2-hrs, 48-hrs) throughout an oxidation process in air, measured at 293 K 91
Figure 51. Stacked ^{57}Fe Mössbauer spectra of AE003 iron nanoparticles at one-hour intervals throughout an aging process in air, measured at 293 K.....94
Figure 52. Stacked ^{57}Fe Mössbauer spectra of as-made AE013A PEG-coated iron nanoparticles and one hour oxidized nanoparticles in air, measured at 293 K 97
Figure 53. Stacked ^{57}Fe Mössbauer spectra of as-made AE013B uncoated iron nanoparticles and one hour oxidized nanoparticles in air, measured at 293 K 100
Figure 54. Stacked time series ^{57}Fe Mössbauer spectra of as-made AE014A PEG-coated iron nanoparticles oxidized at 30-minute intervals in air, measured at 293 K 104
Figure 55. Stacked time series ^{57}Fe Mössbauer spectra of as-made AE014B uncoated iron nanoparticles oxidized at 30-minute intervals in air, measured at 293 K 109
Figure 56. T_2 and T_1 map with varying concentrations of metallic iron nanoparticle samples. Samples denoted with a red box are AE001 nanoparticles increasing in concentration from left to right. Samples denoted with a white box are AE002 nanoparticles increasing in concentration from left to right. A deionized water control is denoted with an orange star 113
Figure A57. Stacked ^{57}Fe Mössbauer spectra of as-made AE005 uncoated metallic iron nanoparticles, measured at 6K and 293K.....123
Figure A58. Stacked ^{57}Fe Mössbauer spectra of 48-hour oxidized AE007 metallic iron nanoparticles, measured at 6K and 293K.....124
Figure A59. Stacked ^{57}Fe Mössbauer spectra of AE008 uncoated metallic iron nanoparticles, measured at 6K and 293K.....125

Figure A60. Stacked ^{57}Fe Mössbauer spectra of AE011 uncoated metallic iron nanoparticles, measured at 6K and 293K 126
Figure A61. Oxidation rate of AE003 calculated through linear fit of oxide percentage over time. Oxidation rate was found to be 5.3%/hour 127
Figure A62. Oxidation rate of AE014A calculated through linear fit of oxide percentage over time. Oxidation rate was found to be 7%/30-min, 14%/hour 128
Figure A63. Stacked ^{57}Fe Mössbauer spectra of as-made PEG-coated (AE013A) and uncoated (AE013B) metallic iron nanoparticles, measured at 293 K .. 129
Figure A64. Stacked ^{57}Fe Mössbauer spectra of PEG-coated (AE013A) and uncoated (AE013B) metallic iron nanoparticles after one hour ambient oxidation, measured at 293 K 130

CHAPTER I
INTRODUCTION

Iron Oxide Nanoparticles vs Metallic Iron Nanoparticles

Iron oxide nanoparticles such as magnetite (Fe_3O_4) and maghemite (γ-Fe_2O_3) have long been studied for their magnetic properties and use in medical applications such as magnetic resonance imaging (MRI), hyperthermia, and drug delivery [1-10]. Iron oxide nanoparticles are chemically stable, non-toxic, and biodegradable. Consequently, iron oxide nanoparticles (IONPs) have undergone regulatory approval and have been deemed safe and legal for use in humans. Despite a long history of research, iron oxide nanoparticles are not the optimal material for these applications due to their oxidized state limiting saturation magnetization.

Magnetization saturation is the state in which the magnetization of a material cannot be further increased by increasing the applied external magnetic field to the material. Materials with higher magnetization saturation possess a larger density of magnetic flux through the material and therefore generate a stronger magnetic moment. Pure metallic iron with no oxide contamination has the highest room temperature magnetization saturation (σ_s) of any element, roughly double the magnitude of its strongest iron oxide counterparts [1, 3]. This offers a clear advantage in magnetic applications such as MRI contrast or hyperthermia; the largest magnetic moment a metallic iron nanoparticle can produce is larger than that of any other metal.

Metallic iron, however, does not come without difficulties; it is highly reactive and therefore is not stable in the aqueous environment required by biological conditions in medical applications. Iron rapidly oxidizes when exposed to water and oxygen, losing all its desirable magnetization saturation advantages as its surface oxidizes into more stable iron oxide forms like maghemite. Stability and metallic iron content can be preserved through biocompatible coatings such as

polyethylene glycol (PEG), but this is also a delicate balance; magnetization saturation decreases as coating thickness increases.

Another possibility would be to embrace the reactivity of metallic iron and attempt to control its oxidation using a tunable biocompatible coating such as polyethylene glycol (PEG). Coatings of various chemical composition, molecular length, or surface thickness can be applied to the metallic iron nanoparticles to control their rate of oxidation into iron oxide. A metallic iron nanoparticle with controllable oxidation would combine the biocompatibility and FDA-approval of iron oxide with the magnetic strength of metallic iron. This phenomenon is explained further in Figure 1.

Metallic Iron Nanoparticle Applications

A material of great and varied research interest, metallic iron nanoparticles (also termed zero-valent iron (ZVI)) have been studied for their potential utilization in data storage [11, 12], catalysis [3, 13-15], energy conversion [15-17], and environmental and wastewater remediation [18-27]. This dissertation, however, is focused on the production and characterization of metallic iron nanoparticles for their medical applications in magnetic resonance imagining (MRI) contrast enhancement and hyperthermia treatment of cancer.

Magnetic Resonance Imaging (MRI) Contrast Agent

Magnetic resonance imaging (MRI) is based on the magnetic properties of the protons within hydrogen atoms aligning in the direction of a strong applied magnetic field. In the absence of an applied magnetic field, hydrogen atoms and their magnetic moments are randomly orientated, resulting in no overall magnetic field. Once the primary magnetic field (typically 1.5-3 T) is applied to the body, protons align parallel or antiparallel in the direction of the magnetization. A greater proportion of the hydrogen protons align parallel to the applied field than

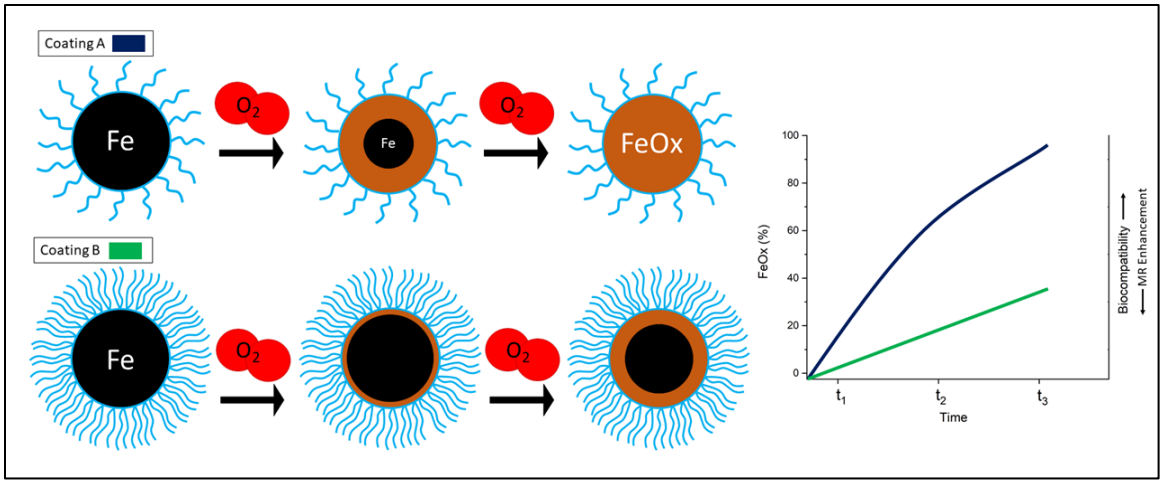


Figure 1. Example of the effect two different theoretical coatings (A: oxygen permeable, B: oxygen resistant) have on the oxidation of metallic iron nanoparticles. As iron oxide (FeOx) percentage increases over time, nanoparticle biocompatibility increases and magnetic resonance enhancement decreases. A balance needs to be achieved between metallic iron content and oxidation rate to maximize these two properties.

antiparallel, leading to a net magnetic vector in the direction of the applied magnetic field. While in alignment with the magnetic field, protons spin in a circular path around the axis of the applied field in a phenomenon known as precession. The frequency of precession is directly proportional to the strength of the applied magnetic field. Once the protons are aligned with the magnetic field, a radio frequency pulse with the same precession frequency is applied and knocks the protons out of alignment with the field. The process of the protons returning to their equilibrium state in alignment with the magnetic field is called relaxation, and this relaxation phenomenon generates a signal that can be processed into a magnetic resonance image of the specimen [1, 3, 28-35]. A schematic outlining this process can be seen on the next page in Figure 2.

There are two types of independent relaxation phenomena that can help generate magnetic resonance images, T_1 (longitudinal, spin relaxation) and T_2 (transverse, spin dephasing). Magnetic nanoparticles enhance MRI contrast by modifying the magnetic field in their vicinity, thereby changing local longitudinal and transverse relaxation times [28, 29, 32-35]. MRI contrast agents do not make an MR image clearer by increasing image resolution. Instead, they provide a material to contrast with that of the local tissue being imaged, allowing for structures that would normally be problematic to view to be seen. An example of the effect MRI contrast agent administration has on the perceptibility of local structures can be seen in Figure 3. Because spin dephasing occurs primarily through magnetic interactions, strong magnetic species have a larger effect on T_2 relaxation times, and as such are better suited as T_2 enhancers. Zero-valent iron nanoparticles, with their strong magnetic properties, suit this application well.

Hyperthermia

Hyperthermia is a cancer treatment technique in which a cancerous tumor is locally heated to a temperature greater than 42 ºC for a period of time in order to destroy it [28, 29, 36-38]. Hyperthermia treatment with metallic iron nanoparticles

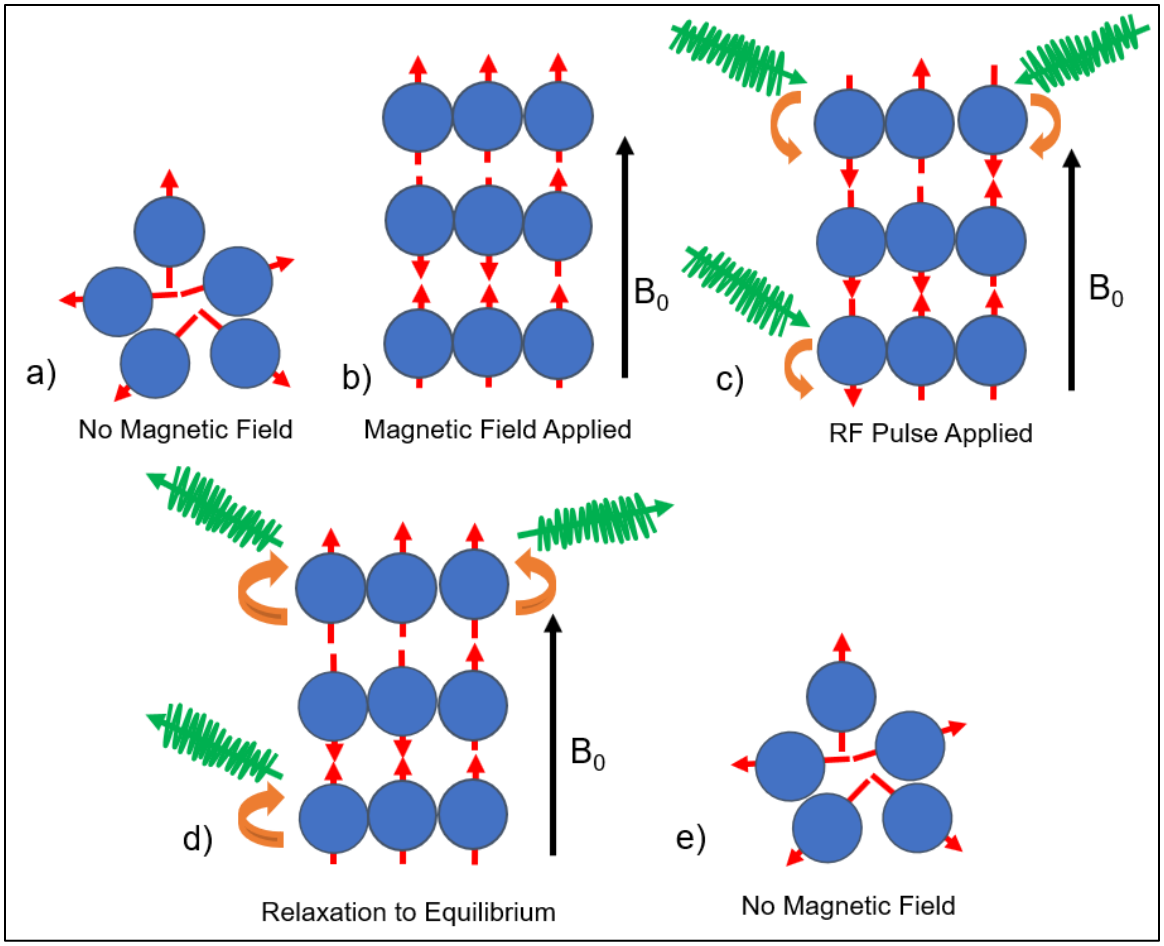


Figure 2. Schematic of the magnetic resonance imaging (MRI) process with hydrogen protons in blue, their magnetic moments in red, and radio frequency (RF) pulses in green. a) Magnetic moments of hydrogen protons orientating randomly in the absence of an applied magnetic field b) Protons aligning parallel and antiparallel to the direction of the applied magnetic field B_0 c) Application of RF pulses flipping lower energy parallel protons into the higher energy antiparallel orientation d) Emission of the RF signal as the protons relax to their equilibrium state e) Magnetic moments of hydrogen protons returning to random orientation once the applied magnetic field is removed

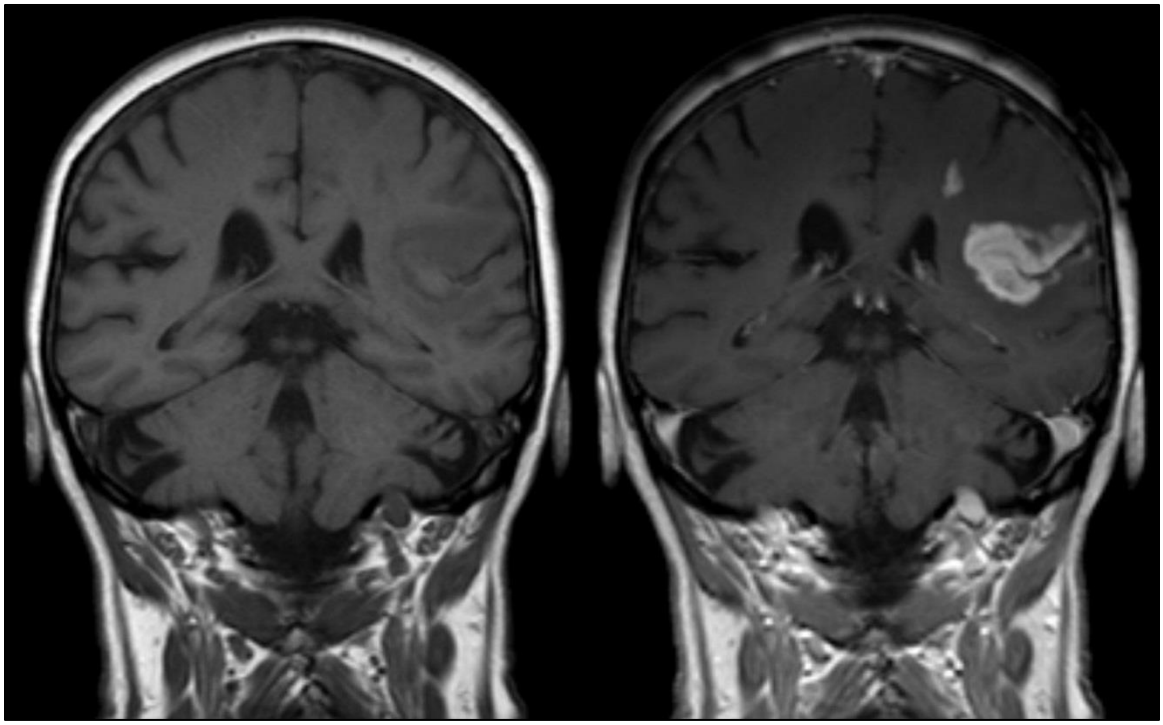


Figure 3. Defect of the blood-brain barrier after stroke shown in MRI. T1-weighted images: left image without contrast medium, right image with contrast medium administration. Image from Hellerhoff, Bluthirnschranke nach Infarkt nativ und KM, CC BY-SA 3.0

would involve dispersing the nanoparticle fluid throughout the target tissue, and then applying an alternating current magnetic field to the target area. An alternating magnetic field of sufficient strength and frequency would cause the particles to heat through hysteresis losses (work done by the magnetizing force against the internal friction of the nanoparticles to the alternating field), thereby killing the tumorous tissue. Other hyperthermia treatment techniques and devices have difficulties with incidentally heating healthy tissue in addition to the tumor tissue. The targeted nature of magnetic nanoparticle hyperthermia, either through direct injection, intravascular administration, or antibody targeting, allows healthy tissue to be spared and is a large part of the technique's appeal.

Metallic iron nanoparticles are more desired than iron oxide nanoparticles for this application due to metallic iron's higher saturation magnetization (σ_s). By having a higher saturation magnetization and therefore a larger response to the applied alternating magnetic field (i.e. more generated heat per volume), metallic iron nanoparticles allow for less material to be injected into the patient while still experiencing the desired amount of localized heating and tumor death.

Additionally, magnetic fields below 15 kAm^{-1} and frequencies between 0.05-1.2 MHz are employed in order to avoid potential negative side effects such as cardiac arrhythmia, muscle stimulation, and general heating/discomfort [3, 28, 29, 38-42]. An optimized metallic iron nanoparticle with high σ_s would generate the appropriate amount of heating while needing the minimum amount of nanoparticle material for these required magnetic field parameters.

Previous Iron Nanoparticle Work at UTSI

Previous iron nanoparticle research at the University of Tennessee Space Institute focused on a variety of synthesis routes as well as characterizing the size distribution and metallic iron content of the produced nanoparticles [33, 35].

Reduction of Iron (II) Chloride

An attempt toward synthesizing metallic iron nanoparticles was made through a reduction reaction of iron (II) chloride dissolved in ethanol with an aqueous solution of sodium borohydride. A syringe pump was used to control reaction rate. Reduction of iron (II) chloride produced a mixture of metallic iron and iron oxide nanoparticles that was confirmed with Mössbauer spectroscopy. Samples were primarily composed of maghemite (γ-Fe_2O_3), with the remaining material being metallic α-Fe. Coating with Brij produced smaller particles (3-20 nm), while coating with polyethylene glycol (PEG) helped preserve metallic iron content at the cost of larger cross-linked particles (Figure 4). A variation of this synthesis method is the subject of this dissertation.

Thermal Decomposition of Iron Pentacarbonyl

An attempt toward synthesizing smaller (< 10 nm), more uniform metallic iron nanoparticles was made through the thermal decomposition of iron pentacarbonyl [43, 44]. An octadecene and oleylamine solution was heated to 250 ºC before iron pentacarbonyl ($Fe(CO)_5$) was injected into the reaction flask. The reaction was left to stir at 250 ºC for another 20 or 40 minutes before being allowed to cool to room temperature. While the resulting nanoparticles were found to be of adequate size (10-30 nm), thermal decomposition produced almost entirely maghemite (γ-Fe_2O_3) nanoparticles with small metallic α-Fe cores. Uniformity of synthesized nanoparticles varied heavily with reaction time; persistent heating caused the nanoparticles to nucleate further and grow. The effect of reaction time on resultant nanoparticle uniformity and size can be seen in Figure 5. Since the nanoparticles produced by this route were primarily iron oxide, thermal decomposition of iron pentacarbonyl was not considered for this dissertation.

Summary of Work

The aim of this research is to successfully synthesize metallic iron (zero-valent iron) nanoparticles for biomedical applications in hyperthermia cancer treatment or as a magnetic resonance imaging (MRI) contrast agent. Iron nanoparticles were synthesized through a reduction reaction of iron (III) chloride and subsequently characterized for size, uniformity, and metallic iron content. This work explores the effect ambient oxidation has on the chemical composition of both coated and uncoated metallic iron nanoparticles, thereby determining oxidation rate. Once oxidation rate is determined, a tunable nanoparticle with a controlled oxidation rate can be developed to combine the biocompatibility of iron oxide with the desirable magnetization saturation properties of metallic iron.

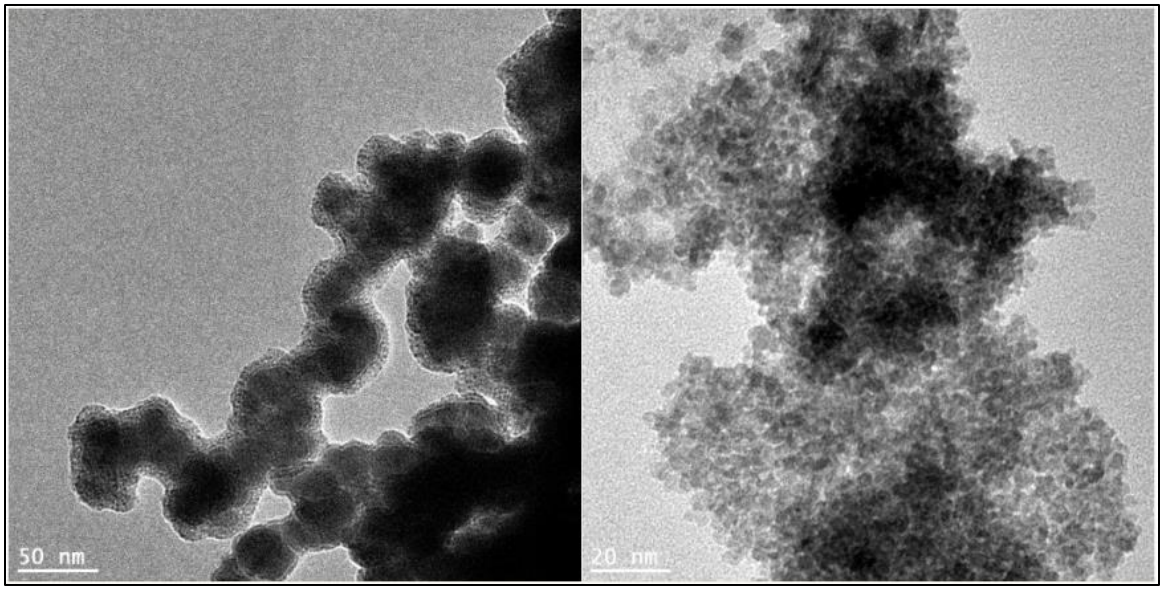


Figure 4. Transmission electron microscopy (TEM) image of nanoparticles produced through iron (II) chloride reduction and coated with polyethylene glycol (left image) and Brij 30 (right image) (reproduced with permission of J.E. King [35])

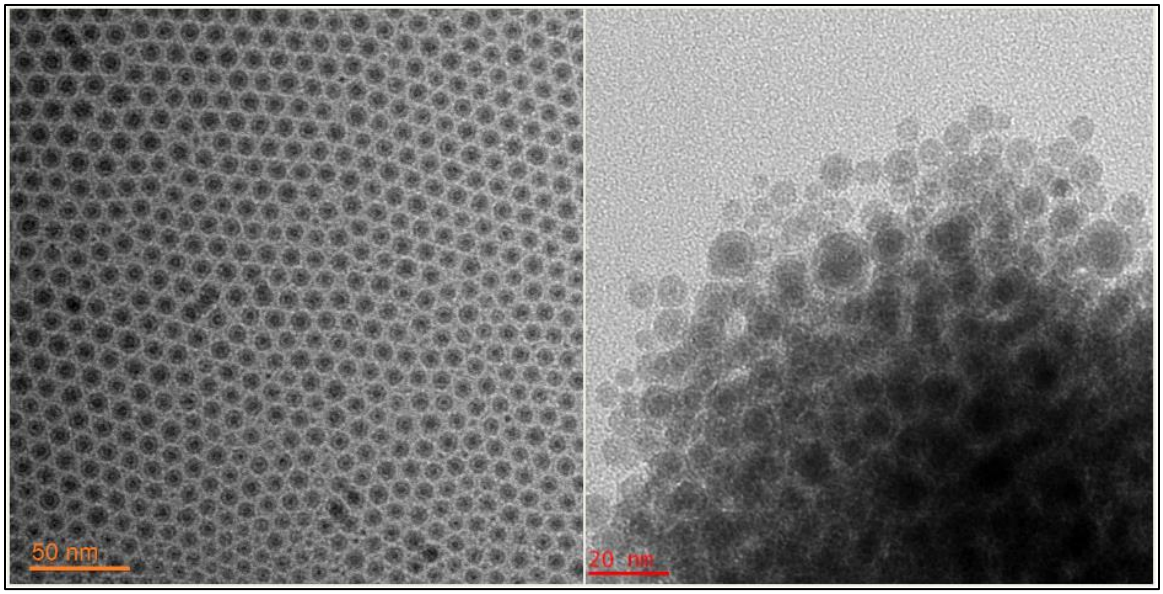


Figure 5. Transmission electron microscopy (TEM) image of longer synthesis reaction time affecting size and uniformity of resulting nanoparticles. Left image: 20-minute reaction time. Right image: 40-minute reaction time. (reproduced with permission of J.E. King [35])

CHAPTER II
EXPERIMENTAL METHODS

Iron Nanoparticle Synthesis

Syringe Pump Reduction of Iron (III) Chloride

Iron nanoparticle synthesis experiments were performed at the University of Tennessee Space Institute. Metallic iron nanoparticles were prepared via reduction of iron (III) chloride at room temperature. For AE001 and AE002, ~ 2 g of $FeCl_3 \cdot 6H_2O$ was dissolved in a 70% ethanol/water mixture (21 mL EtOH + 9 mL deionized water). The reducing agent was prepared by dissolving 0.60 g of $NaBH_4$ in 15 mL of deionized water. The reducing agent was then taken up into a syringe and placed into the syringe pump. The syringe pump allows for consistent control of the reactant solution dispersal. The ferric solution was added to a three neck round bottomed flask and stirred at 800 rpm. To impart the particles with a silica coating through a Stöber process, 0.05 mL tetraethyl orthosilicate (TEOS) was added to the three-neck round and stirred for another 15 min. The reducing agent solution was added at a rate of 5 mL/min until completely dispensed, after which the nanoparticle solution was stirred for another 10 minutes. As the reducing agent was added to the amber-colored ferric solution, black particles began to appear, signifying the presence of metallic iron nanoparticles. AE001's synthesis was performed in an ambient atmosphere, while AE002 was synthesized under a nitrogen flow. AE003 followed the same synthesis parameters as AE002 but was a synthesis with five times more initial reagents and did not have an attempted silica coating.

The next samples to be synthesized using a syringe pump were AE013 and AE014. An example of the apparatus arrangement for these syntheses can be seen below in Figure 6. In the lower round bottom flask, 300 µL polyethylene glycol (PEG) was pipetted into 20 mL deionized water and stirred at 400 rpm. ~ 1.4 g $FeCl_3 \cdot 6H_2O$ was dissolved in 15 mL deionized water and up taken up into a syringe. ~ 0.7 g $NaBH_4$ was dissolved in 15 mL deionized water and taken up into a separate syringe, then both syringes were placed in the syringe pump. Rubber tubing from each syringe was placed into a separatory funnel. The

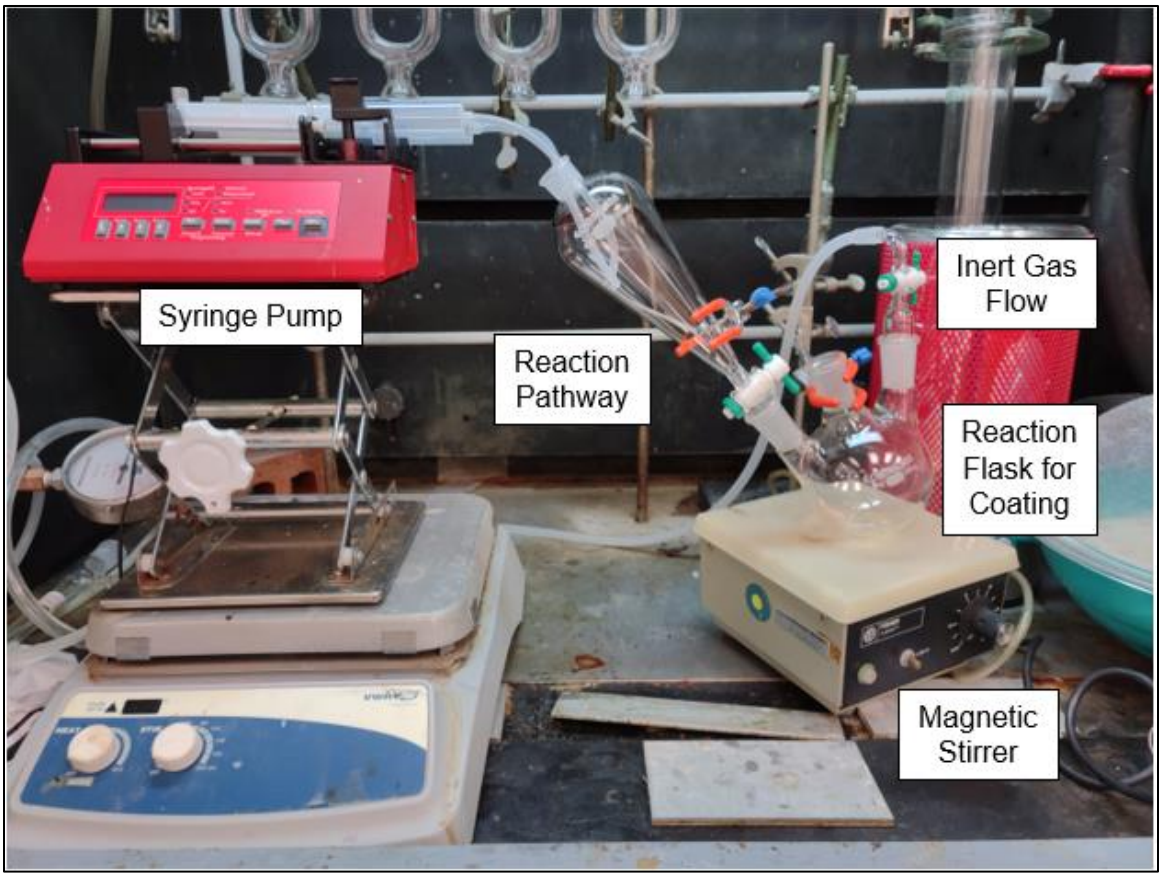


Figure 6. Apparatus for syringe pump FeNP synthesis with and without PEG coating (AE013-AE014)

separatory funnel acted as a reaction pathway for the two solutions to mix before dropping into the polyethylene glycol (PEG) coating solution in the lower round bottom flask. The reactant solutions were dispersed at 15 mL/min by the syringe pump. As the solutions mixed and travelled down the length of the separatory funnel, the amber-colored ferric solution became black as particles began to appear, signifying the presence of metallic iron nanoparticles. Another angle of the separatory funnel acting as a reaction pathway can be seen below in Figure 7. Some particles remained in the separatory funnel and were thus uncoated. These particles were labelled as AE013B and AE014B. Particles that were coated were stirred at 400 rpm for an additional 15 min and were labelled AE013A and AE014A. Both AE013 and AE014 were synthesized in an argon gas flow. AE014 followed the same synthesis parameters as AE013 but had two times more initial reagents.

Dropwise Reduction of Iron (III) Chloride

AE004-AE012 metallic iron nanoparticles were prepared via reduction of iron (III) chloride at room temperature. The apparatus for these syntheses was a 250 mL round bottomed flask placed on a magnetic stirrer with a separatory funnel affixed over the vertical neck of the round bottomed flask. The reaction atmosphere was varied throughout the synthesis series. The dropwise synthesis followed previous work detailed by Yuvakkumar et al. [45]. For AE004, ~1.1 g $FeCl_3 \cdot 6H_2O$ was placed into the round bottom flask and dissolved in an 80% ethanol/water mixture (48 mL EtOH + 12 mL deionized water). The reducing agent was prepared by dissolving ~ 0.8 grams of $NaBH_4$ in 100 mL of deionized water. The reducing agent solution was added dropwise (~ 2 drops/sec) until completion, after which the nanoparticle solution was stirred for another 10 minutes. As the reducing agent was added to the amber-colored ferric solution, black particles began to appear, signifying the presence of metallic iron nanoparticles.



Figure 7. $FeCl_3$ solution reacting with $NaBH_4$ solution down the length of the separatory funnel before falling into the reaction flask for PEG coating

An example of this color change during synthesis can be seen below in Figure 8. A table detailing the differences in synthesis parameters and resultant sample processing can be seen in Table 1.

Sample Washing and Magnetic Separation

Once synthesis was complete, the nanoparticle solution was moved to a large glass container for sample washing and work up. The glass vessel was placed on a magnet to allow the nanoparticles to separate from the remaining reaction solution and byproducts. After a 5-15 minute period of magnetic separation, the supernatant was removed with a pipet and 50 mL deionized water was added to the nanoparticles to remove any lingering reaction byproducts. After shaking the container, the solution was left on the magnet for the nanoparticles to separate from the solution again. This process of supernatant removal, redispersion in deionized water, and magnetic separation was repeated at least three times before the sample was either stored in a glass vial or was subsequently vacuum filtered and dried in the glovebox with an argon atmosphere. An example of iron nanoparticles separating out of solution can be seen in Figure 9.

Vacuum Filtration

Thoroughly washed nanoparticles must be removed from their solution before final drying and storage in the glovebox. Filtration limits oxygen and water contamination both in the glovebox's argon atmosphere and at the nanoparticles' surface. Filtration also results in a dry powder: the preferred material state for Mössbauer samples. To this end, the nanoparticle solution is subjected to a vacuum filtration process. The vacuum filtration apparatus is detailed in Figure 10.

A Büchner funnel is attached to a vacuum filter flask. A rubber hose connects the vacuum flask to a water aspirator that is attached to a sink faucet. When the sink is turned on and water flows past the aspirator, a vacuum is pulled through the

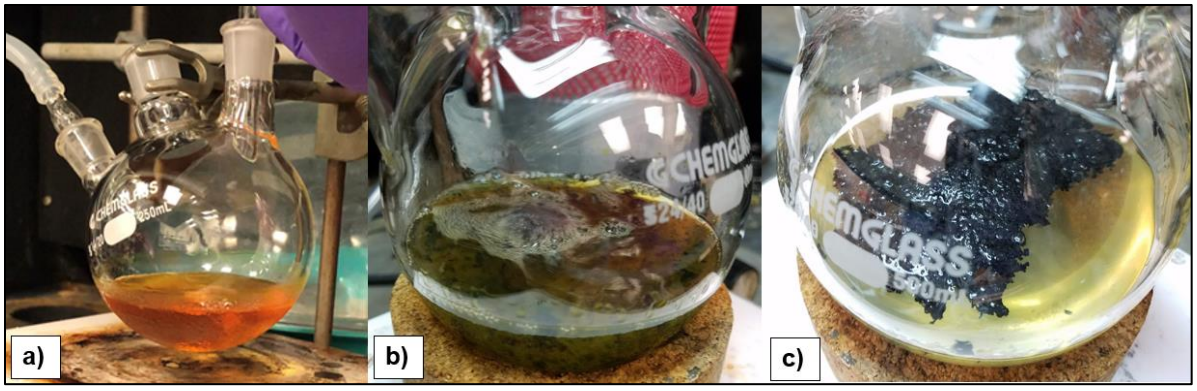


Figure 8. Example of sample color change throughout synthesis. a) Initial $FeCl_3$ dissolved in H_2O/EtOH solution. b) Black FeNPs precipitating into solution mid-synthesis. c) FeNP "island" forming over magnetic stir bar once synthesis is complete. Throughout synthesis, the solution has transformed from a homogeneous rust-orange color to black nanoparticles floating in a yellow-tinted solution.

Table 1. Synthesis parameters and sample work up procedures used for each sample

Sample	Synthesis	Atmosphere	Coating	Synthesis Size	Sample Work Up
AE001	Syringe Pump	Air	Silica	1x	Ethanol Wash
AE002	Syringe Pump	Nitrogen	Silica	1x	Ethanol Wash
AE003	Syringe Pump	Nitrogen	none	5x	Ethanol Wash
AE004	Dropwise	Air	none	1x	Vacuum Filter
AE005	Dropwise	Air	none	2x	Vacuum Filter, Furnace Dry
AE006	Dropwise	Air	none	2x	Vacuum Filter, Furnace Dry
AE007	Dropwise	Argon	none	1x	Vacuum Filter, Furnace Dry
AE008	Dropwise	Argon	none	1x	Vacuum Filter, Furnace Dry
AE009	Dropwise	Argon	none	0.5x	Vacuum Filter, Furnace Dry
AE010	Dropwise	Argon	none	1x	Ethanol Wash, Furnace Dry
AE011	Dropwise	Air	none	1x	Vacuum Filter, Furnace Dry
AE012	Dropwise	Air	none	1x	Vacuum Filter, Furnace Dry
AE013	Syringe Pump	Argon	PEG	1x	Vacuum Filter, Furnace Dry
AE014	Syringe Pump	Argon	PEG	2x	Vacuum Filter, Furnace Dry



Figure 9. Magnetic separation of an iron nanoparticle solution post-synthesis. Once the nanoparticles have settled close to the magnet, the remaining reaction liquid is removed and either deionized water or absolute ethanol is introduced to wash the particles before the process is repeated. Inset: separation of solution into layers (FeNP, water, reaction byproducts) after 5 minutes on a magnet

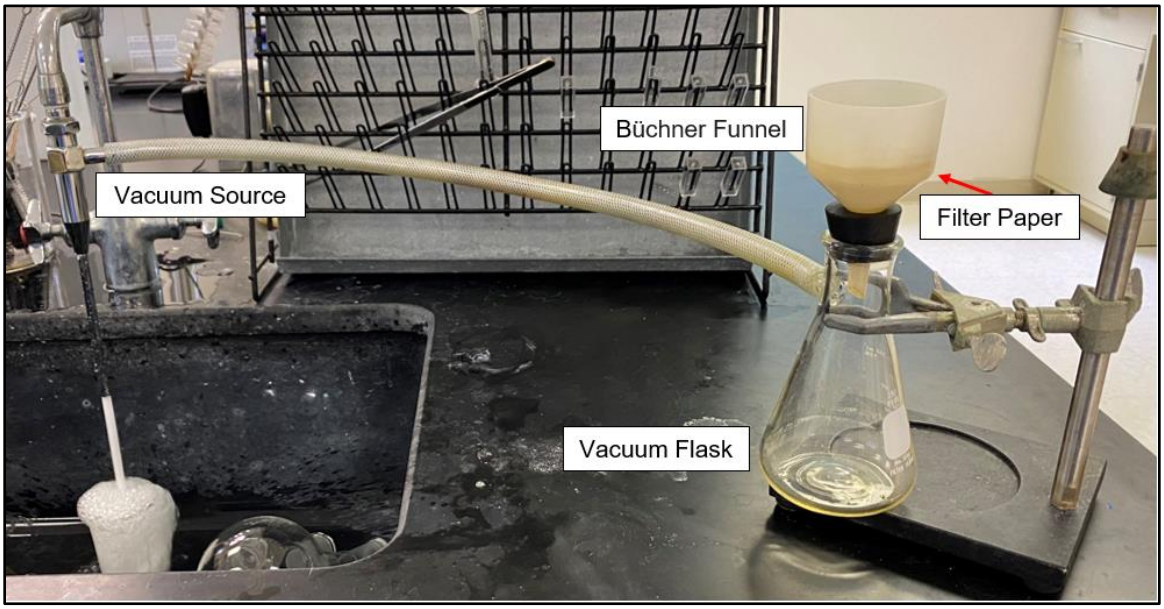


Figure 10. Vacuum filtration apparatus for removing solids from a suspension

connected hose and Büchner funnel, allowing for the solid iron nanoparticles to be separated from most of their solution. Two sheets of Whatman filter paper (grade 42, 2.5 μm pore size) are wetted to the Büchner funnel with ethanol, then the washed nanoparticle solution is poured into the Büchner funnel. The previous washing liquid (deionized water and ethanol) falls into the filter flask below as the vacuum continues to pull, leaving a semi-dried “cake” of nanoparticle powder on top of the filter paper in the Büchner funnel. This nanoparticle “cake” is given a final wash with multiple 25 mL quantities of absolute ethanol before being removed from the filter paper and placed into a vial for transport into the glovebox. An example of the nanoparticle filtration and washing process can be seen below in Figure 11.

Nanoparticle Drying and Glovebox Storage

After the samples were synthesized, washed, and vacuum filtered, the resultant nanoparticle material was placed in a glass vial and transferred into an MBRAUN glovebox (pictured in Figure 12) for sample drying and long-term storage. The glovebox has an inert argon atmosphere that protects samples from oxidation normally attributed to oxygen and water in the ambient atmosphere. Water and oxygen sensors within this glovebox typically read ~ 2.5 ppm and ~ 20 ppm, respectively.

When new samples are transferred into the glovebox, they are immediately placed in the programmable furnace and dried at 50 ºC overnight. Figure 13a shows an example of dried, aggregated nanoparticle powder immediately after furnace removal. These nanoparticle macrostructures are mechanically fragmented with a laboratory spatula into a finer powder that can be seen in Figure 13b.

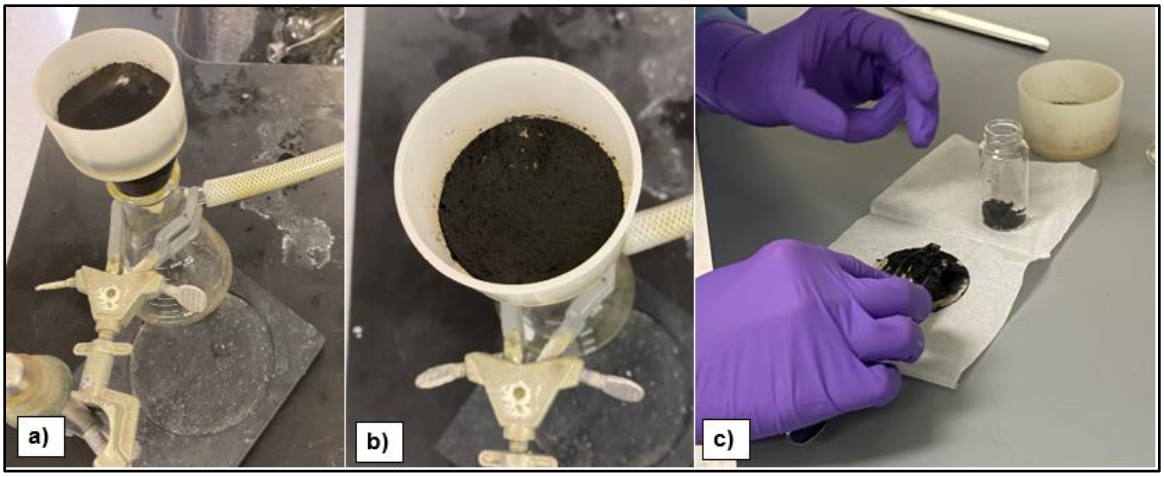


Figure 11. An overview of the vacuum filtration process: a) Wet FeNPs being washed with EtOH and H_2O b) Semi-dry caked FeNPs post-filtration c) Removing FeNPs from filter paper before further drying in the glovebox furnace

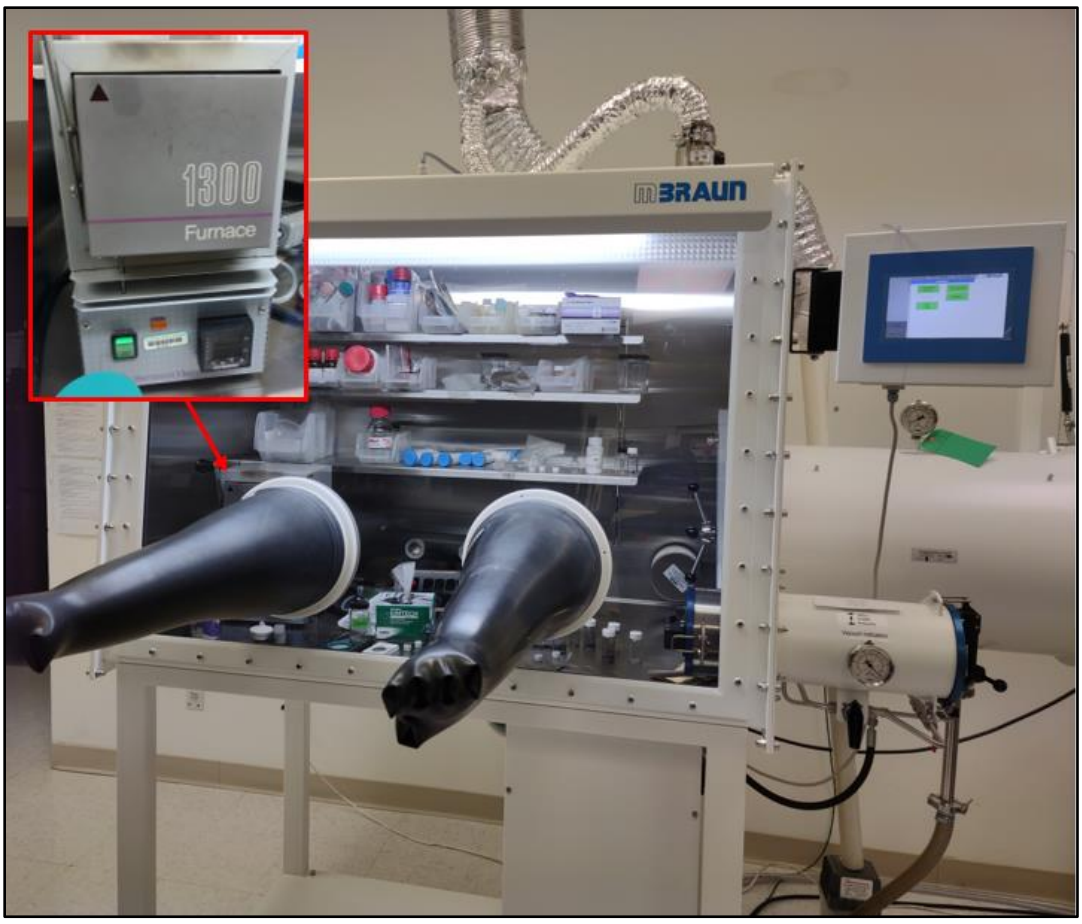


Figure 12. MBRAUN glovebox with argon atmosphere for long-term FeNP sample storage and drying. Inset: programmable furnace used to dry nanoparticles while inside the glovebox

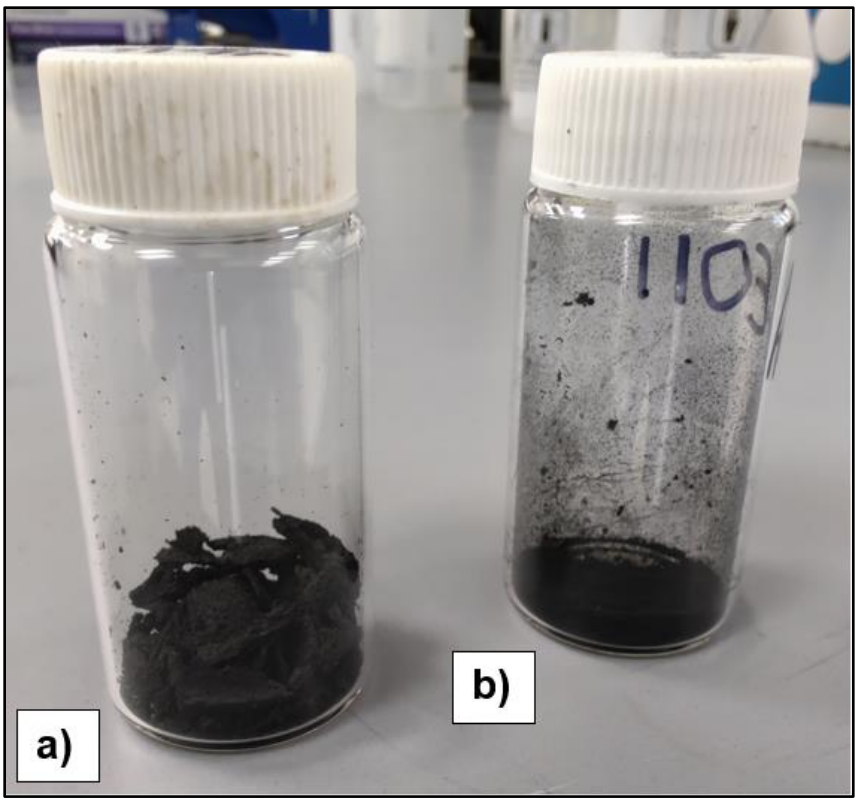


Figure 13. a) Aggregated FeNP immediately after drying in the glovebox furnace. b) Final dried FeNP powder created from fracturing aggregated FeNP structures

Ambient Oxidation of Metallic Iron Nanoparticles

For ambient oxidation experiments, dried nanoparticle powder was left at room temperature on a watch glass to age and oxidize for the required duration before being transferred to the Mössbauer apparatus for characterization. Figure 14 details the slight color variation that occurs to nanoparticle powder after a brief period (in this case two hours) of exposure to an ambient atmosphere. The powder becomes slightly greyer in the early stages of ambient oxidation. After substantial periods of time in air, metallic iron nanoparticles change from their characteristic black color to a rusty shade of orange brown, indicating the sample has fully oxidized.

Materials Characterization

Transmission Electron Microscopy

Transmission electron microscopy (TEM) was performed at the Vanderbilt Institute of Nanoscale Science and Engineering (VINSE) using an FEI Tecnai Osiris Transmission Electron Microscope operating between 80-200 kV (Figure 15). Nanoparticle samples were synthesized at the University of Tennessee Space Institute and diluted with deionized water until adequately dispersed. A probe sonicator was employed to disrupt agglomeration before a copper TEM grid was lowered into the solution and dried in air. Samples AE001 and AE003 were characterized using this technique.

Scanning Electron Microscopy

Larger nanoparticle samples were evaluated using scanning electron microscopy (SEM). Scanning Electron Microscopy (SEM) was conducted at the Vanderbilt Institute of Nanoscale Science and Engineering (VINSE) with a Zeiss MERLIN SEM Zeiss operating at 30 kV. Nanoparticle samples were synthesized at the University of Tennessee Space Institute and diluted with deionized water until



Figure 14. As-made AE007 FeNPs (left) vs AE007 FeNPs oxidized in air for 2 hours

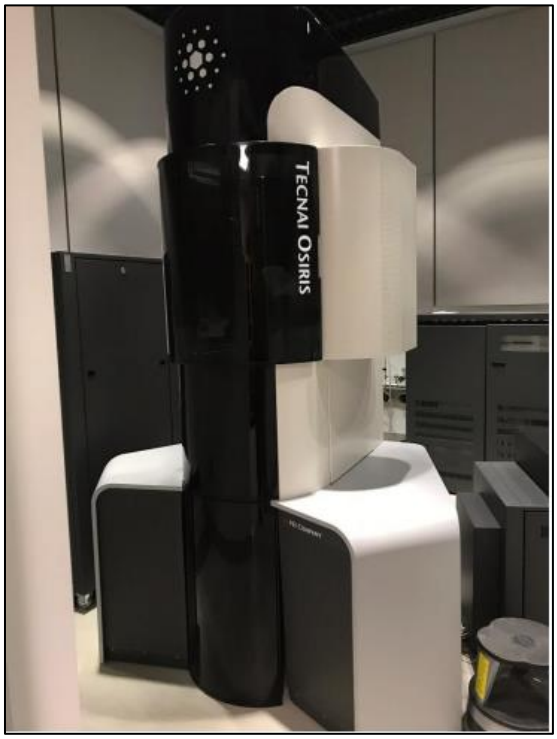


Figure 15. FEI Tecnai Osiris Transmission Electron Microscope at VINSE. Image reused with permission

adequately dispersed. A copper SEM grid was lowered into the solution and dried in air. Sample AE008 was characterized using this technique.

X-ray Diffraction

Powder X-ray diffraction (XRD) measurements were collected at room temperature on a Phillips X'Pert MRD X-ray Diffractometer (Figure 16) with a Cu anode X-ray source ($\lambda = 0.1542$ nm) in the 2θ range from 20° to 80°. Scanning rate step size was 0.015° with a time step of 4 seconds. MDI Jade 9 analytical software (Materials Data, Inc.) was employed to identify crystal phases. Because samples must be vertically mounted in this diffractometer, an aluminum sample holder with a magnetic backing was used to hold the metallic nanoparticle powder samples. Nanoparticle powder was affixed to the sample holder with a layer of vacuum grease. Samples AE005, AE007, and AE008 were characterized with this technique.

Dynamic Light Scattering

Dynamic Light Scattering (DLS) analysis was conducted at the University of Tennessee Space Institute using a Particulate Systems NanoPlus Zeta/Nano Particle Analyzer (pictured below in Figure 17). Samples were prepared by diluting the nanoparticle powder with deionized water until the solution was adequately concentrated (transparent liquid with a grey tint). Samples were further dispersed using a probe sonicator at 5 Watts for 30 seconds to diffuse agglomerates and homogenize the sample solution before examination. The solution was pipetted into a quartz cuvette and analyzed using the NanoPlus software program. Samples AE001, AE003, AE004, AE006-AE011, AE013, and AE014 were analyzed using this characterization technique.

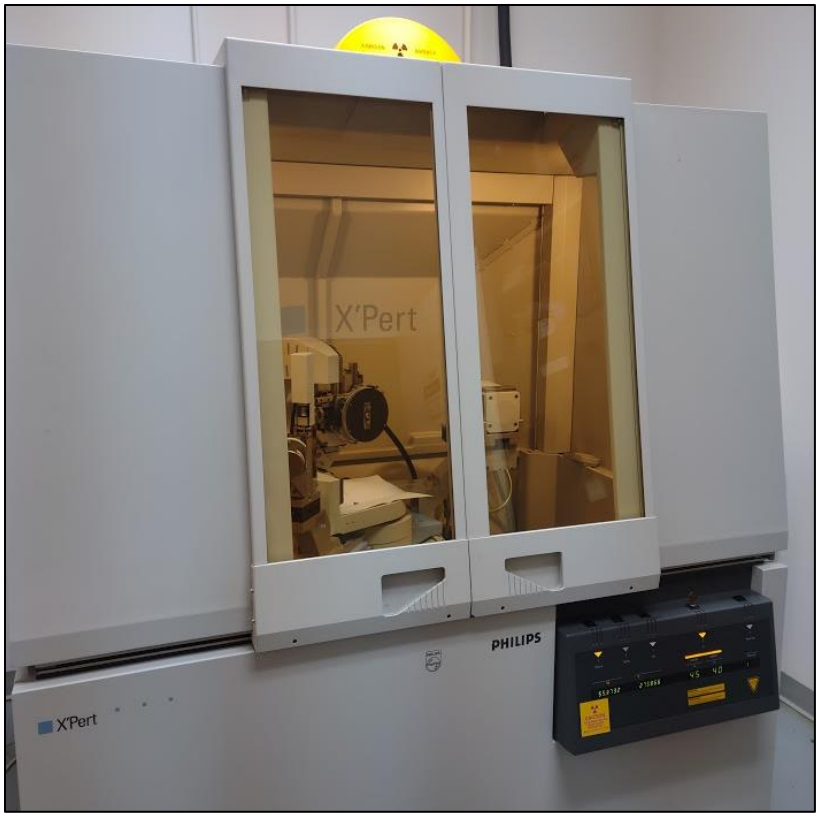


Figure 16. UTSI's Phillips X'Pert X-ray Diffractometer



Figure 17. NanoPlus DLS apparatus. Inset: DLS cuvette sample holder

Mössbauer Spectroscopy

Mössbauer spectroscopy experiments were performed at the University of Tennessee Space Institute. ^{57}Fe Mössbauer spectra were obtained with a constant acceleration drive (SEECO, Edina, MN) using a ^{57}Co/Rh radiation source, and isomer shifts were quoted relative to an α-Fe standard. Experimental temperature (293 K and 6 K) was controlled with a Janis SHI-850-5 cryogen-free continuous flow helium cryostat (Janis, Woburn, MA/SEECO) and a Lakeshore 325 Temperature Controller. Hyperfine interaction parameters were determined via least-squares fitting using Mössbauer GenFit Software (R.S. Preston and D.E. Brown). Dried nanoparticle powder samples were sealed in custom sample cups created at UTSI (Figure 18) before being placed in either the room-temperature (Figure 19) or low-temperature (Figure 20) Mössbauer apparatus. All nanoparticle samples (AE001-AE014) were characterized with this technique.

Magnetic Resonance Relaxometry

Magnetic resonance (MR) relaxometry characterization was conducted at Vanderbilt University Institute of Imaging Science. A Varian Magnetic Resonance imaging system with a 4.7 T field was employed for relaxometry measurements. AE001 and AE002 were characterized using this technique. The nanoparticle solution was diluted with deionized water into four separate concentrations before being dispersed with 60 seconds of probe sonication and placed into disposable NMR tubes for analysis (Figure 21).



Figure 18. Example of Mössbauer sample holders

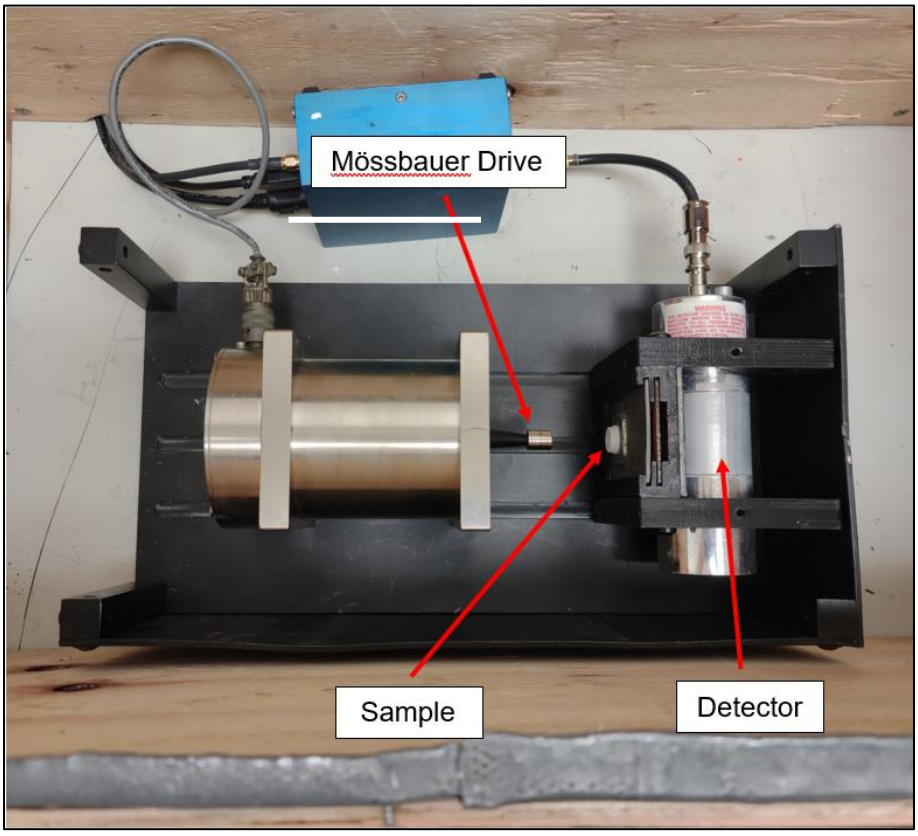


Figure 19. Room temperature Mössbauer apparatus

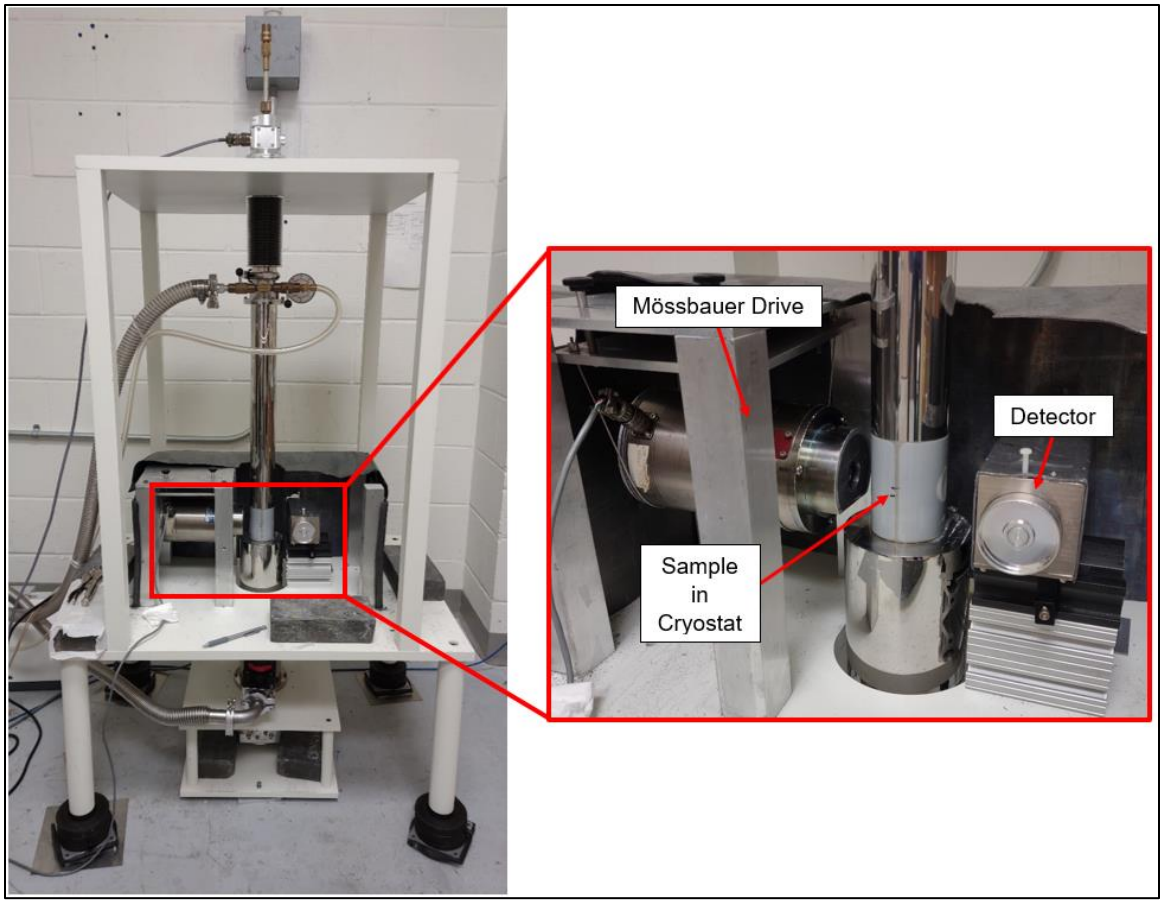


Figure 20. Low temperature Mössbauer apparatus with cryostat



Figure 21. Example of NMR tubes filled with various concentrations of nanoparticle solution for relaxometry measurements

CHAPTER III
RESULTS AND DISCUSSION

General Material Characterization

Transmission Electron Microscopy (TEM)

The transmission electron microscopy results of AE001 metallic iron nanoparticles with silica coating can be seen in Figures 22-24. AE001 nanoparticles were synthesized in an ambient atmosphere through an $FeCl_3$ reduction with KBH_4 and a silica coating. Figure 22 shows an agglomerated mass of black iron nanoparticle material surrounded by lighter iron oxide material. It is difficult to determine particle size due the severity of the aggregation but particle size can be estimated between 20-50 nm. Crystalline dark-colored iron nanometal resides in the middle of the mass, while iron oxide is on the outer areas of the mass. Figure 23 shows a large aggregated array of iron metal, iron oxide, and silica nanoparticles ranging in size between 20-70 nm. Some nanoparticles possess a core-shell iron-iron oxide structure, while others are completely oxidized. Although individual nanoparticles are discernable, a superstructure such as this would appear as an agglomerate when using another characterization technique like dynamic light scattering. It is difficult to determine whether the attempted silica coating adhered to the nanoparticles or instead provided the metal nanoparticles a lattice on which to aggregate. Figure 24 also illustrates a closer view of crystalline iron metal and crystalline iron oxide agglomeration. The same trend of black iron nanoparticle material surrounded by lighter iron oxide material can be seen.

Transmission electron microscopy (TEM) of AE003 uncoated metallic iron nanoparticles can be seen below in Figure 25. AE003 nanoparticles were synthesized in a nitrogen atmosphere through a reduction of $FeCl_3$ with KBH_4 and remained uncoated. TEM shows nanoparticles with well-preserved dark iron metal cores between 6-9 nm in diameter and white iron oxide outer shells between 3-5 nm. The natural oxide shell shields the metal iron core from further oxidation.

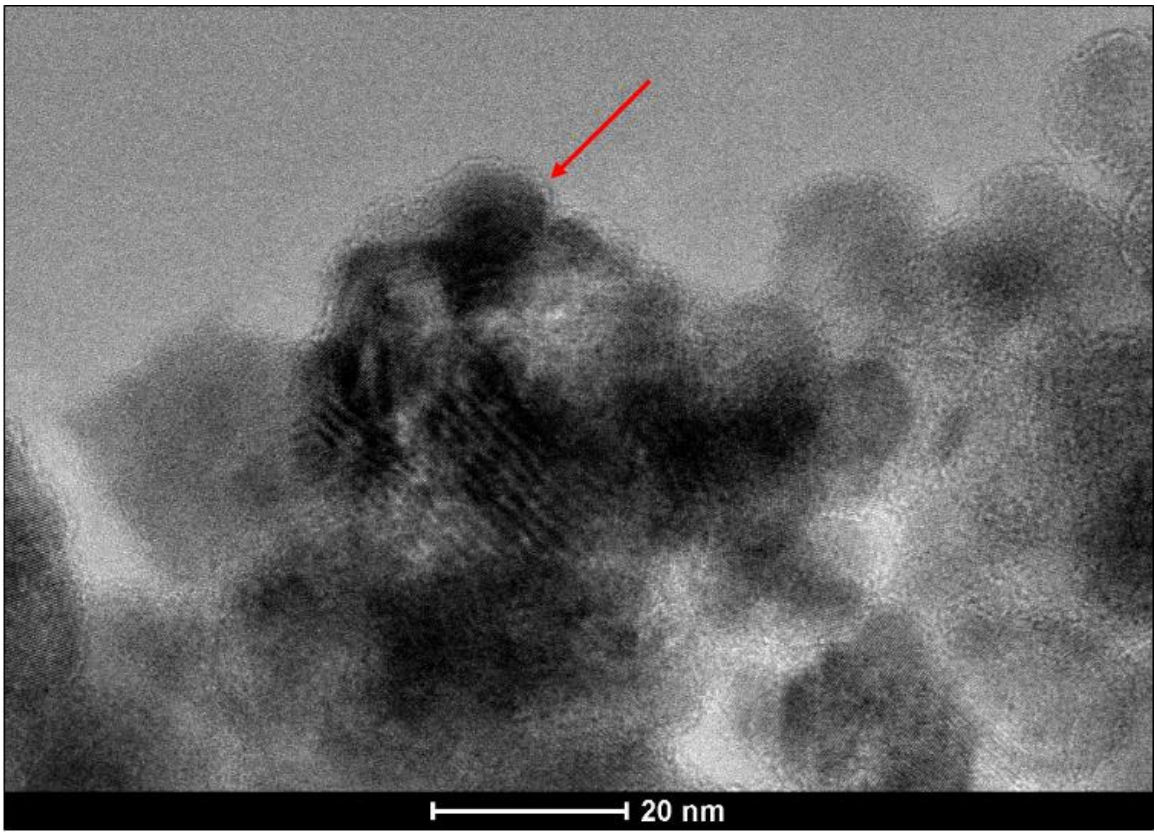


Figure 22. Agglomerated AE001 metallic iron nanoparticles. Dark regions correspond to iron, while lighter regions are iron oxide. The arrow indicates the presence of an iron oxide shell

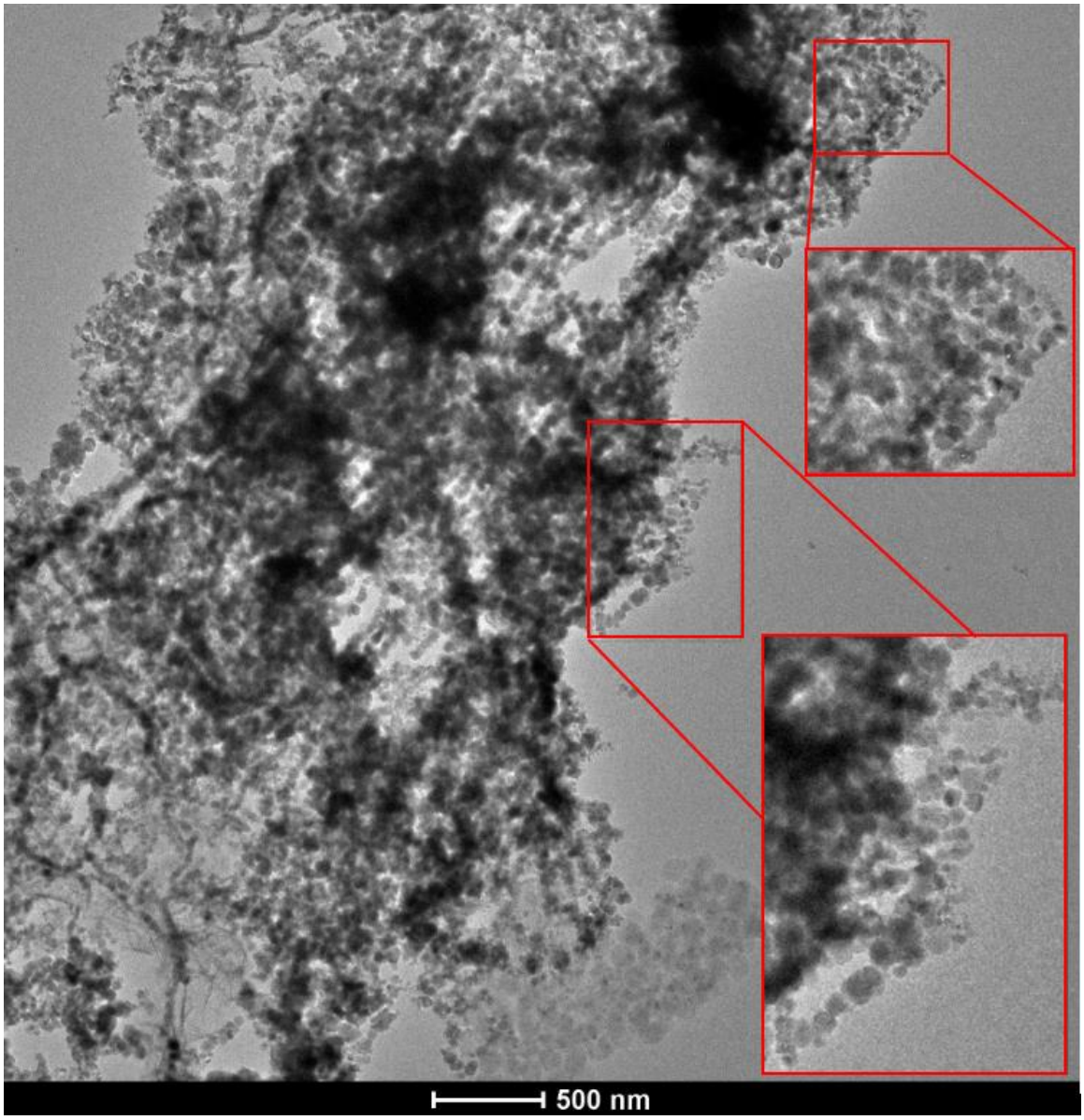


Figure 23. AE001 metallic iron nanoparticle superstructure with silica coating. Dark areas are iron while lighter areas are either iron oxide or silica coating/nanobeads. Insets give a 2x zoom view of agglomeration and coating adherence

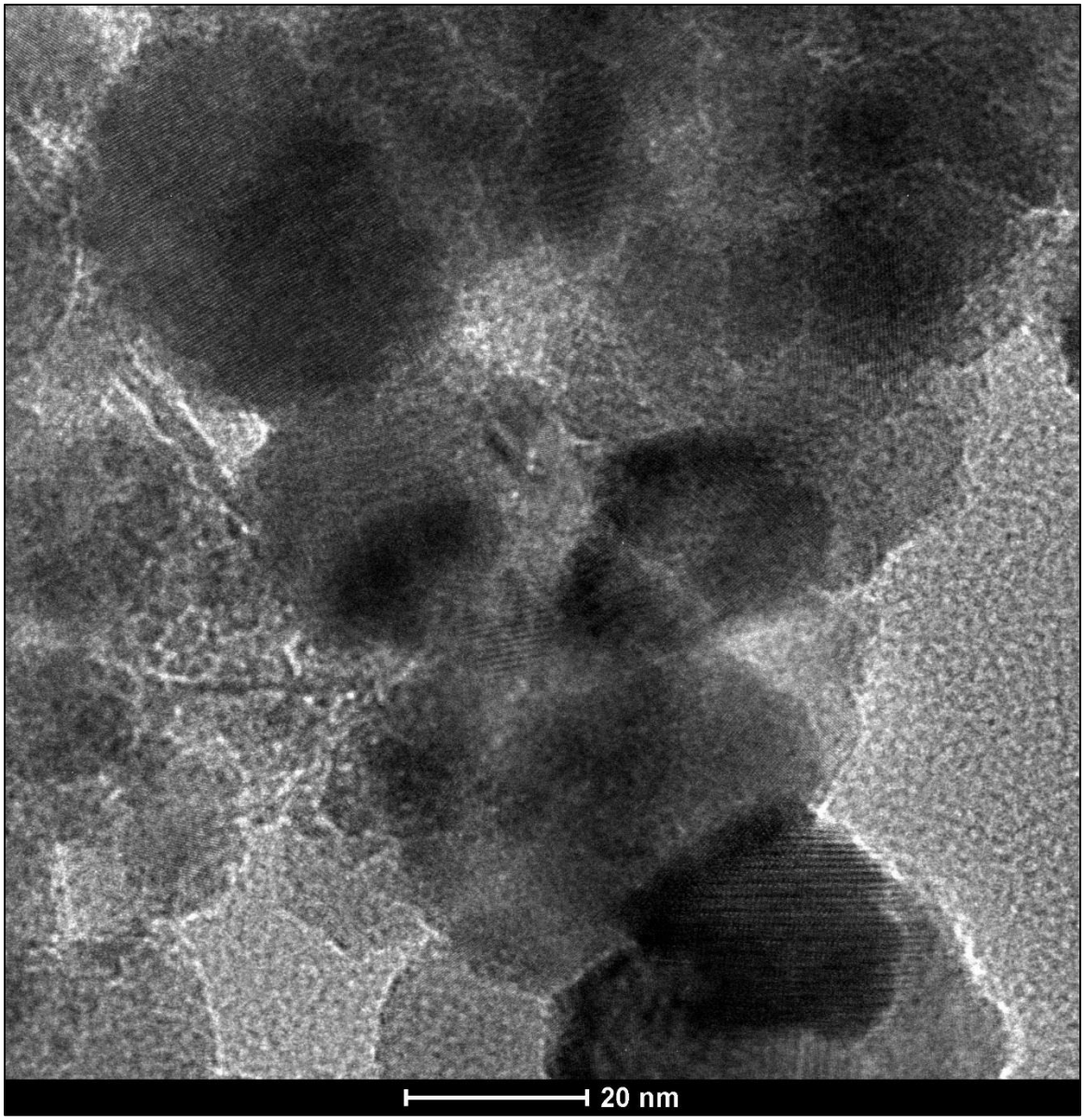


Figure 24. Agglomeration of AE001 metallic iron nanoparticles at a smaller scale length. Both crystalline metallic iron and crystalline iron oxide are apparent

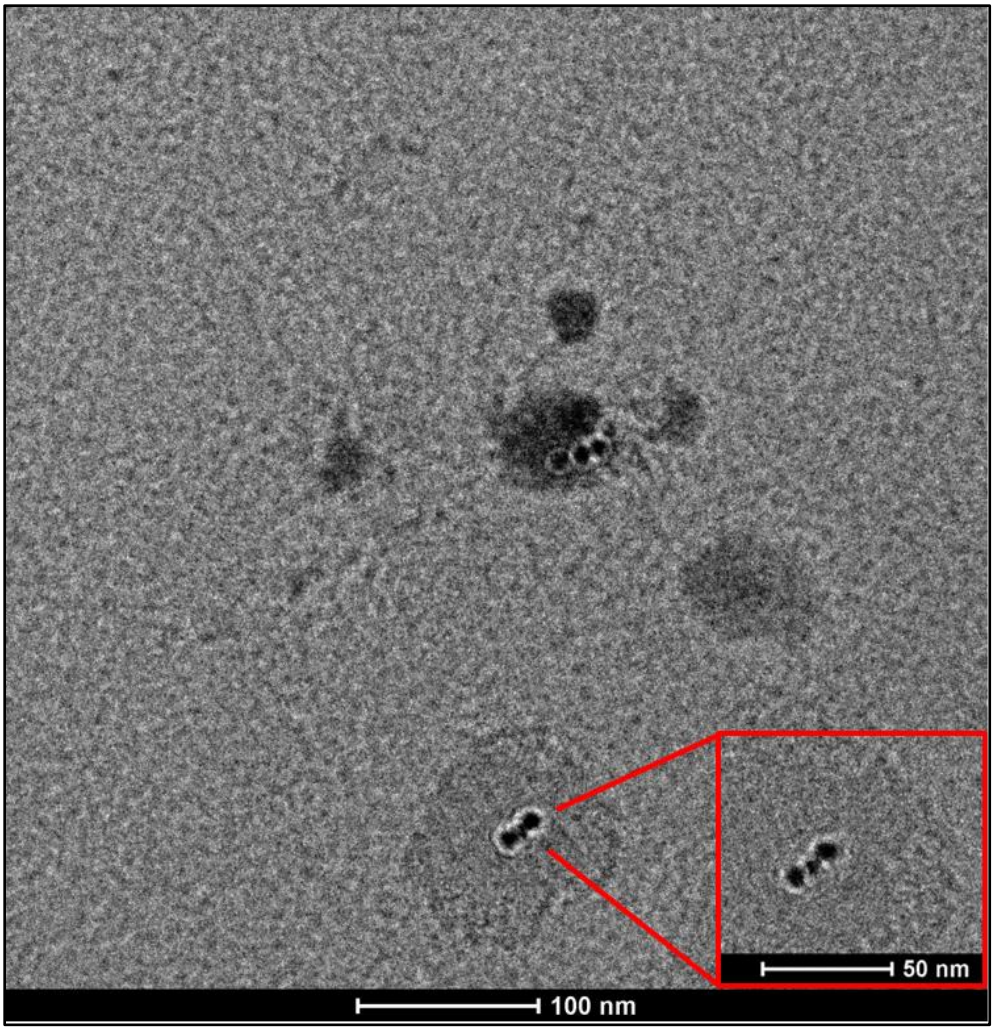


Figure 25. Transmission electron microscopy (TEM) of AE003 uncoated metallic iron nanoparticles. Dark areas are iron while lighter areas are of an iron oxide shell caused by oxidation of the nanoparticle surface

Scanning Electron Microscopy (SEM)

Scanning electron microscopy (SEM) images of AE008 metallic iron nanoparticles can be seen in Figures 26-28. AE008 nanoparticles were produced through an $FeCl_3$ reduction synthesis in argon with dropwise $NaBH_4$ solution, vacuum filtered with a Büchner funnel, and dried in a furnace with argon atmosphere. The nanoparticles were uncoated. Unlike AE001 and AE003 transmission electron microscopy (TEM) results that show individual nanoparticles accumulating into larger agglomerates, AE008 SEM displays iron nanomaterial that has physically sintered in a porous mass. An example of this dendritic structure can be seen in Figure 26. The diameter of iron aggregates in Figure 27 ranged between 25-150 nm, with most residing in the 50-80 nm regime. Diameters were determined using ImageJ image processing software. Sintered aggregation can be attributed to the act of drying the nanoparticles; AE001 and AE003 that remained in solution and were not filtered or dried did not display this behavior. Figure 28 provides a more comprehensive view of the sintered aggregate superstructure. Diameters were also in the 50-80 nm regime and possessed a relatively uniform size distribution.

Finally, Figure 28a) shows an SEM image of sintered iron nanoparticle aggregation, while Figure 28b) displays the backscattered electron image of the same region. Higher-energy backscattered electrons probe deeper than the secondary electrons typically used to construct SEM images [46, 47], allowing for information about the sintered aggregate core to be discerned. When employed in tandem with SEM imaging data to characterize the structures' surface, these combined imaging modalities can be used to determine core-shell structure and size. Site 1 in Figure 28 was measured to have a total diameter of 65 nm with an inner diameter of 41 nm, equating to an outer iron oxide shell thickness of approximately 12 nm. Site 2 had a total diameter of 255 nm with an inner diameter of 205 nm, equating to a shell thickness of approximately 25 nm.

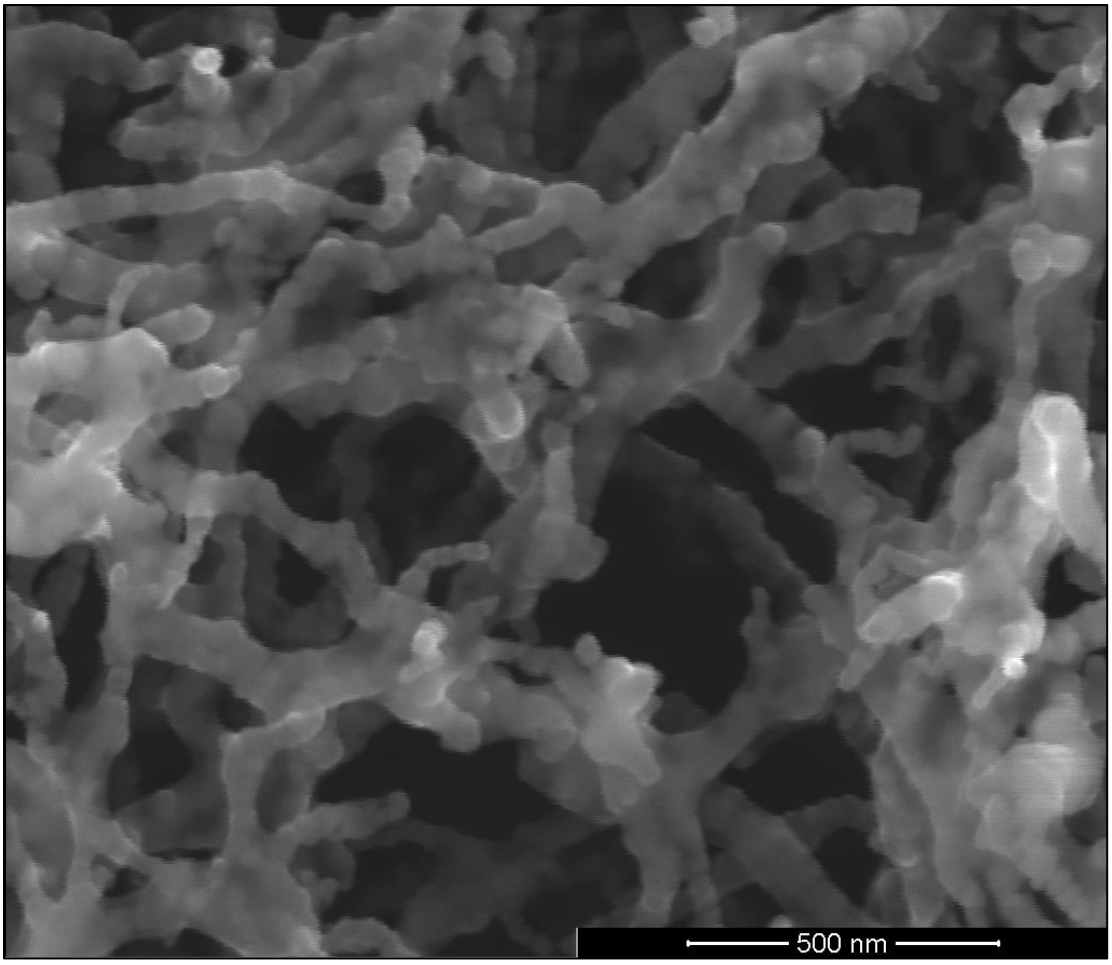


Figure 26. SEM image of AE008 metallic iron nanoparticles arranging as sintered aggregates

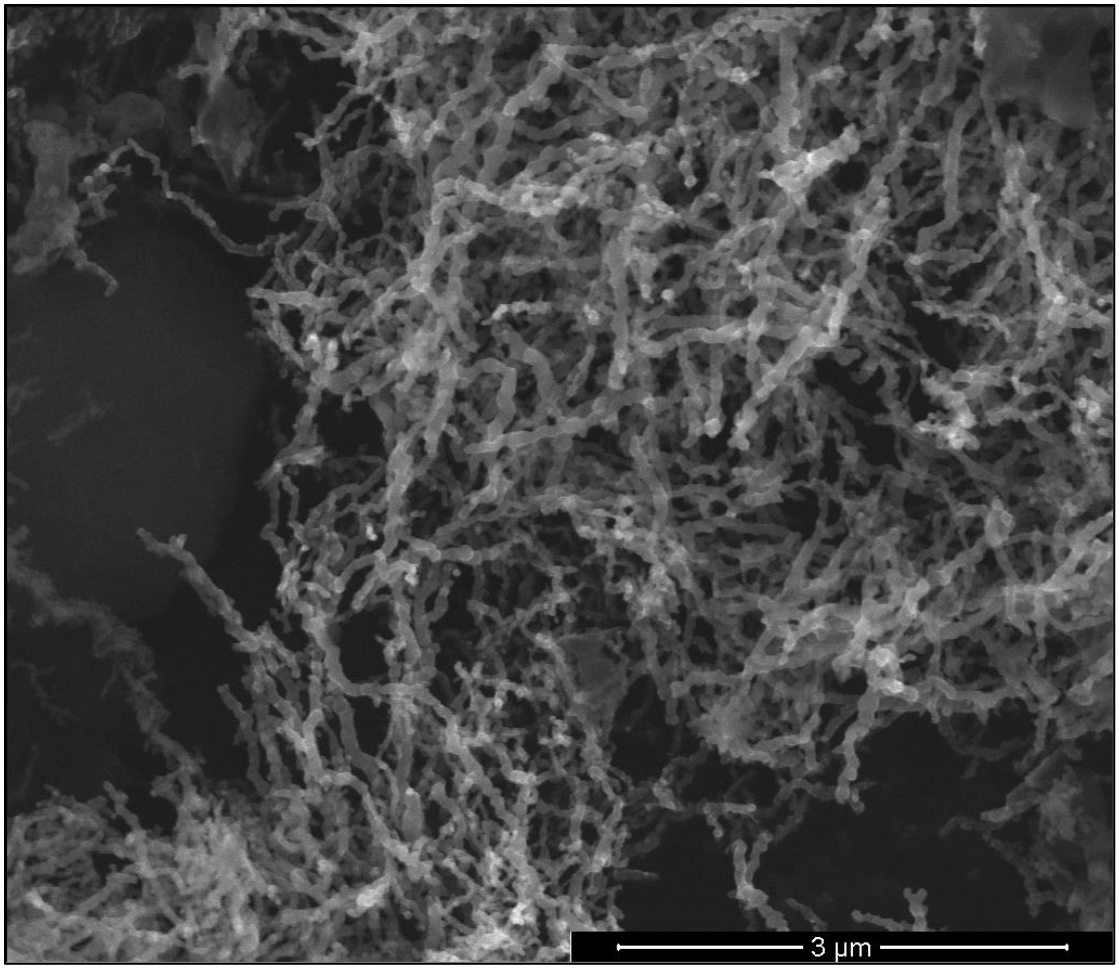


Figure 27. SEM image of AE008 metallic iron nanoparticles arranging as sintered aggregates

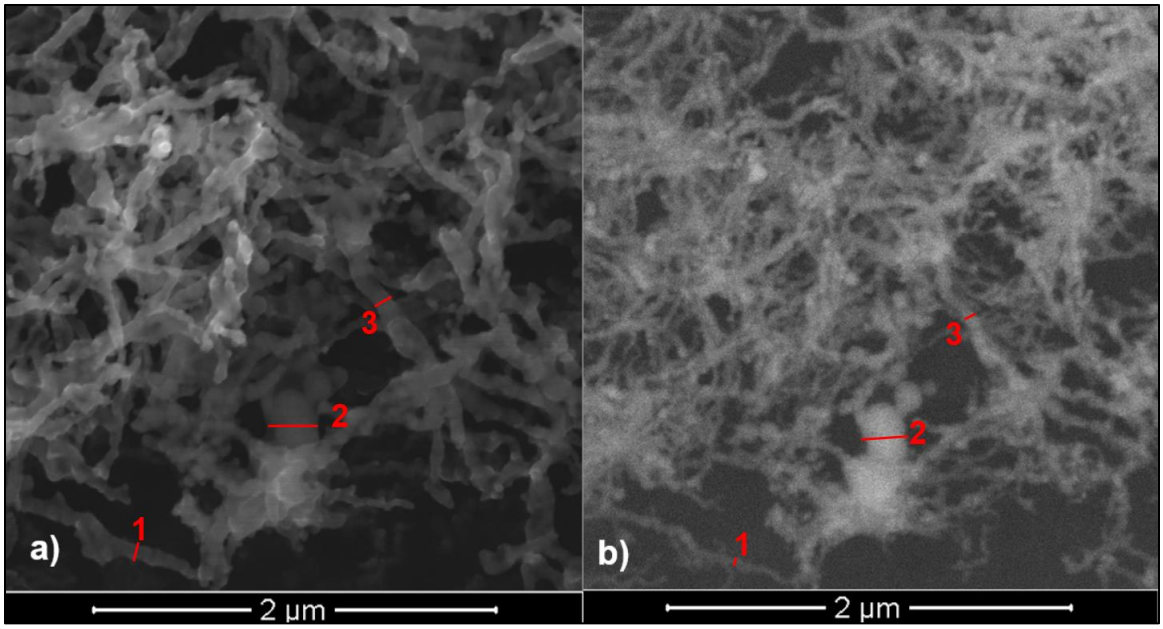


Figure 28. a) SEM image of AE008 metallic iron nanoparticles arranging as sintered aggregates b) Backscattered electron image of same region allowing for differentiation between core and shell. Numbered areas indicate the location of core-shell diameter measurements

Site 3 had a total diameter of 81 nm with an inner diameter of 47 nm, meaning the outer iron oxide shell was approximately 17 nm in thickness. The thickness of the sintered aggregate iron oxide shell increased as metallic iron core thickness increased.

X-ray diffraction (XRD)

X-ray diffraction (XRD) was used to determine the crystallinity of the newly synthesized iron nanoparticles, and results can be seen in Figures 29-31. An amorphous peak at lower angles is attributed to the vacuum grease used to mount the nanoparticle powder. The only discernible diffraction peak in AE005's XRD spectrum (Figure 29) is that of metallic α-Fe [20, 22, 48-50], as evidenced by the characteristic peak at 44.9˚ (Joint Committee on Powder Diffraction Standards JCPDS # 87-0722).

Nanoparticle crystallite size, τ, can be estimated through use of the Scherrer equation:

$$\tau = \frac{K\lambda}{\beta cos\theta} \quad (1)$$

where K is a dimensionless shape factor (typically 0.9), λ is the X-ray wavelength, β is the full width at half maximum (FWHM) in radians, and θ is the Bragg angle in radians. Nanoparticle crystallite size for each XRD sample as determined through the Scherrer equation is tabulated below in Table 2. The crystallite size of AE005 was calculated to be 8.6 nm.

The XRD spectra of AE007 iron nanoparticles at three separate stages of ambient oxidation (as-made, 2-hr, 48-hr) are displayed in Figure 30. Characteristic metallic α-Fe peaks at 44.9˚ and 65.1˚ (JCPDS # 87-0722) are detected in all three samples. Contributions from the metallic aluminum sample holder (JCPDS # 89-4037) can be seen in the spectra for the 2-hr and 48-hr oxidized samples at 38.0˚ and 78.0˚ [51].

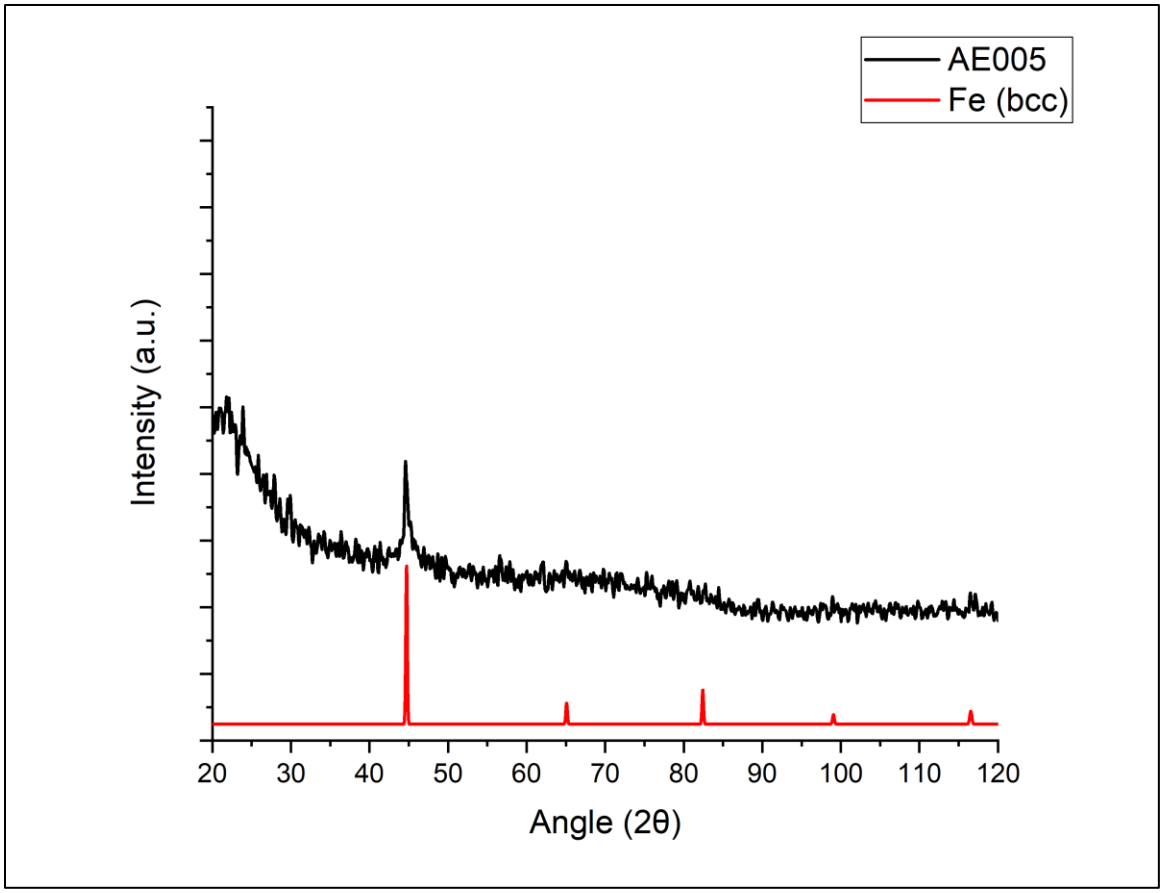


Figure 29. XRD results for AE005 metallic iron nanoparticles synthesized through dropwise $FeCl_3$ reduction with $NaBH_4$. Below the sample spectrum is the pattern for body-centered cubic (bcc) α-Fe (JCPDS # 87-0722)

Table 2. Iron nanoparticle crystallite size determined through Scherrer equation calculations

Sample	Crystallite Size (nm)
AE005	8.6
AE007 0-hr	31.8
AE007 2-hr	47.0
AE007 48-hr	40.9
AE008	20.2

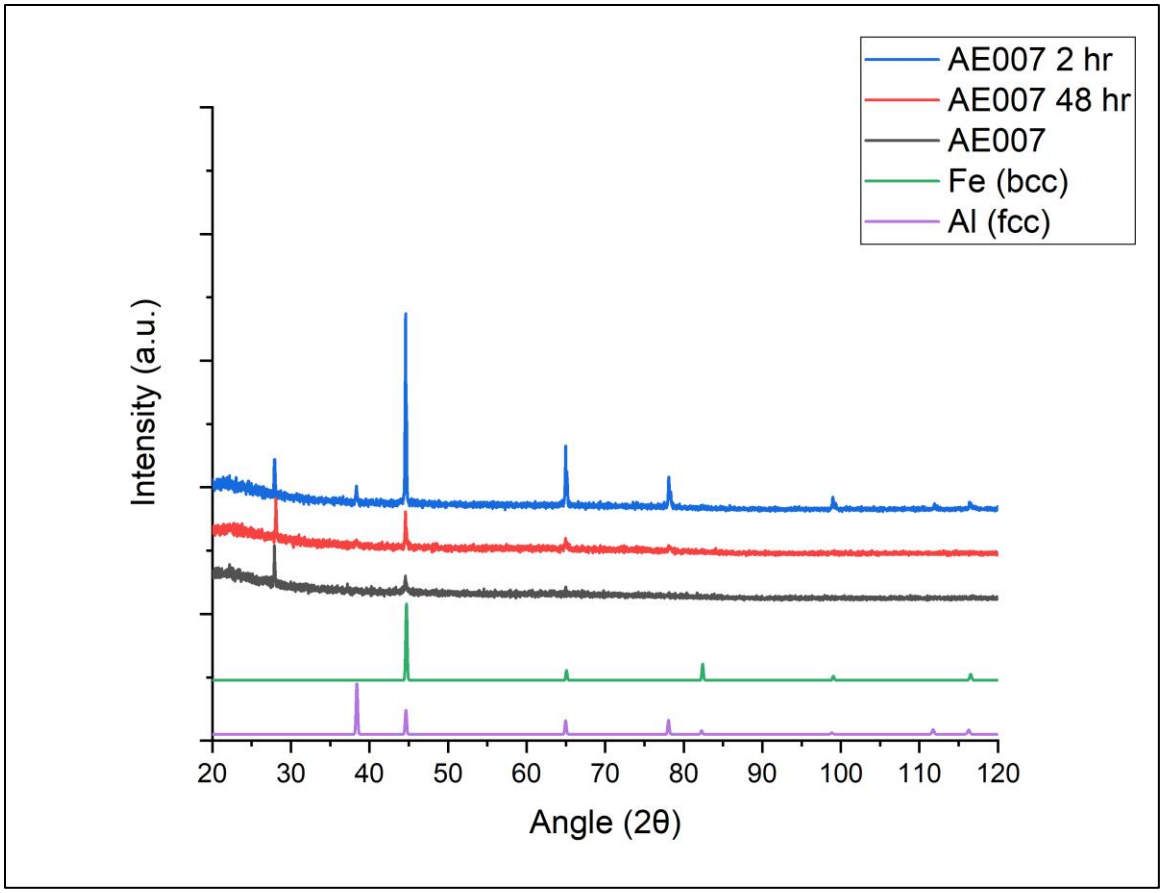


Figure 30. XRD results for AE007 metallic iron nanoparticles synthesized through dropwise $FeCl_3$ reduction with $NaBH_4$. Samples were characterized at three separate lengths of ambient oxidation. Below the sample spectra are the patterns for body-centered cubic (bcc) α-iron (JCPDS # 87-0722) and face-centered cubic (fcc) metallic aluminum (JCPDS # 89-4037)

An unidentified peak at 28.1˚ is attributed to unidentified reaction products. No new peaks in the x-ray diffraction spectra were detected as ambient oxidation progressed. Crystallite size of AE007 (as-made, 2-hr, 48-hr) was determined to be 31.8 nm, 47.0 nm, and 40.9 nm, respectively, leading to an overall average of 39.9 nm across sample variants.

XRD results of as-made uncoated AE008 nanoparticles (Figure 31) confirm the presence of metallic α-Fe with characteristic peaks at 44.9˚ and 65.1˚ (JCPDS # 87-0722). Additional peaks at 38.0˚ and 78.0˚ are contributions from the metallic aluminum sample holder used to hold the particles during characterization (JCPDS # 89-4037). Along with an amorphous peak at low angles ascribed to vacuum grease, supplementary peaks at 27.9˚ and 28.1˚ are attributed to unidentified reaction products [52]. Crystallite size of AE008 was calculated to be 20.2 nm.

No reflections due to iron oxides (Fe_3O_4, γ-Fe_2O_3, α-Fe_2O_3) were observed in any sample. Since XRD is not sensitive enough to detect the thin oxide and amorphous layers that surround the crystalline iron core of the nanoparticles [50, 53], Mössbauer spectroscopy was employed to give a more detailed understanding of the iron ions' local chemical environment throughout the various stages of ambient oxidation.

Dynamic Light Scattering (DLS)

Dynamic light scattering results (DLS) are separated into three differently weighted categories: intensity, volume, and number distributions. Intensity distributions are weighted according to the amplitude of each similarly sized particle group's scattering from the DLS instrument's laser. Intensity distributions are sensitive to being skewed towards agglomerates, as scattering intensity is correlated with particle radius.

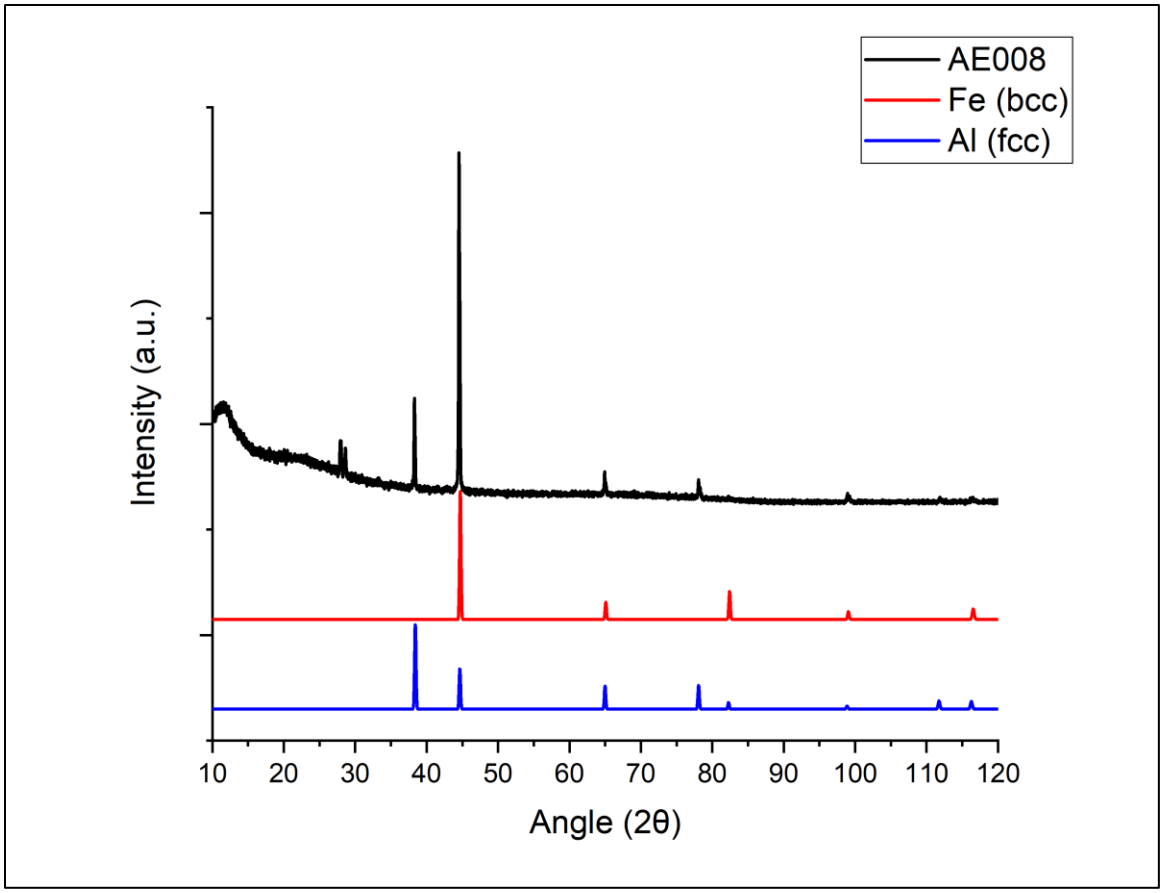


Figure 31. XRD results for AE008 metallic iron nanoparticles synthesized through dropwise $FeCl_3$ reduction with $NaBH_4$. Below the sample spectrum are the patterns for body-centered cubic (bcc) α-iron (JCPDS # 87-0722) and face-centered cubic (fcc) metallic aluminum (JCPDS # 89-4037)

Despite this sensitivity, intensity distribution remains the best mode of reporting these DLS results; the resultant graph displays the entire range of detected nanoparticles, agglomerates, and larger macrostructures.

Number distribution measurements, on the other hand, display the relative proportion of each grouping of differently sized particles. This method is similar to that of visual inspection using a microscope or other counting based techniques. Therefore, smaller sized particles dominate number distribution results because many more of them exist when compared with the sample's larger agglomerates. Conversely, volume distribution is a measurement weighted by the relative proportion of each particle's mass or size rather than its scattering. Particle agglomerates and macrostructures are orders of magnitude larger than the nanoparticles at the subject of this investigation and thus compose a majority proportion of particle volume. Consequently, agglomerates dominate volume distribution results. Intensity distribution results are reported in the paragraphs below, with additional volume and number distribution graphs and data appearing in their sample's corresponding figure and table.

Sample AE001 yielded four distribution peaks that can be seen in Figure 32. Intensity distribution shows particle sizes of 23.1 nm ± 1.7 nm (nanoparticles), 137.5 nm ± 25.3 nm (moderate agglomerates), 667.3 nm ± 117.4 nm (large agglomerates), and 10,910.8 nm ± 763.0 nm (large macrostructures). AE001 DLS results, including supplementary volume and number distribution values, are organized in Table 3.

Sample AE003 yielded three distribution peaks that can be seen in Figure 33. Intensity distribution shows particle sizes of 35.5 nm ± 2.4 nm (nanoparticles), 887.5 nm ± 152.1 nm (large agglomerates), and 43,047.2 nm ± 9,303.6 nm (large macrostructures). AE003 DLS, including supplementary volume and number distribution values, results are organized in Table 4.

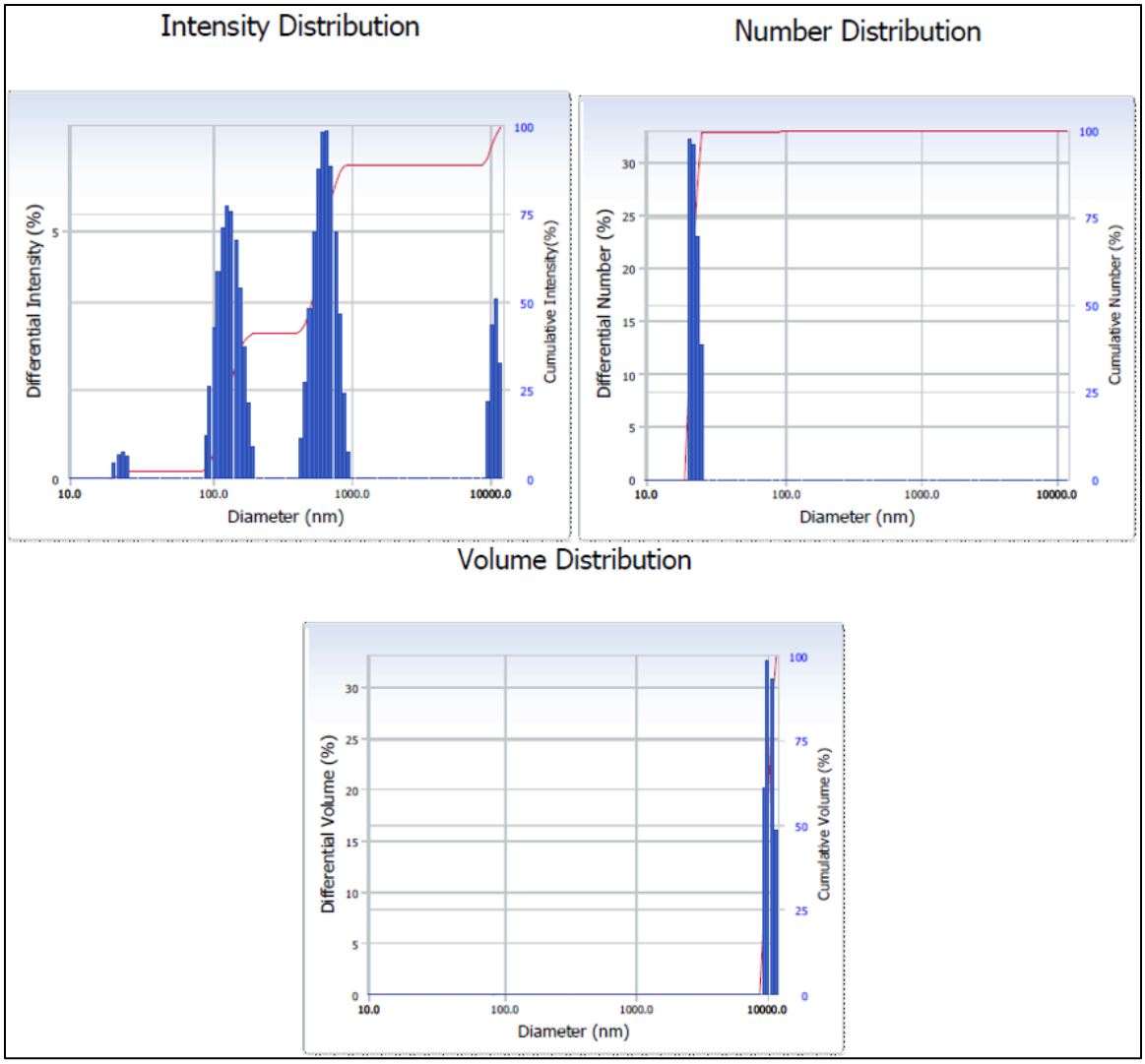


Figure 32. AE001 DLS results

Table 3. Table of AE001 DLS results

Intensity Distribution			Volume Distribution			Number Distribution		
Peak	Diameter (nm)	Std. Dev.	Peak	Diameter (nm)	Std. Dev.	Peak	Diameter (nm)	Std. Dev.
1	23.1	1.7	1	22.7	1.7	1	22.3	1.7
2	137.5	25.3	2	124.6	22.4	2	114.6	18.5
3	667.3	117.4	3	608.8	106.4	3	561.3	89.8
4	10,910.8	763.0	4	10,748.2	760.7	4	10,591.2	741.2
Average	1,535.8	3,252.9	Avg.	10,711.7	982.8	Avg.	22.6	28.9

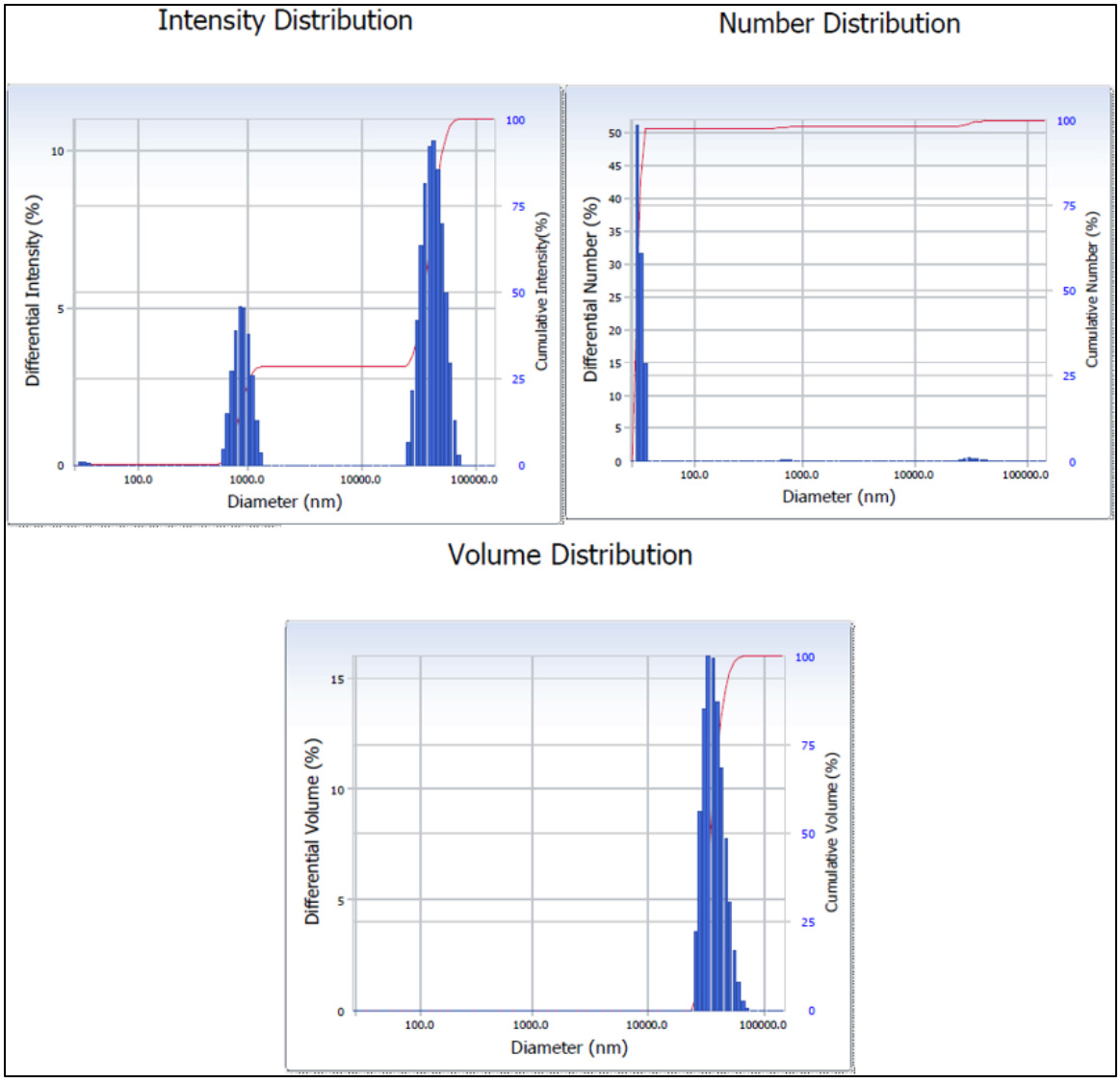


Figure 33. AE003 as-made DLS results

Table 4. Table of AE003 as-made DLS results

Intensity Distribution			Volume Distribution			Number Distribution		
Peak	Diameter (nm)	Std. Dev.	Peak	Diameter (nm)	Std. Dev.	Peak	Diameter (nm)	Std. Dev.
1	35.5	2.4	1	35.0	2.3	1	34.6	2.2
2	887.5	152.1	2	813.9	137.9	2	114.6	117.4
3	43,047.2	9,303.6	3	37,663.9	7,880.8	3	33,749.3	6,190.0
Average	31,059.2	20,545.0	Avg.	37,663.8	7,881.0	Avg.	661.4	4,619.5

Sample AE004 yielded four distribution peaks that can be seen in Figure 34. Intensity distribution shows particle sizes of 10.4 nm ± 0.4 nm (nanoparticles), 133.5 nm ± 19.3 nm (moderate agglomerates), 485.0 nm ± 92.8 nm (large agglomerates), and 41,458.3 nm ± 6,113.9 nm (large macrostructures). AE004 DLS results, including supplementary volume and number distribution values, are organized in Table 5.

Sample AE006 yielded five distribution peaks that can be seen in Figure 35. The intensity distribution shows particle sizes of 10.4 nm ± 0.4 nm (nanoparticles), 209.4 nm ± 61.7 nm (moderate agglomerates), 548.9 nm ± 111.1 nm (large agglomerates), 1,855.7 nm ± 566.1 nm (moderate macrostructures), and 26,434.0 nm ± 2,869.8 nm (large macrostructures). AE006 DLS results, including supplementary volume and number distribution values, are organized in Table 6.

Sample AE007 yielded two distribution peaks that can be seen in Figure 36. Intensity distribution shows particle sizes of 327.2 nm ± 125.5 nm (moderate agglomerates), and 5,676.6 nm ± 5,802.5 nm (large macrostructures). AE007 DLS, including supplementary volume and number distribution values, results are organized in Table 7.

Sample AE008 yielded three distribution peaks that can be seen in Figure 37. Intensity distribution shows particles sizes of 51.7 nm ± 7.6 nm (nanoparticles), 1,676.2 nm ± 637.3 nm (large agglomerates), and 129,998 nm ± 54,494.8 nm (bulk material). AE008 DLS, including supplementary volume and number distribution values, results are organized in Table 8.

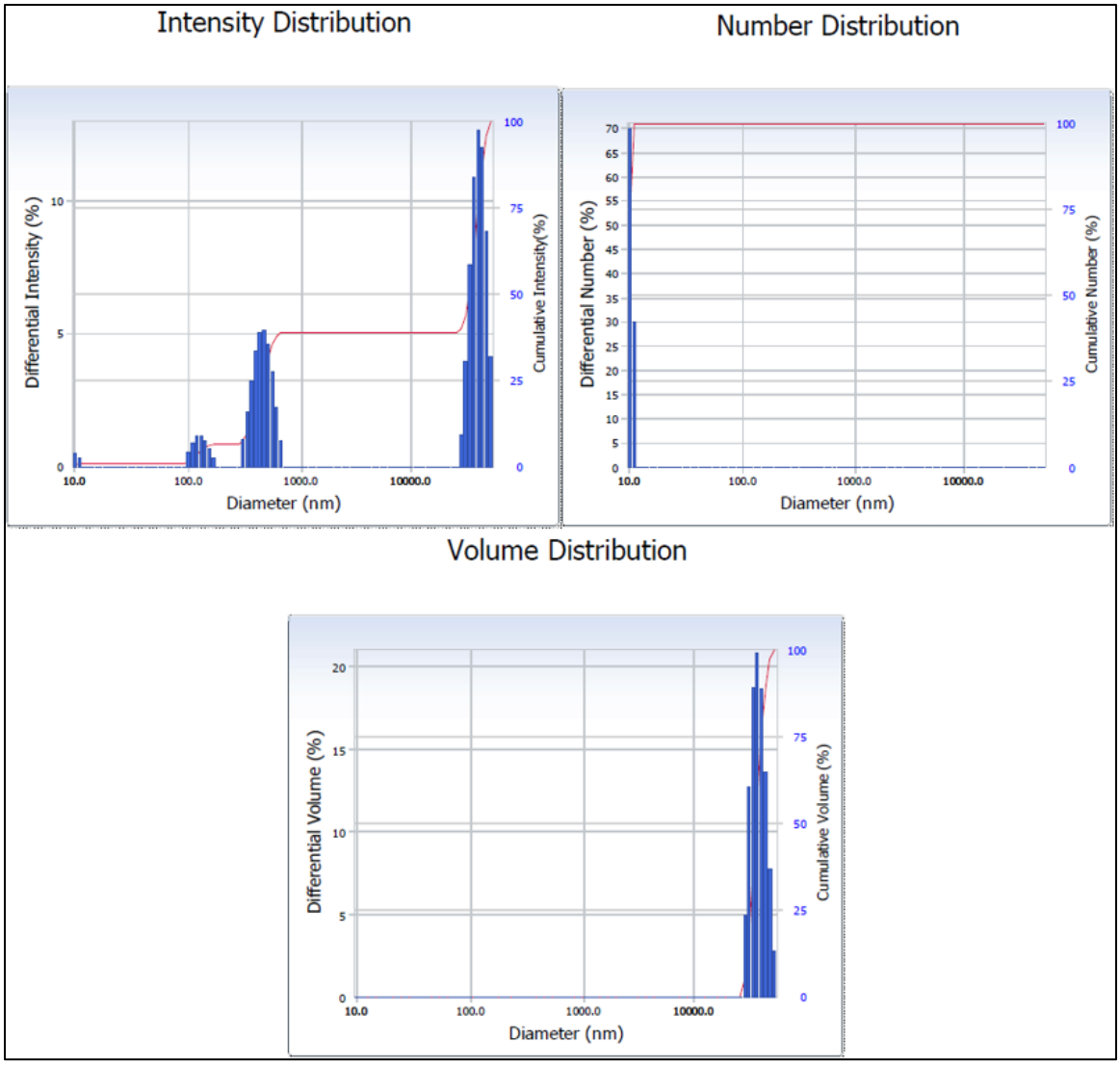


Figure 34. AE004 DLS results

Table 5. Table of AE004 DLS results

Intensity Distribution			Volume Distribution			Number Distribution		
Peak	Diameter (nm)	Std. Dev.	Peak	Diameter (nm)	Std. Dev.	Peak	Diameter (nm)	Std. Dev.
1	10.4	0.4	1	10.3	0.4	1	10.3	0.4
2	133.5	19.3	2	125.7	17.6	2	119.4	15.1
3	485.0	92.8	3	435.1	82.6	3	396.5	67.1
4	41,598.3	6,113.9	4	38,894.5	5,878.1	4	36,455.6	5,283.0
Average	25,674.9	20,616.2	Avg.	38,893.8	5,880.2	Avg.	10.3	43.4

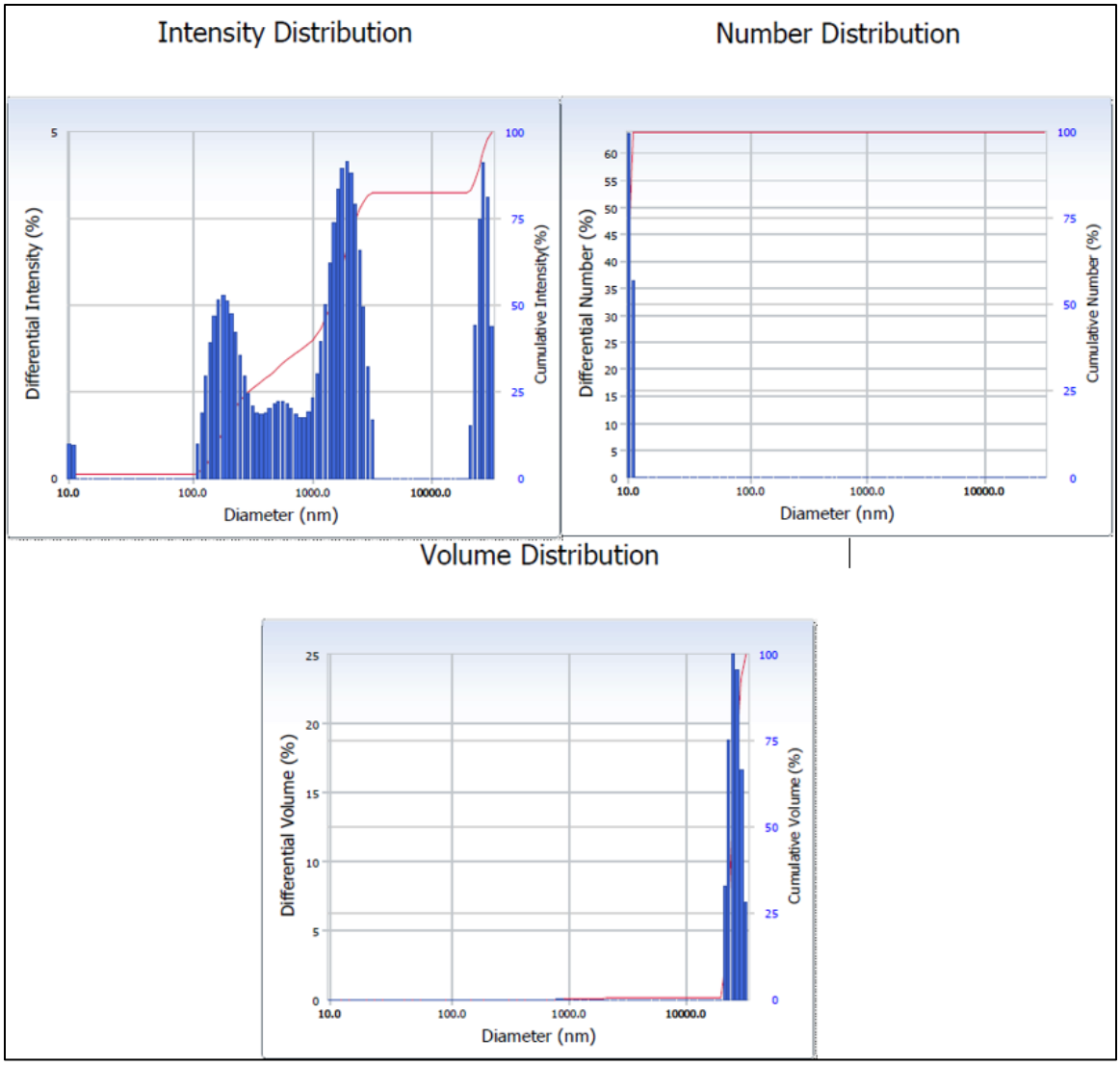


Figure 35. AE006 DLS results

Table 6. Table of AE006 DLS results

Intensity Distribution			Volume Distribution			Number Distribution		
Peak	Diameter (nm)	Std. Dev.	Peak	Diameter (nm)	Std. Dev.	Peak	Diameter (nm)	Std. Dev.
1	10.4	0.4	1	166.1	42.2	1	10.3	0.4
2	209.4	61.7	2	477.9	85.5	2	144.4	28.8
3	548.9	111.1	3	866.1	57.8	3	442.2	66.9
4	1,855.7	566.1	4	1,552.1	422.8	4	1,019.6	275.1
5	26,434.0	2,869.8	5	25,480.6	2,846.1	5	24,562.5	2,702.3
Average	5,596.4	9,711.2	Avg.	25,375.5	3,256.3	Avg.	10.3	13.1

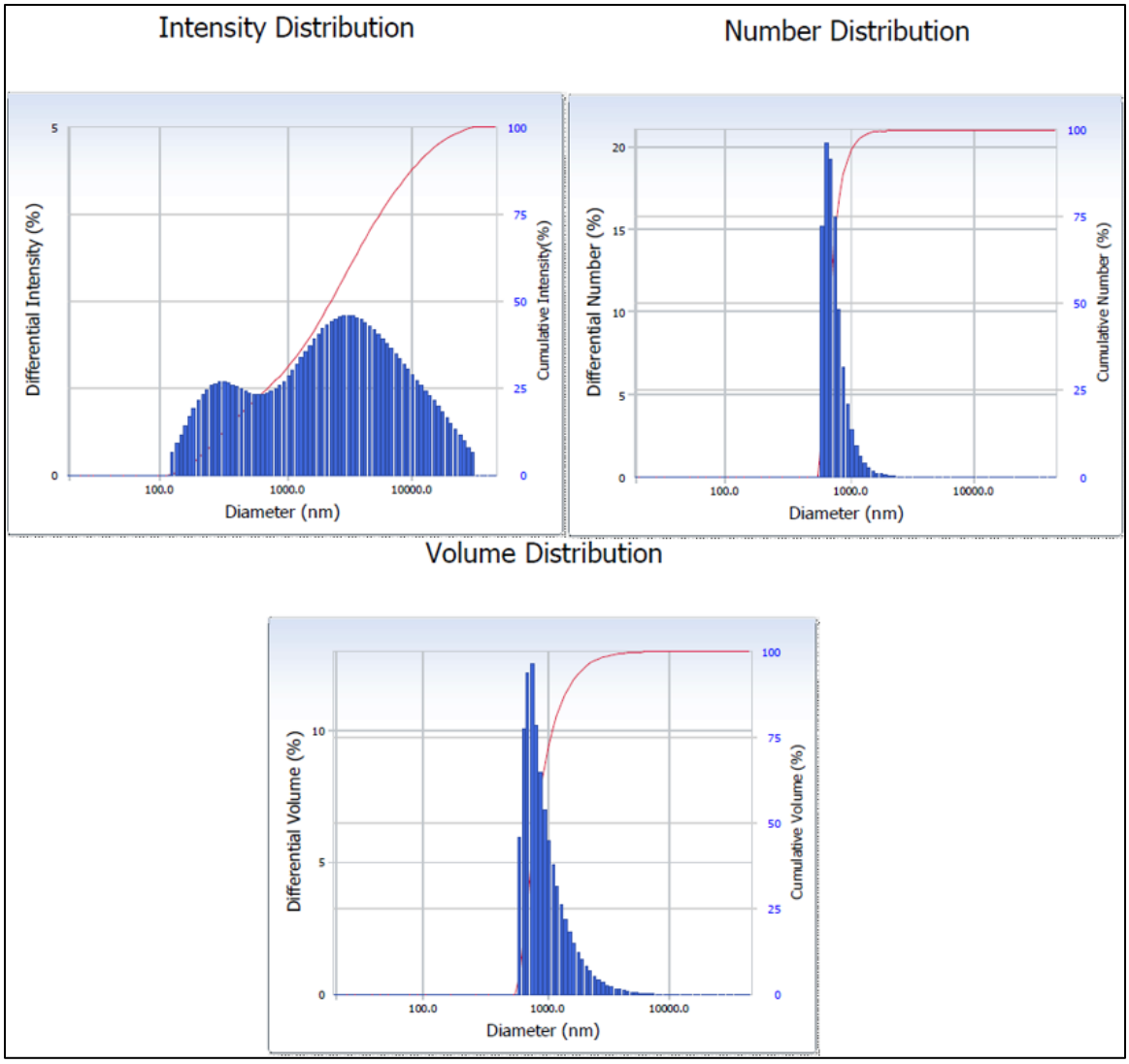


Figure 36. AE007 DLS results

Table 7. Table of AE007 DLS results

Intensity Distribution			Volume Distribution			Number Distribution		
Peak	Diameter (nm)	Std. Dev.	Peak	Diameter (nm)	Std. Dev.	Peak	Diameter (nm)	Std. Dev.
1	327.2	125.5	1	221.2	76.4	1	178.0	42.2
2	5,676.6	5,802.5	2	1,069.9	627.0	2	790.7	192.6
Average	4,539.9	5,595.3	Avg.	1,069.9	627.0	Avg.	790.7	192.6

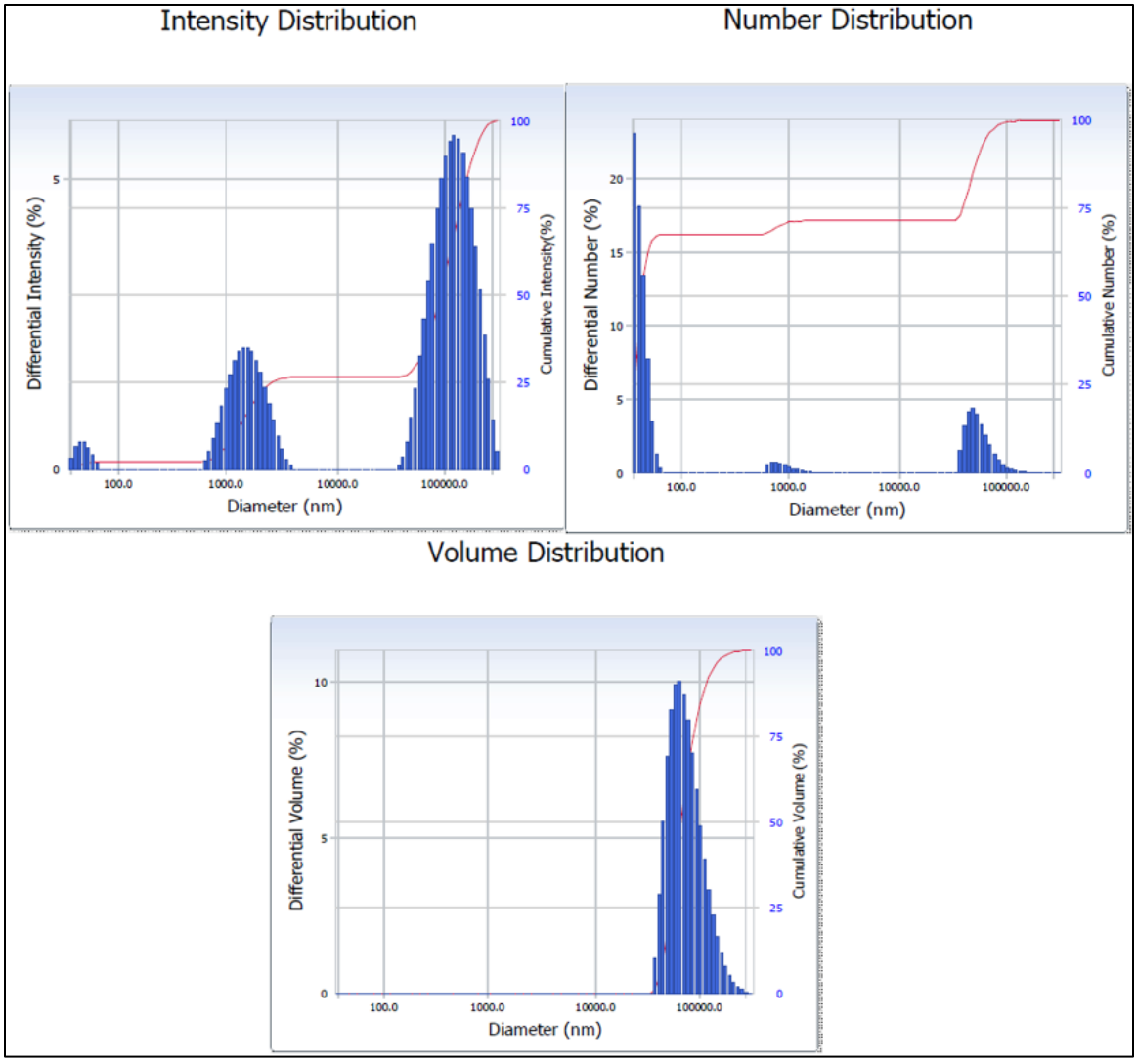


Figure 37. AE008 DLS results

Table 8. Table of AE008 DLS results

Intensity Distribution			Volume Distribution			Number Distribution		
Peak	Diameter (nm)	Std. Dev.	Peak	Diameter (nm)	Std. Dev.	Peak	Diameter (nm)	Std. Dev.
1	51.7	7.6	1	48.0	6.9	1	45.5	5.8
2	1,676.2	637.3	2	1,136.0	401.0	2	891.4	228.9
3	129,998	53,498.8	3	79,100.9	32,286.5	3	57,732.4	16,878.1
Average	96,118.6	72,882.2	Avg.	79,100.9	32,286.5	Avg.	16,431.2	27,486.7

Sample AE009 yielded three distribution peaks that can be seen in Figure 38. Intensity distribution shows particle sizes of 73.9 nm ± 9.1 nm (nanoparticles), 1,370.3 nm ± 211.7 nm (large agglomerates), and 69,149.5 nm ± 15,062.1 nm (bulk material). AE009 DLS, including supplementary volume and number distribution values, results are organized in Table 9.

Sample AE010 yielded three distribution peaks that can be seen in Figure 39. Intensity distribution shows particle sizes of 66.4 nm ± 8.2 nm (nanoparticles), 1,936.7 nm ± 729.9 nm (large agglomerates), and 158,225 nm ± 82,870.5 nm (bulk material). AE010 DLS, including supplementary volume and number distribution values, results are organized in Table 10.

Sample AE011 yielded five distribution peaks that can be seen in Figure 40. Intensity distribution shows particle sizes of 36.9 nm ± 4.7 nm (nanoparticles), 154.9 nm ± 45.5 nm (moderate agglomerates), 512.4 nm ± 123.5 nm (large agglomerates), 4,839.4 nm ± 1,114.3 nm (large macrostructures), and 155,720 nm ± 24,450.4 nm (bulk material). AE011 DLS results, including supplementary volume and number distribution values, are organized in Table 11.

Sample AE013B yielded three distribution peaks that can be seen in Figure 41. Intensity distribution shows particle sizes of 46.8 nm ± 5.0 nm (nanoparticles), 1,250.1 nm ± 211.3 nm (large agglomerates), and 83,568.1 nm ± 18,267.0 nm (bulk material). AE013B DLS, including supplementary volume and number distribution values, results are organized in Table 12.

Sample AE014A yielded three distribution peaks that can be seen in Figure 42. Intensity distribution shows particle sizes of 103.3 nm ± 17.5 nm (nanoparticles), 3,281.2 nm ± 1,268.1 nm (large agglomerates), and 169,317 nm ± 10,578.9 nm (bulk material). AE014A DLS, including supplementary volume and number distribution values, results are organized in Table 13.

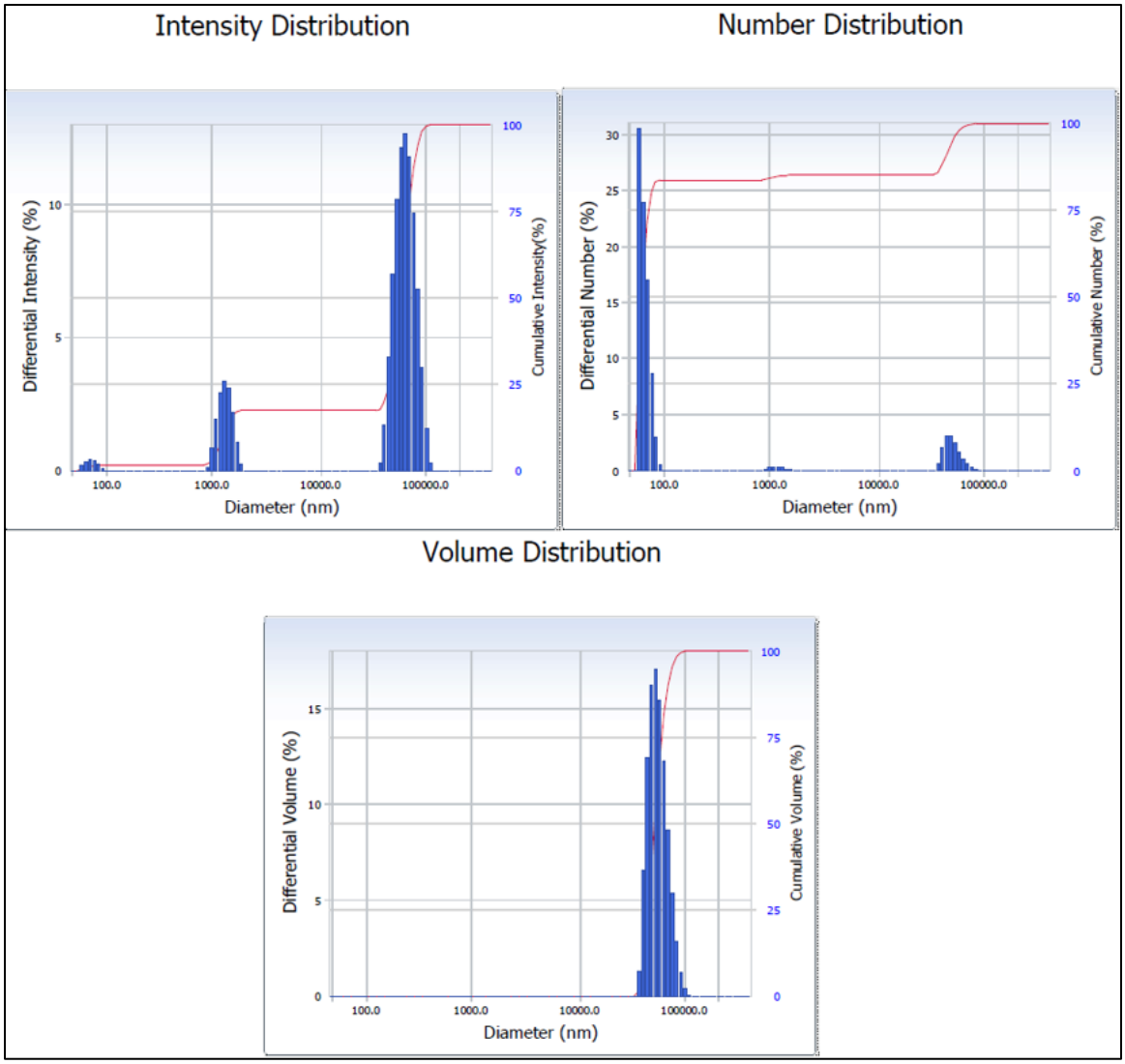


Figure 38. AE009 DLS results

Table 9. Table of AE009 DLS results

Intensity Distribution			Volume Distribution			Number Distribution		
Peak	Diameter (nm)	Std. Dev.	Peak	Diameter (nm)	Std. Dev.	Peak	Diameter (nm)	Std. Dev.
1	73.9	9.1	1	70.0	8.6	1	67.2	7.5
2	1,370.3	211.7	2	1,277.0	195.4	2	1,197.5	171.8
3	69,149.5	15,062.1	3	60,337.3	12,775.0	3	53,881.0	10,063.6
Average	57,324.3	29,163.6	Avg.	60,337.2	12,775.2	Avg.	8,050.2	19,494.5

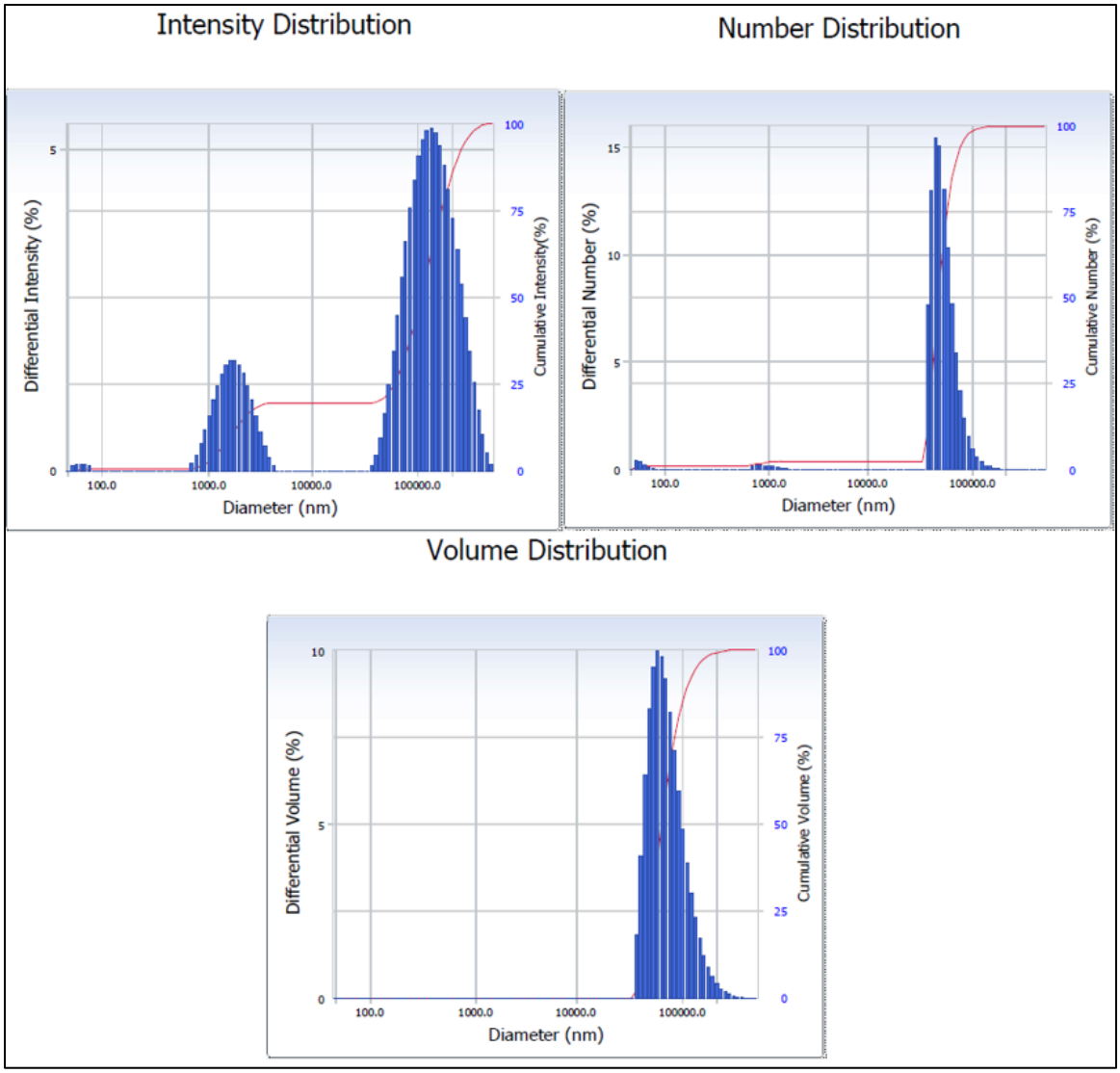


Figure 39. AE010 DLS results

Table 10. Table of AE010 DLS results

Intensity Distribution			Volume Distribution			Number Distribution		
Peak	Diameter (nm)	Std. Dev.	Peak	Diameter (nm)	Std. Dev.	Peak	Diameter (nm)	Std. Dev.
1	66.4	8.2	1	63.6	7.7	1	61.1	6.7
2	1,936.7	729.9	2	1,305.9	467.5	2	1,016.1	265.6
3	158,225	82,870.5	3	79,312.9	36,882.1	3	55,798.5	16,767.2
Average	127,751	96,769.5	Avg.	75,312.9	36,882.1	Avg.	54,484.1	18,582.4

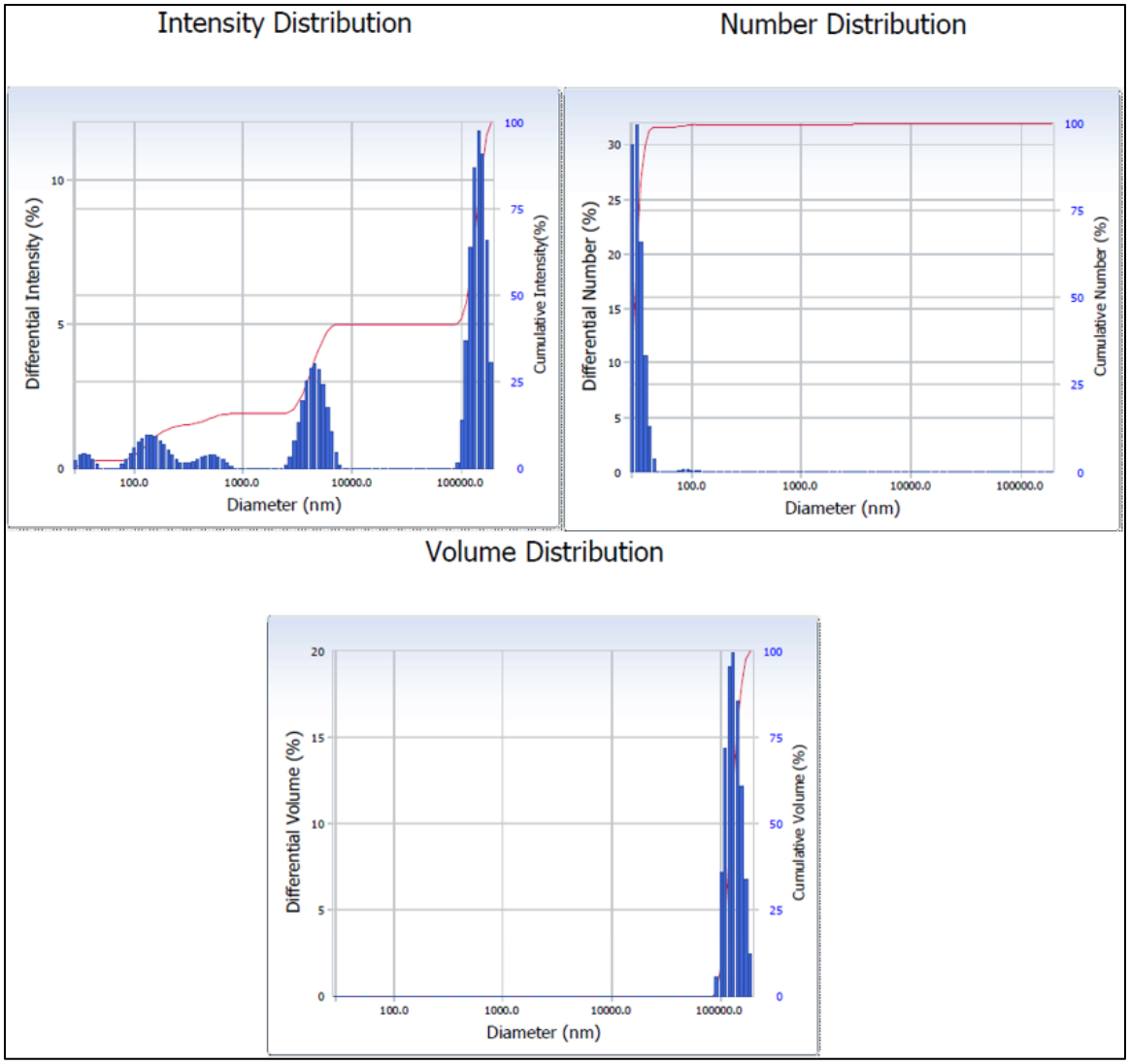


Figure 40. AE011 DLS results

Table 11. Table of AE011 DLS results

Intensity Distribution			Volume Distribution			Number Distribution		
Peak	Diameter (nm)	Std. Dev.	Peak	Diameter (nm)	Std. Dev.	Peak	Diameter (nm)	Std. Dev.
1	36.9	4.7	1	35.2	4.3	1	33.9	3.8
2	154.9	45.5	2	122.2	32.8	2	104.0	22.4
3	512.4	123.5	3	442.8	102.6	3	387.9	77.5
4	4,839.4	1,114.3	4	4,128.1	954.9	4	3,601.3	740.9
5	155,720	24,450.4	5	144,155	23,390.8	5	133,807	20,803.3
Average	92,394.2	77,507.8	Avg.	144,152	23,400.0	Avg.	156.1	4,023.2

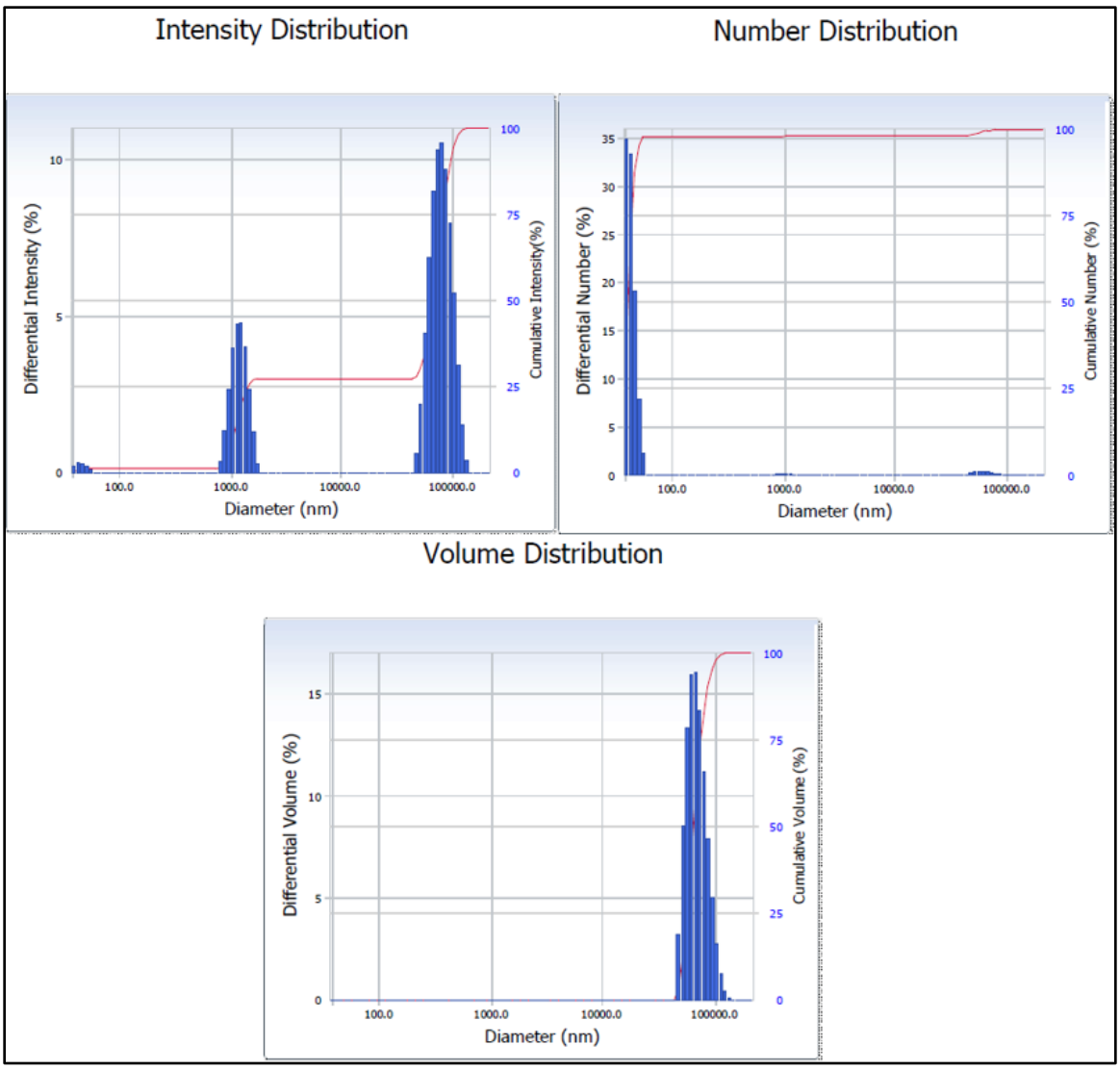


Figure 41. AE013B DLS results

Table 12. Table of AE013B DLS results

Intensity Distribution			Volume Distribution			Number Distribution		
Peak	Diameter (nm)	Std. Dev.	Peak	Diameter (nm)	Std. Dev.	Peak	Diameter (nm)	Std. Dev.
1	46.8	5.0	1	45.3	4.6	1	44.1	4.1
2	1,250.1	211.3	2	1,148.8	192.6	2	1,064.8	165.4
3	83,568.1	18,267.0	3	72,884.0	15,439.0	3	65,132.7	12,095.3
Average	61,082.7	39,863.3	Avg.	72,844.0	15,439.2	Avg.	1,243.6	8,892.6

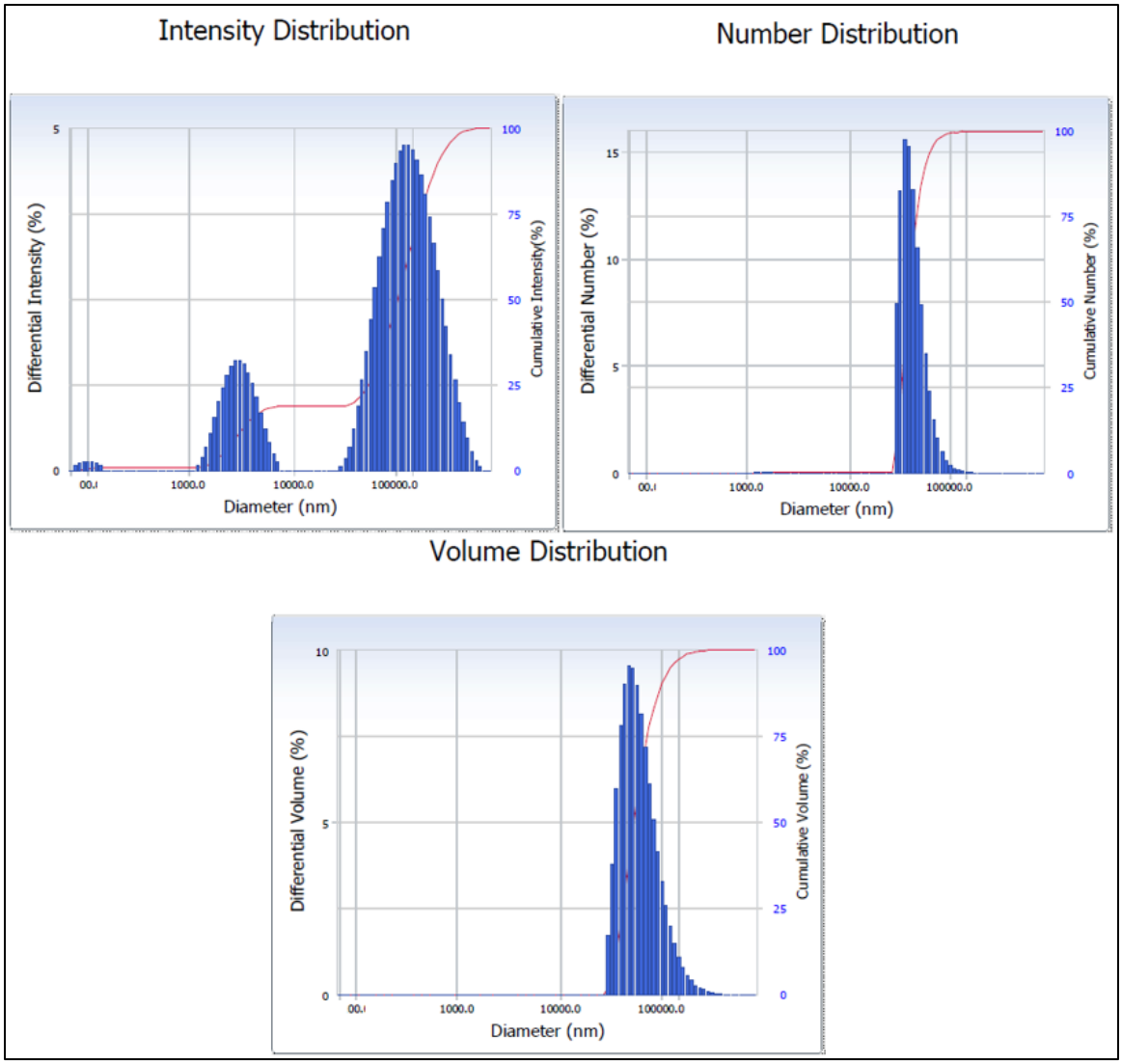


Figure 42. AE014A DLS results

Table 13. Table of AE014A DLS results

Intensity Distribution			Volume Distribution			Number Distribution		
Peak	Diameter (nm)	Std. Dev.	Peak	Diameter (nm)	Std. Dev.	Peak	Diameter (nm)	Std. Dev.
1	103.3	17.5	1	96.0	15.6	1	89.7	12.9
2	3,281.2	1,268.1	2	2,181.4	792.4	2	1,687.0	447.1
3	169,317	10,578.9	3	69,197.2	36,024.8	3	46,451.8	14,628.0
Average	138,391	11,528.8	Avg.	69,197.2	36,024.8	Avg.	46,360.5	14,752.7

All DLS nanoparticle samples (except for AE007) display an initial peak reporting nanoparticle sizes between 10.4-103.3 nm, followed by agglomerates of varying proportions. This initial peak is corroborated with the TEM (AE001 – 20 nm, AE003 – 35 nm) and SEM (AE008 – 50 nm) results previously reported in the imaging section of this dissertation. Agglomeration, however, is prevalent in all samples and is also confirmed with microscopy. Samples that are vacuum filtered and dried in the glovebox furnace, such as AE008, are prone to fusing into sintered aggregates and forming larger structures, i.e. agglomerates. Agglomerates from samples that were left in solution, AE001 and AE003, can be explained by the magnetic nature of the iron nanoparticles and the energetic favorability of coalescing. The silica coating of AE001 also caused cross-linkages to form, leading to aggregation. DLS was also able to determine that polyethylene glycol coated (AE014A) nanoparticles had a larger size (103 nm vs 47 nm) than uncoated nanoparticles using a similar synthesis (AE013B).

General Mössbauer Spectroscopy

After nanoparticle synthesis, Mössbauer spectroscopy was performed on each sample in order to help determine chemical composition and metallic iron content. Samples are grouped according to similar synthesis procedures as outlined in the Experimental Methods section.

The room-temperature ^{57}Fe Mössbauer spectra of AE001, AE002, and AE003 can be seen below in Figure 43. Each sample followed the same basic synthesis route (syringe pump $FeCl_3$ reduction with KBH_4 solution) with the following distinctive features: AE001 was synthesized in ambient atmosphere with a silica coating, AE002 was synthesized in a nitrogen atmosphere with a silica coating, and AE003 was produced with five times more initial reagents in a nitrogen flow with no silica coating. Hyperfine parameters can be seen in Table 14.

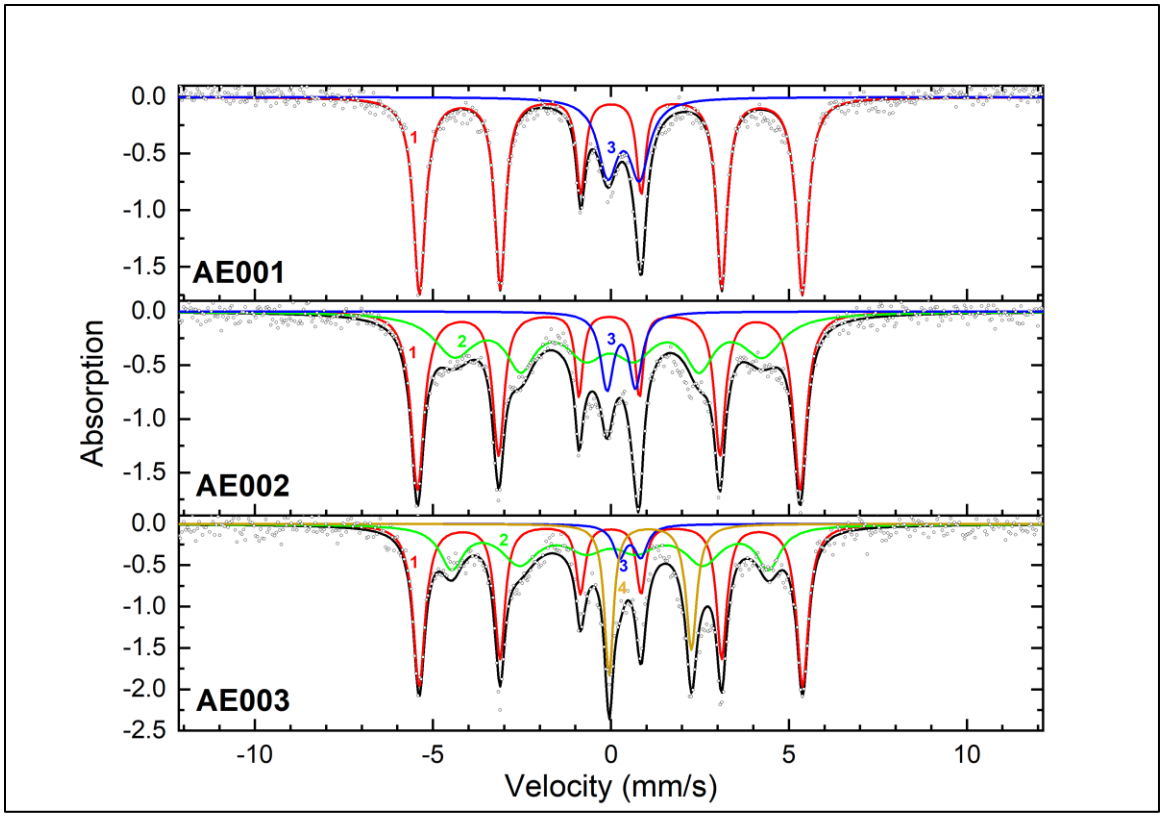


Figure 43. Stacked ^{57}Fe Mössbauer spectra of as-made AE001, AE002, and AE003 iron nanoparticles measured at 293 K. Each sample followed the same basic synthesis route (syringe pump $FeCl_3$ reduction with KBH_4 solution) with the following distinctive features: AE001 was synthesized in air with silica coating, AE002 was synthesized in a nitrogen flow with silica coating, and AE003 was synthesized as a 5x larger batch in a nitrogen flow with no silica coating.

Table 14. Values of hyperfine parameters derived from fitting as-made AE001, AE002, and AE003 metallic iron nanoparticles post-synthesis. B_{hf} is the hyperfine magnetic field, δ is the isomer shift, ΔE_Q is the quadrupole splitting, and Γ is the linewidth (FWHM). Typical errors are ±0.5 mm/s for B_{hf}, ±0.02 mm/s for δ, ΔE_Q, and Γ and ±3% for relative area

Sample	Component	B_{hf} (T)	δ (mm/s)	ΔE_Q (mm/s)	Γ (mm/s)	Relative area (%)	Attribution
AE001	1	33.3	0.00	0.00	0.41	78	α-Fe
	3	-	0.36	0.89	0.67	22	Fe^{3+} oxides
AE002	1	33.2	0.00	0.00	0.44	45	α-Fe
	2	26.7	0.00	-0.04	1.38	45	amorphous ZVI
	3	-	0.34	0.80	0.43	10	Fe^{3+} oxides
AE003	1	33.2	0.00	0.00	0.41	45	α-Fe
	2	27.4	0.00	-0.03	0.79	36	amorphous ZVI
	3	-	0.54	0.60	0.43	4	Fe^{3+} oxides
	4	-	1.10	2.31	0.36	15	Fe^{2+} impurities

The room-temperature Mössbauer spectra of AE001 show a superposition of two components, a narrow sextet (component 1, red line), and a split doublet (component 3, blue line). The narrow sextet (component 1) with magnetic hyperfine field 33.3 T, isomer shift 0.00 mm/s, and quadrupole splitting 0.0 mm/s is characteristic of crystalline α-Fe in the core [26, 33, 35, 50, 54]. The split doublet (component 3) with isomer shift 0.36 mm/s and quadrupole splitting 0.89 mm/s can be attributed to Fe^{3+} ions in oxide or hydroxide phases such as superparamagnetic γ-Fe_2O_3 or ferrihydrite [50, 53-57]. As this synthesis was conducted in an ambient atmosphere, these phases are most likely located at the shell of the nanoparticles, where the oxides are formed as the surface of the nanoparticle interacts with oxygen and moisture in both the atmospheric and synthesis environments. Mössbauer spectra of the as-made iron nanoparticle sample in Table 13 shows a 78% relative intensity for α-Fe (component 1) and a 22% relative intensity for ferric oxides/hydroxides (component 2).

The room-temperature Mössbauer spectra of AE002 (Figure 43) show a superposition of three components, a narrow sextet (component 1, red line), a broad sextet (component 2, green line), and a split doublet (component 3, blue line). The narrow sextet (component 1) with magnetic hyperfine field 33.2 T, isomer shift 0.00 mm/s, and quadrupole splitting 0.0 mm/s is characteristic of crystalline α-Fe in the core. New to AE002 is a broad sextet (component 2) with hyperfine field 26.7 T, isomer shift 0.00 mm/s, and quadrupole splitting -0.04 mm/s. These parameters correspond to amorphous zero-valent iron nanoparticles [26, 33, 35, 50, 53, 54, 58]. The split doublet (component 3) with isomer shift 0.34 mm/s and quadrupole splitting 0.80 mm/s can be attributed to Fe^{3+} ions in oxide or hydroxide phases such as superparamagnetic γ-Fe_2O_3 or ferrihydrite.

The broad sextet attributed to amorphous iron can be confirmed through inspection of the sub-spectrum (component 2) after low temperature and room temperature measurements. Figures A57-A60 and Tables A30-A33 in the Appendix show the stacked spectra and hyperfine parameters, respectively, of various nanoparticle samples (AE005, AE007 48-hr oxidized, AE008, AE011) measured at both 6K and 293K. At room temperature, the broad sextet can be attributed to either amorphous iron or relaxation effects from smaller scale metallic iron nanoparticles. At low temperatures (such as 6K), however, the broad sextet remains if contributed by amorphous iron or collapses if contributed by relaxation effects. Figures A57-A60 show broad sextets in the spectra for both 6K and 293K temperatures, confirming the presence of amorphous metallic iron within the nanoparticles [50, 53, 54, 58].

Unlike AE001's synthesis, which was conducted in air, AE002 was synthesized while under a nitrogen atmosphere in order to help mitigate oxidation during sample creation. Therefore, these oxide phases are most likely attributed to the nanoparticle's shell interacting with the ethanol and moisture in the reaction flask as opposed to oxygen in the atmosphere. Regardless, these oxides remain located on the surface of the nanoparticle, composing its shell and acting as a deterrent for further oxidation of the iron core.

The introduction of a nitrogen flow during sample synthesis demonstrated a marked decrease in sample oxidation. Table 14 shows a 45% spectral absorption for α-Fe (component 1), 45% spectral absorption for amorphous zero-valent iron nanoparticles (component 2), and a 10% for ferric oxides/hydroxides (component 3). When compared to AE001, this not only corresponds to a >50% decrease in oxide percentage, but also reveals the existence of amorphous zero-valent iron nanoparticles.

Finally, the room-temperature Mössbauer spectra of AE003 can be seen in Figure 43. AE003 is composed of three components, a narrow sextet (component 1, red line), a broad sextet (component 2, green line), and two split doublets (component 3, blue line), (component 4, yellow line). The narrow sextet (component 1) with magnetic hyperfine field 33.2 T, isomer shift 0.00 mm/s, and quadrupole splitting 0.0 mm/s is characteristic of crystalline α-Fe in the core. The broad sextet (component 2) with hyperfine field 27.4 T, isomer shift 0.00 mm/s, and quadrupole splitting -0.03 mm/s corresponds to amorphous zero-valent iron. The split doublet (component 3) with isomer shift 0.54 mm/s and quadrupole splitting 0.60 mm/s can be attributed to Fe^{3+} ions in oxide or hydroxide phases such as superparamagnetic γ-Fe_2O_3 or ferrihydrite. New to AE003, the split doublet with isomer shift 1.10 mm/s and quadrupole splitting 2.31 mm/s corresponds to partially reacted/oxidized iron oxide phases that occurred during sample synthesis [26, 59].

In order to have enough nanoparticle material for an oxidation time series encompassing six Mössbauer samples, AE003 was synthesized under nitrogen flow (like AE002), but with five times larger an amount of initial reagents. A synthesis this large resulted in a relatively significant amount (15%) of partially reacted iron impurities. This can be attributed to a lack of adequate mixing of reagents during synthesis due to the formation of a nanoparticle “island” (as seen in Figure 8c), or due to the complete consumption of the reducing agent before all of the iron (III) chloride could react as a limiting reagent.

Table 14 shows a 45% spectral absorption for α-Fe (component 1), 36% spectral absorption for amorphous zero-valent iron nanoparticles (component 2), a 4% spectral absorption for ferric oxides/hydroxides (component 3), and a 15% for Fe^{2+} impurities / partially reacted iron (component 4). AE003 was slightly more oxidized overall when compared to AE002, but still had significantly more amorphous zero-valent iron than AE001. The amount of partially reacted iron in

AE003 is the largest of any sample within this project and shows that smaller batches result in more consistent synthesis outcomes.

The room-temperature ^{57}Fe Mössbauer spectra of AE005, AE006, and AE011 can be seen below in Figure 44. Each sample followed the same basic synthesis route ($FeCl_3$ reduction with dropwise $NaBH_4$ solution followed by furnace drying) with the following distinctive features: AE005's dropwise synthesis lasted 35 minutes, AE006's dropwise synthesis lasted 15 minutes, and AE011's dropwise synthesis lasted 8 minutes. Hyperfine parameters can be seen in Table 15.

The room-temperature Mössbauer spectra of AE005 (Figure 44) show a superposition of three components, a narrow sextet (component 1, red line), a broad sextet (component 2, green line), and a split doublet (component 3, blue line). The narrow sextet (component 1) with magnetic hyperfine field 32.6 T, isomer shift 0.00 mm/s, and quadrupole splitting 0.00 mm/s is characteristic of crystalline α-Fe in the core. The broad sextet (component 2) with hyperfine field 25.5 T, isomer shift 0.00 mm/s, and quadrupole splitting 0.00 mm/s correspond to amorphous zero-valent iron. The split doublet (component 3) with isomer shift 0.38 mm/s and quadrupole splitting 0.86 mm/s can be attributed to Fe^{3+} ions in oxide or hydroxide phases such as superparamagnetic γ-Fe_2O_3 or ferrihydrite. Table 15 shows a 22.0% spectral absorption for α-Fe (component 1), 58% spectral absorption for amorphous zero-valent iron nanoparticles (component 2), and a 20% spectral absorption for ferric oxides/hydroxides (component 3).

The room-temperature Mössbauer spectra of AE006 (Figure 44) show a superposition of three components, a narrow sextet (component 1, red line), a broad sextet (component 2, green line), and a split doublet (component 3, blue line). The narrow sextet (component 1) with magnetic hyperfine field 32.8 T, isomer shift 0.00 mm/s, and quadrupole splitting -0.02 mm/s is characteristic of crystalline α-Fe in the core.

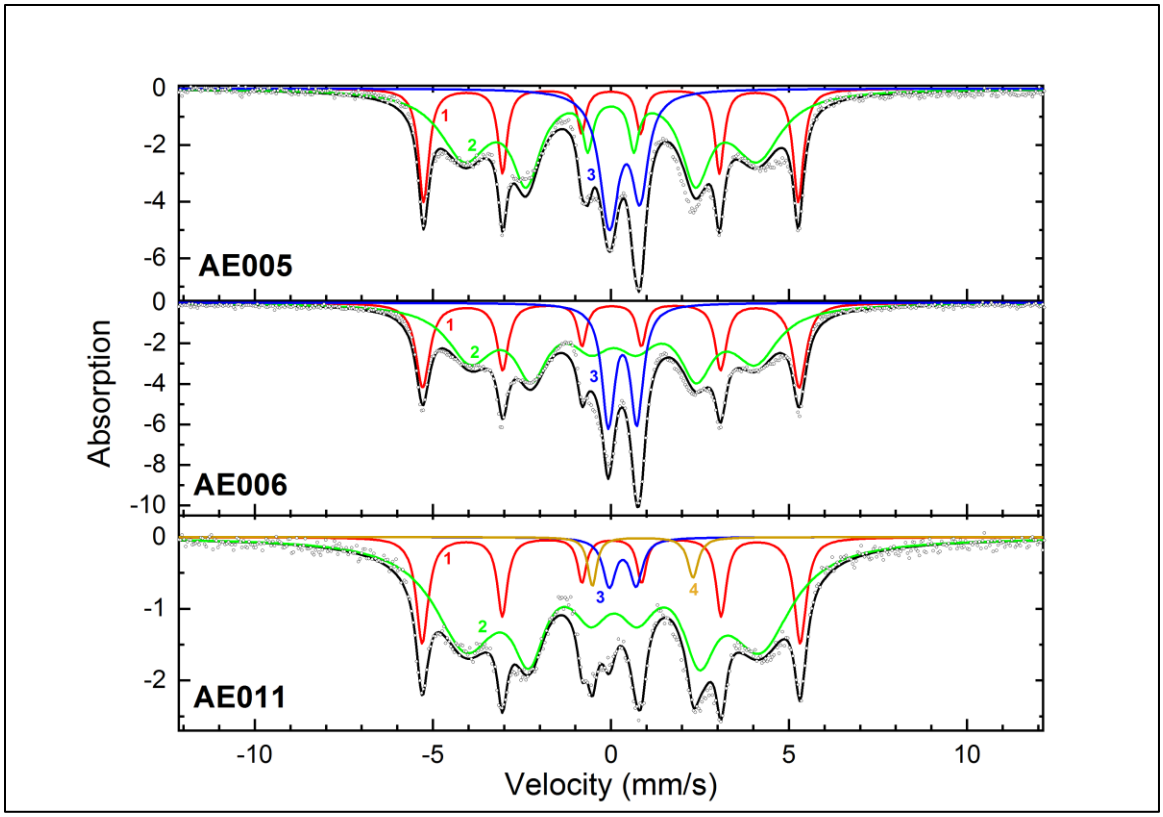


Figure 44. Stacked ^{57}Fe Mössbauer spectra of as-made AE005, AE006, and AE011 iron nanoparticles measured at 293K. Each sample followed the same basic synthesis route ($FeCl_3$ reduction in air with dropwise $NaBH_4$ solution, subsequent furnace drying) with the following distinctive features: AE005's dropwise synthesis lasted 35 min, AE006's dropwise synthesis lasted 15 min, and AE011's dropwise synthesis lasted 8 min. Not pictured: AE004

Table 15. Values of hyperfine parameters derived from fitting as-made AE005, AE006, and AE011 metallic iron nanoparticles post-synthesis. B_{hf} is the hyperfine magnetic field, δ is the isomer shift, ΔE_Q is the quadrupole splitting, and Γ is the linewidth (FWHM). Typical errors are ±0.5 mm/s for B_{hf}, ±0.02 mm/s for δ, ΔE_Q, and Γ and ±3% for relative area

Sample	Component	B_{hf} (T)	δ (mm/s)	ΔE_Q (mm/s)	Γ (mm/s)	Relative area (%)	Attribution
AE005	1	32.6	0.00	0.00	0.35	22	α-Fe
	2	25.5	0.00	0.00	1.68	58	amorphous ZVI
	3	-	0.38	0.86	0.54	20	Fe^{3+} oxides
AE006	1	32.8	0.00	-0.02	0.46	24	α-Fe
	2	24.8	0.06	-0.02	1.55	61	amorphous ZVI
	3	-	0.32	0.81	0.43	15	Fe^{3+} oxides
AE011	1	33.0	0.02	-0.02	0.41	16	α-Fe
	2	25.7	0.08	-0.03	2.20	77	amorphous ZVI
	3	-	0.34	0.76	0.43	4	Fe^{3+} oxides
	4	-	0.90	2.84	0.36	3	Fe^{2+} impurities

The broad sextet (component 2) with hyperfine field 24.8 T, isomer shift 0.06 mm/s, and quadrupole splitting -0.02 mm/s correspond to amorphous zero-valent iron nanoparticles. The split doublet (component 3) with isomer shift 0.32 mm/s and quadrupole splitting 0.81 mm/s can be attributed to Fe^{3+} ions in oxide or hydroxide phases such as superparamagnetic γ-Fe_2O_3 or ferrihydrite.

Table 15 shows a 24% relative intensity for α-Fe (component 1), 61% relative intensity for amorphous zero-valent iron nanoparticles (component 2), and a 15% relative intensity for ferric oxides/hydroxides (component 3).

Lastly, the room-temperature Mössbauer spectra of AE011 can be seen in Figure 44. AE011 is composed of three components, a narrow sextet (component 1, red line), a broad sextet (component 2, green line), and two split doublets (component 3, blue line), (component 4, yellow line). The narrow sextet (component 1) with magnetic hyperfine field 33.0 T, isomer shift 0.02 mm/s, and quadrupole splitting -0.02 mm/s is characteristic of crystalline α-Fe in the core. The broad sextet (component 2) with hyperfine field 25.7 T, isomer shift 0.08 mm/s, and quadrupole splitting -0.03 mm/s correspond to amorphous zero-valent iron nanoparticles. The split doublet (component 3) with isomer shift 0.34 mm/s and quadrupole splitting 0.76 mm/s can be attributed to Fe^{3+} ions in oxide or hydroxide phases such as superparamagnetic γ-Fe_2O_3 or ferrihydrite. A component new to AE011, the split doublet with isomer shift 0.90 mm/s and quadrupole splitting 2.84 mm/s corresponds to partially reacted/oxidized iron oxide phases that occurred during sample synthesis.

Table 15 shows a 16% spectral absorption for α-Fe (component 1), 77% spectral absorption for amorphous zero-valent iron nanoparticles (component 2), a 4% spectral absorption for ferric oxides/hydroxides (component 3), and a 3% for Fe^{2+} impurities / partially reacted iron (component 4).

The speed of the reducing agent ($NaBH_4$) dropping into the reaction flask influenced the final zero-valent iron percentage. Generally, as drop speed increased, ZVI NP percentage increased. AE005 (35-minute synthesis) and AE006 (15-minute synthesis) were similar in overall composition breakdown, but a significant increase in ZVI percentage occurred (16%) between AE006 and AE011 (8-minute synthesis). This increase in zero-valent iron caused a decrease in both α-Fe and Fe^{3+} oxide/hydroxide percentage. The speed of the reaction, however, may have been too fast, as AE011 is the only sample where Fe^{2+} impurities are detected.

The room-temperature ^{57}Fe Mössbauer spectra of AE007 and AE008 can be seen below in Figure 45. Each sample followed the same basic synthesis route ($FeCl_3$ reduction in argon with dropwise $NaBH_4$ solution, vacuum filtration, and subsequent furnace drying). Hyperfine parameters can be seen in Table 16.

The room-temperature Mössbauer spectra of AE007 show a superposition of two components, a narrow sextet (component 1, red line), and a broad sextet (component 2, green line). The narrow sextet (component 1) with magnetic hyperfine field 32.8 T, isomer shift 0.00 mm/s, and quadrupole splitting 0.00 mm/s is characteristic of crystalline α-Fe in the core. The broad sextet (component 2) with magnetic hyperfine field 24.2 T, isomer shift 0.09 mm/s and quadrupole splitting -0.03 mm/s can be attributed to amorphous zero-valent iron nanoparticles. Mössbauer spectra of the as-made iron nanoparticle sample in Table 16 shows a 14% relative intensity for α-Fe (component 1) and an 86% relative intensity for amorphous zero-valent iron nanoparticles (component 2).

The room-temperature Mössbauer spectra of AE008 show a superposition of two components, a narrow sextet (component 1, red line), and a broad sextet (component 2, green line).

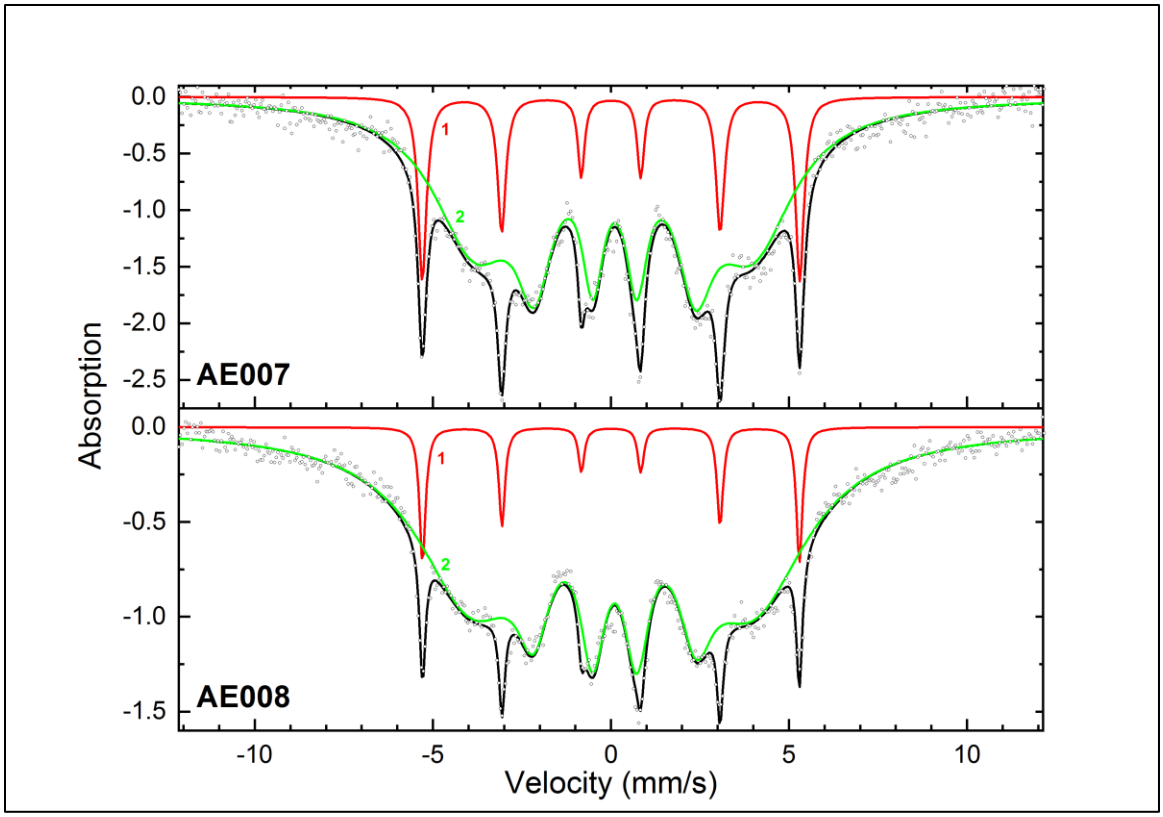


Figure 45. Stacked ^{57}Fe Mössbauer spectra of as-made AE007 and AE008 iron nanoparticles measured at 293K. Each sample followed the same basic synthesis route: $FeCl_3$ reduction in argon with dropwise $NaBH_4$ solution, vacuum filtration, and subsequent furnace drying

Table 16. Values of hyperfine parameters derived from fitting as-made AE007 and AE008 metallic iron nanoparticles post-synthesis. B_{hf} is the hyperfine magnetic field, δ is the isomer shift, ΔE_Q is the quadrupole splitting, and Γ is the linewidth (FWHM). Typical errors are ±0.03 mm/s for B_{hf}, ±0.5 mm/s for δ, ΔE_Q, and Γ and ±3% for relative area

Sample	Component	B_{hf} (T)	δ (mm/s)	ΔE_Q (mm/s)	Γ (mm/s)	Relative area (%)	Attribution
AE007	1	32.8	0.00	0.00	0.28	14	α-Fe
	2	24.2	0.09	-0.03	2.84	86	amorphous ZVI
AE008	1	32.8	0.00	0.00	0.21	6	α-Fe
	2	24.4	0.07	-0.06	3.75	94	amorphous ZVI

The narrow sextet (component 1) with magnetic hyperfine field 32.8 T, isomer shift 0.00 mm/s, and quadrupole splitting 0.00 mm/s is characteristic of crystalline α-Fe in the core. The broad sextet (component 2) with magnetic hyperfine field 24.4 T, isomer shift 0.07 mm/s and quadrupole splitting -0.06 mm/s can be attributed to amorphous zero-valent iron nanoparticles. Mössbauer spectra of the as-made iron nanoparticle sample in Table 16 shows a 6% relative intensity for α-Fe (component 1) and a 94% relative intensity for amorphous zero-valent iron nanoparticles (component 2).

AE007 and AE008 have the largest amount of amorphous zero-valent iron out of all synthesized samples and illustrate the importance of using an inert gas flow during synthesis to minimize oxidation. The result, however, has proven difficult to repeat, as most samples, including ones using the exact same reaction parameters, usually have at least some percentage of Fe^{3+} oxide/hydroxide shell present in their Mössbauer spectra.

The room-temperature ^{57}Fe Mössbauer spectra of AE009 and AE010 can be seen below in Figure 46. Each sample followed the same basic synthesis route ($FeCl_3$ reduction in argon with dropwise $NaBH_4$ solution, vacuum filtration, and subsequent furnace drying). Hyperfine parameters can be seen in Table 17.

The room-temperature Mössbauer spectra of AE009 (Figure 46) show a superposition of three components, a narrow sextet (component 1, red line), a broad sextet (component 2, green line), and a split doublet (component 3, blue line). The narrow sextet (component 1) with magnetic hyperfine field 32.8 T, isomer shift 0.00 mm/s, and quadrupole splitting -0.01 mm/s is characteristic of crystalline α-Fe in the core. The broad sextet (component 2) with hyperfine field 25.9 T, isomer shift 0.07 mm/s, and quadrupole splitting -0.05 mm/s corresponds to amorphous zero-valent iron nanoparticles.

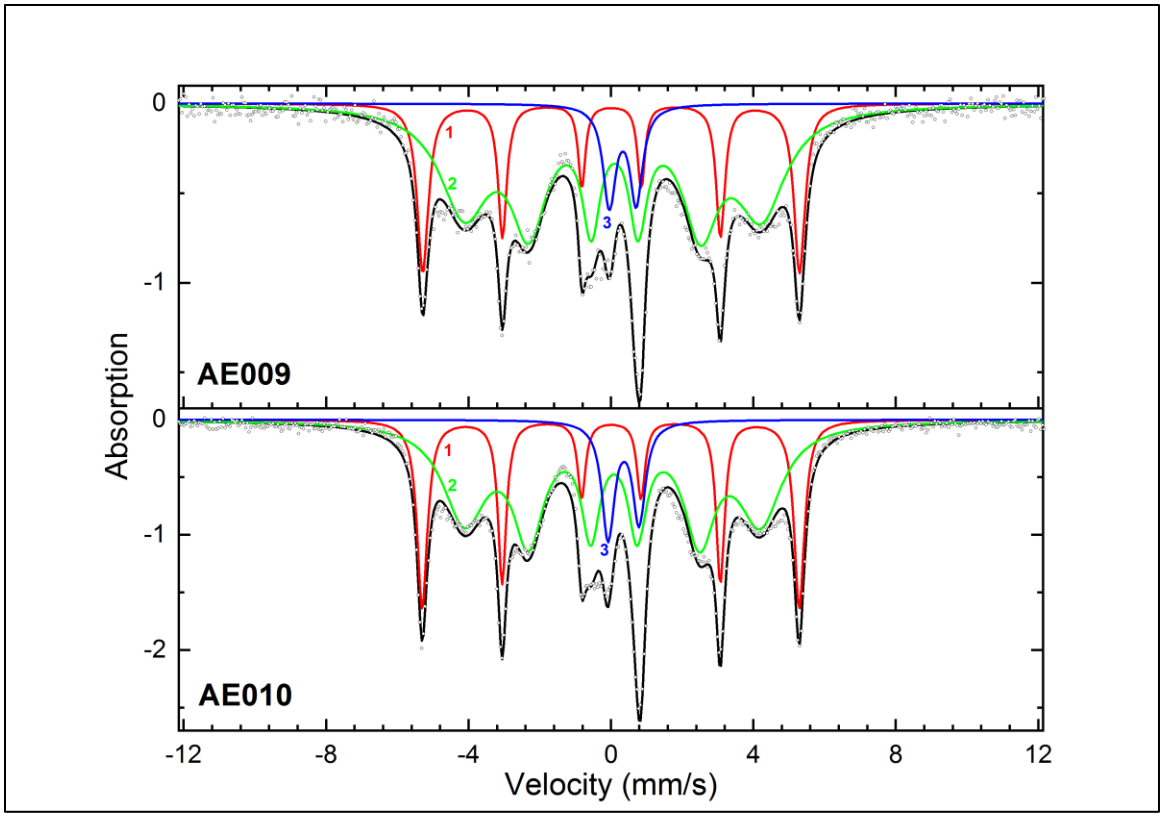


Figure 46**. Stacked ^{57}Fe Mössbauer spectra of as-made AE009 and AE010 iron nanoparticles measured at 293K. Each sample followed the same basic synthesis route: $FeCl_3$ reduction in argon with dropwise $NaBH_4$ solution, vacuum filtration, and subsequent furnace drying**

Table 17. Values of hyperfine parameters derived from fitting as-made AE009 and AE010 metallic iron nanoparticles post-synthesis. B_{hf} is the hyperfine magnetic field, δ is the isomer shift, ΔE_Q is the quadrupole splitting, and Γ is the linewidth (FWHM). Typical errors are ±0.03 mm/s for B_{hf}, ±0.5 mm/s for δ, ΔE_Q, and Γ and ±3% for relative area

Sample	Component	B_{hf} (T)	δ (mm/s)	ΔE_Q (mm/s)	Γ (mm/s)	Relative area (%)	Attribution
AE009	1	32.8	0.00	-0.01	0.38	23	α-Fe
	2	25.9	0.07	-0.05	1.67	69	amorphous ZVI
	3	-	0.33	0.76	0.43	8	Fe^{3+} oxides
AE010	1	32.9	0.00	-0.01	0.35	27	α-Fe
	2	25.8	0.07	-0.04	1.48	64	amorphous ZVI
	3	-	0.36	0.88	0.43	9	Fe^{3+} oxides

The split doublet (component 3) with isomer shift 0.33 mm/s and quadrupole splitting 0.76 mm/s can be attributed to Fe^{3+} ions in oxide or hydroxide phases such as superparamagnetic γ-Fe_2O_3 or ferrihydrite.

Table 17 shows a 23% relative intensity for α-Fe (component 1), 69% relative intensity for amorphous zero-valent iron nanoparticles (component 2), and an 8% relative intensity for ferric oxide/hydroxide (component 3).

The room-temperature Mössbauer spectra of AE010 (Figure 46) show a superposition of three components, a narrow sextet (component 1, red line), a broad sextet (component 2, green line), and a split doublet (component 3, blue line). The narrow sextet (component 1) with magnetic hyperfine field 32.9 T, isomer shift 0.00 mm/s, and quadrupole splitting -0.01 mm/s is characteristic of crystalline α-Fe in the core. The broad sextet (component 2) with hyperfine field 25.8 T, isomer shift 0.07 mm/s, and quadrupole splitting -0.04 mm/s corresponds to amorphous zero-valent iron nanoparticles. The split doublet (component 3) with isomer shift 0.36 mm/s and quadrupole splitting 0.88 mm/s can be attributed to Fe^{3+} ions in oxide or hydroxide phases such as superparamagnetic γ-Fe_2O_3 or ferrihydrite.

Table 17 shows a 27% relative intensity for α-Fe (component 1), 64% relative intensity for amorphous zero-valent iron nanoparticles (component 2), and a 9% relative intensity for ferric oxides/hydroxides (component 3).

AE009 and AE010 show the repeatability of the $NaBH_4$ dropwise synthesis with argon gas flow; as final chemical compositions were similar between syntheses. When combined with the results of AE007 and AE008, all samples produced a product with a majority amorphous zero-valent iron and <10% surface oxidation.

The room-temperature ^{57}Fe Mössbauer spectra of AE013A and AE014A can be seen below in Figure 47. Each sample followed the same basic synthesis route (syringe pump $FeCl_3$ reduction with $NaBH_4$ solution, PEG coating, followed by vacuum filtration and glovebox furnace drying) with the only difference being AE014A's synthesis being a double batch. Hyperfine parameters can be seen in Table 18.

The room-temperature Mössbauer spectra of AE013A can be seen below in Figure 47. AE013A is composed of four components, a narrow sextet (component 1, red line), a broad sextet (component 2, green line), and two split doublets (component 3, blue line), (component 4, yellow line). The narrow sextet (component 1) with magnetic hyperfine field 33.6 T, isomer shift 0.01 mm/s, and quadrupole splitting -0.01 mm/s is characteristic of crystalline α-Fe in the core. The broad sextet (component 2) with hyperfine field 26.6 T, isomer shift 0.09 mm/s, and quadrupole splitting -0.04 mm/s corresponds to amorphous zero-valent iron nanoparticles. The split doublet (component 3) with isomer shift 0.35 mm/s and quadrupole splitting 0.85 mm/s can be attributed to Fe^{3+} ions in oxide or hydroxide phases such as superparamagnetic γ-Fe_2O_3 or ferrihydrite. The split doublet with isomer shift 0.79 mm/s and quadrupole splitting 2.65 mm/s corresponds to partially reacted/oxidized iron oxide phases that occurred during sample synthesis.

Table 18 shows a 23% spectral absorption for α-Fe (component 1), 65% spectral absorption for amorphous zero-valent iron nanoparticles (component 2), a 10% spectral absorption for ferric oxides/hydroxides (component 3), and a 2% for Fe^{2+} impurities / partially reacted iron (component 4).

The room-temperature Mössbauer spectra of AE014A can be seen in Figure 47. AE014A is composed of four components, a narrow sextet (component 1, red line), a broad sextet (component 2, green line),

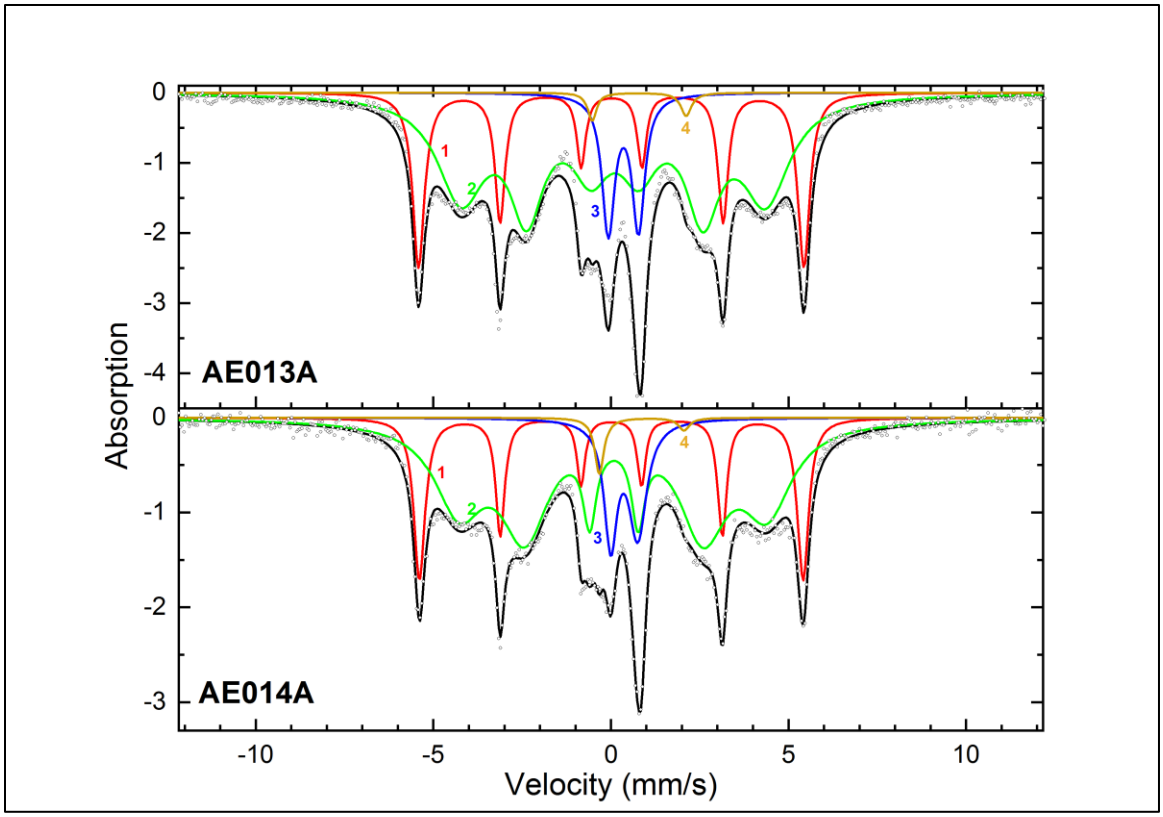


Figure 47**. Stacked ^{57}Fe Mössbauer spectra of as-made PEG-coated AE013A and AE014A iron nanoparticles measured at 293K. Each sample followed the same basic synthesis route: syringe pump $FeCl_3$ reduction with $NaBH_4$ solution followed by vacuum filtration and glovebox furnace drying.**

Table 18. Values of hyperfine parameters derived from fitting as-made AE013A and AE014A metallic iron nanoparticles post-synthesis. B_{hf} is the hyperfine magnetic field, δ is the isomer shift, ΔE_Q is the quadrupole splitting, and Γ is the linewidth (FWHM). Typical errors are ±0.5 mm/s for B_{hf}, ±0.02 mm/s for δ, ΔE_Q, and Γ and ±3% for relative area

Sample	Component	B_{hf} (T)	δ (mm/s)	ΔE_Q (mm/s)	Γ (mm/s)	Relative area (%)	Attribution
AE013A	1	33.6	0.01	-0.01	0.40	23	α-Fe
	2	26.6	0.09	-0.04	1.62	65	amorphous ZVI
	3	-	0.35	0.85	0.43	10	Fe^{3+} oxides
	4	-	0.79	2.65	0.36	2	Fe^{2+} impurities
AE014A	1	33.3	0.00	0.00	0.38	22	α-Fe
	2	26.7	0.06	-0.02	1.67	65	amorphous ZVI
	3	-	0.36	0.76	0.61	11	Fe^{3+} oxides
	4	-	0.85	2.37	0.37	2	Fe^{2+} impurities

and two split doublets (component 3, blue line), (component 4, yellow line). The narrow sextet (component 1) with magnetic hyperfine field 33.3 T, isomer shift 0.00 mm/s, and quadrupole splitting 0.00 mm/s is characteristic of crystalline α-Fe in the core. The broad sextet (component 2) with hyperfine field 26.7 T, isomer shift 0.06 mm/s, and quadrupole splitting -0.02 mm/s corresponds to amorphous zero-valent iron nanoparticles. The split doublet (component 3) with isomer shift 0.36 mm/s and quadrupole splitting 0.76 mm/s can be attributed to Fe^{3+} ions in oxide or hydroxide phases such as superparamagnetic γ-Fe_2O_3 or ferrihydrite.

The split doublet with isomer shift 0.85 mm/s and quadrupole splitting 2.37 mm/s corresponds to partially reacted/oxidized iron oxide phases that occurred during sample synthesis.

Table 18 shows a 22% spectral absorption for α-Fe (component 1), 65% spectral absorption for amorphous zero-valent iron nanoparticles (component 2), a 11% spectral absorption for ferric oxides/hydroxides (component 3), and a 2% for Fe^{2+} impurities / partially reacted iron (component 4).

The room-temperature ^{57}Fe Mössbauer spectra of AE013B and AE014B can be seen below in Figure 48. Each sample followed the same basic synthesis route (syringe pump $FeCl_3$ reduction with $NaBH_4$ solution, uncoated, followed by vacuum filtration and glovebox furnace drying) with the only difference being AE014B's synthesis being a double batch. Hyperfine parameters can be seen in Table 19.

The room-temperature Mössbauer spectra of AE013B can be seen above in Figure 48. AE013B is composed of four components, a narrow sextet (component 1, red line), a broad sextet (component 2, green line), and two split doublets (component 3, blue line), (component 4, yellow line).

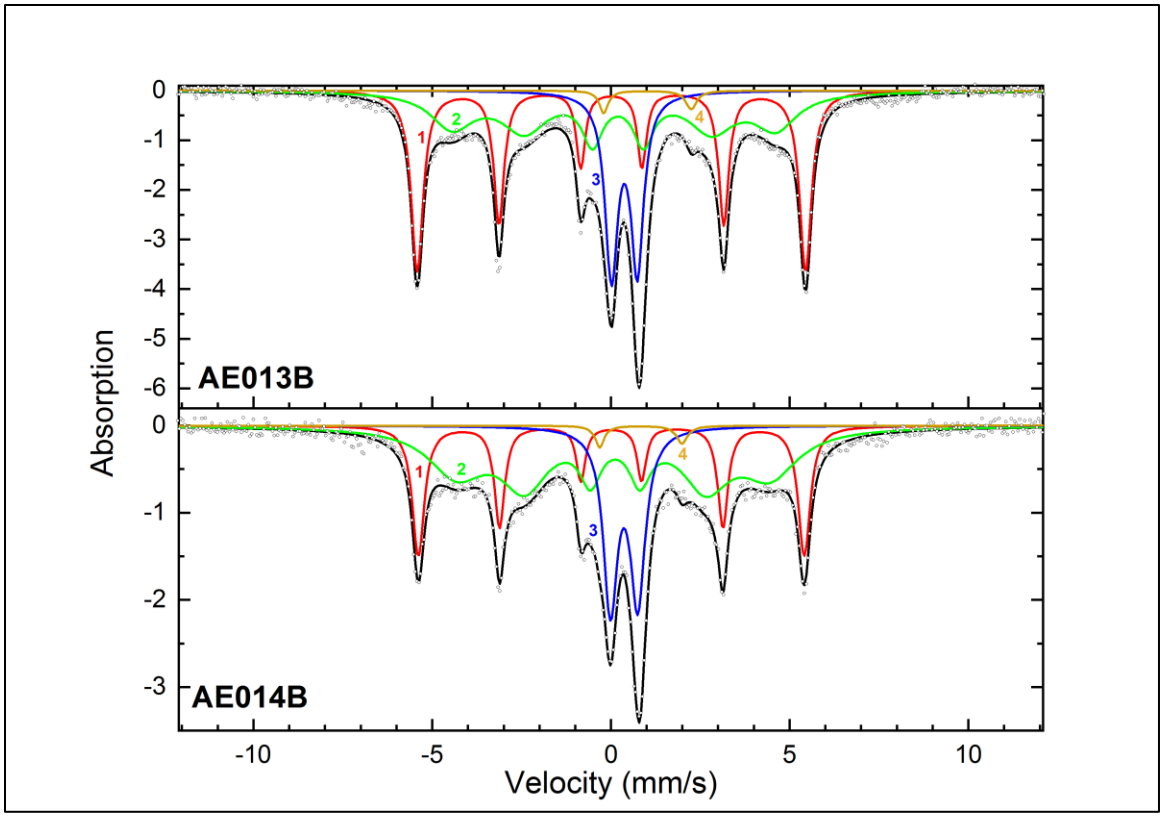


Figure 48. Stacked ^{57}Fe Mössbauer spectra of as-made AE013B and AE014B iron nanoparticles measured at 293K. Each sample followed the same basic synthesis route: syringe pump $FeCl_3$ reduction with $NaBH_4$ solution followed by vacuum filtration and glovebox furnace drying.

Table 19. Values of hyperfine parameters derived from fitting as-made AE013B and AE014B metallic iron nanoparticles post-synthesis. B_{hf} is the hyperfine magnetic field, δ is the isomer shift, ΔE_Q is the quadrupole splitting, and Γ is the linewidth (FWHM). Typical errors are ±0.03 mm/s for B_{hf}, ±0.5 mm/s for δ, ΔE_Q, and Γ and ±3% for relative area

Sample	Component	B_{hf} (T)	δ (mm/s)	ΔE_Q (mm/s)	Γ (mm/s)	Relative area (%)	Attribution
AE013B	1	33.6	0.01	0.00	0.41	38	α-Fe
	2	28.1	0.14	-0.11	1.44	39	amorphous ZVI
	3	-	0.38	0.73	0.43	21	Fe^{3+} oxides
	4	-	1.02	2.45	0.36	2	Fe^{2+} impurities
AE014B	1	33.2	0.00	0.00	0.41	25	α-Fe
	2	26.9	0.08	-0.05	1.89	52	amorphous ZVI
	3	-	0.35	0.76	0.50	21	Fe^{3+} oxides
	4	-	0.82	2.29	0.37	2	Fe^{2+} impurities

The narrow sextet (component 1) with magnetic hyperfine field 33.6 T, isomer shift 0.01 mm/s, and quadrupole splitting 0.00 mm/s is characteristic of crystalline α-Fe in the core. The broad sextet (component 2) with hyperfine field 28.1 T, isomer shift 0.14 mm/s, and quadrupole splitting -0.11 mm/s corresponds to amorphous zero-valent iron nanoparticles. The split doublet (component 3) with isomer shift 0.38 mm/s and quadrupole splitting 0.73 mm/s can be attributed to Fe^{3+} ions in oxide or hydroxide phases such as superparamagnetic γ-Fe_2O_3 or ferrihydrite. Finally, the split doublet with isomer shift 1.02 mm/s and quadrupole splitting 2.45 mm/s corresponds to partially reacted/oxidized iron oxide phases that occurred during sample synthesis.

Table 19 shows a 38% spectral absorption for α-Fe (component 1), 39% spectral absorption for amorphous zero-valent iron nanoparticles (component 2), a 21% spectral absorption for ferric oxides/hydroxides (component 3), and a 2% for Fe^{2+} impurities / partially reacted iron (component 4).

The room-temperature Mössbauer spectra of AE014B can be seen above in Figure 48. AE014B is composed of four components, a narrow sextet (component 1, red line), a broad sextet (component 2, green line), and two split doublets (component 3, blue line), (component 4, yellow line). The narrow sextet (component 1) with magnetic hyperfine field 33.2 T, isomer shift 0.00 mm/s, and quadrupole splitting 0.00 mm/s is characteristic of crystalline α-Fe in the core. The broad sextet (component 2) with hyperfine field 26.9 T, isomer shift 0.08 mm/s, and quadrupole splitting -0.05 mm/s corresponds to amorphous zero-valent iron nanoparticles. The split doublet (component 3) with isomer shift 0.35 mm/s and quadrupole splitting 0.76 mm/s can be attributed to Fe^{3+} ions in oxide or hydroxide phases such as superparamagnetic γ-Fe_2O_3 or ferrihydrite. Finally, the split doublet with isomer shift 0.82 mm/s and quadrupole splitting 2.29 mm/s corresponds to partially reacted/oxidized iron oxide phases that occurred during sample synthesis.

Table 19 shows a 25% spectral absorption for α-Fe (component 1), 52% spectral absorption for amorphous zero-valent iron nanoparticles (component 2), a 21% spectral absorption for ferric oxides/hydroxides (component 3), and a 2% for Fe^{2+} impurities / partially reacted iron (component 4).

While results were consistent amongst AE013 and AE014 PEG-coated (A) and uncoated (B) sample groups, a comparison between A and B sample groupings illustrates the efficacy of nanoparticle coating in reducing Fe^{3+} oxidation in the final synthesis product. PEG-coated samples possessed a 20% greater amount of amorphous zero-valent iron when compared to their uncoated counterparts as well as 10% less Fe^{3+} oxides detected.

Overall, this Mössbauer study of as-made iron nanoparticles demonstrates the effect synthesis parameters have on the final composition of the synthesized nanoparticles. Inert gas flow (either nitrogen or argon) was shown to reduce oxidation and increase amorphous ZVI content in the resultant iron nanoparticles. The same trend was shown with PEG coating immediately after synthesis. Amorphous ZVI content was shown to increase as dropwise reaction time decreased, although large synthesis size and shorter reaction times introduced partially oxidized and reacted products.

Mössbauer Spectroscopy Oxidation Time Studies

AE001: Syringe Pump $FeCl_3$ Reduction in Air

The room temperature ^{57}Fe Mössbauer spectra of AE001 iron nanoparticles at three separate time intervals during an ambient oxidation experiment are shown in Figure 49. Measurements were collected immediately post synthesis, after 72 hours of aging, and after 2 weeks of aging. Hyperfine parameters can be seen in Table 20.

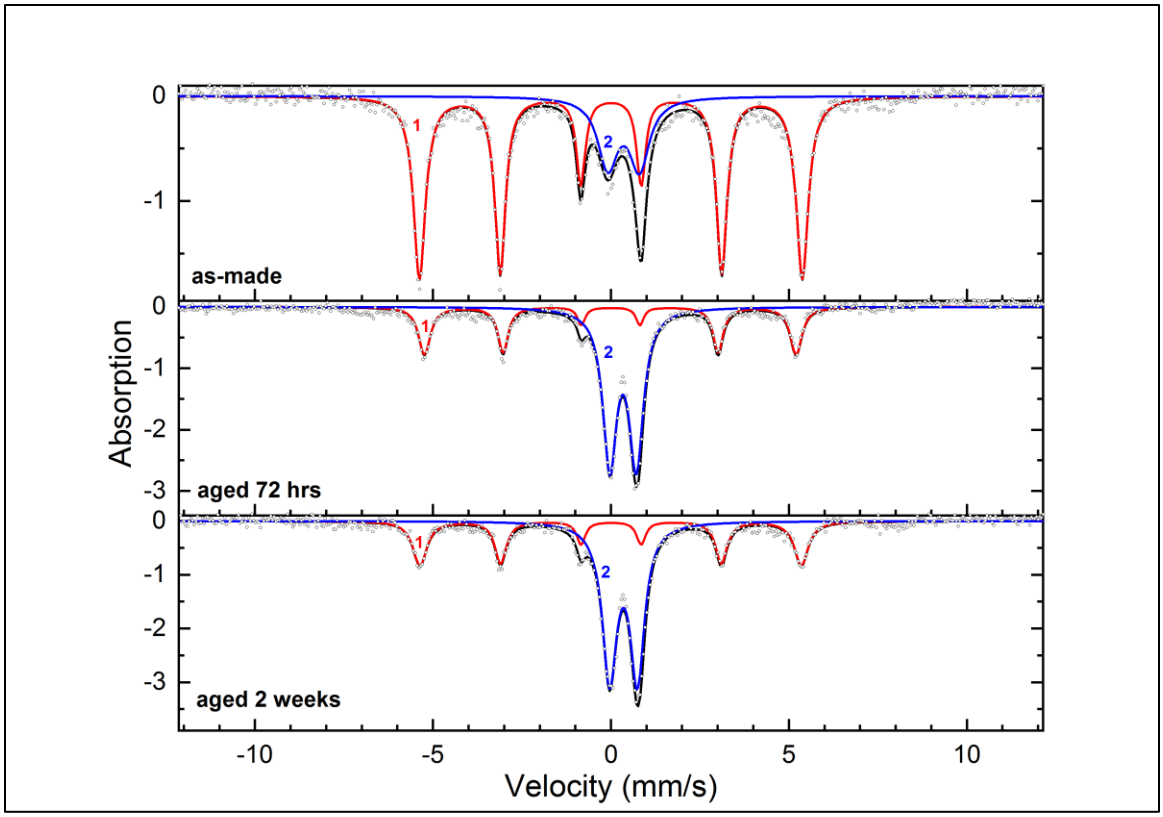


Figure 49**. Stacked ^{57}Fe Mössbauer spectra of AE001 iron nanoparticles three separate time intervals (as-made, 72 hrs, 2 weeks) throughout an oxidation process in air, measured at 293 K**

Table 20. Values of hyperfine parameters derived from fitting AE001 metallic iron nanoparticles prepared at lengths of room temperature ambient oxidation. B_{hf} is the hyperfine magnetic field, δ is the isomer shift, ΔE_Q is the quadrupole splitting, and Γ is the linewidth (FWHM). Typical errors are ±0.03 mm/s for B_{hf}, ±0.5 mm/s for δ, ΔE_Q, and Γ and ±3% for relative area

Sample	Component	B_{hf} (T)	δ (mm/s)	ΔE_Q (mm/s)	Γ (mm/s)	Relative area (%)	Attribution
as-made	1	33.3	0.00	0.00	0.41	78	α-Fe
	2	-	0.36	0.89	0.67	22	Fe^{3+} oxides
aged 72 hours	1	32.9	-0.01	-0.01	0.40	35	α-Fe
	2	-	0.34	0.75	0.48	65	Fe^{3+} oxides
aged 2 weeks	1	33.2	0.00	-0.01	0.47	35	α-Fe
	2	-	0.35	0.78	0.48	65	Fe^{3+} oxides

The spectra of all three time-interval samples are composed of two components, a narrow sextet (component 1) and a split doublet (component 2). The narrow sextet with magnetic hyperfine field 33.0 T, isomer shift 0.00 mm/s, and quadrupole splitting 0.0 mm/s is characteristic of crystalline α-Fe in the core [26, 33, 35, 50, 54]. The split doublet with isomer shift ~0.35 mm/s and quadrupole splitting ~0.80 mm/s can be attributed to Fe^{3+} oxides such as superparamagnetic γ-Fe_2O_3 or ferrihydrite [50, 53-57].

The relative percentage of each iron species changed as the sample oxidized. Mössbauer spectra of the as-made iron nanoparticle sample in Figure 49 showed a 78% relative intensity for α-Fe (component 1) and a 22% relative intensity for Fe^{3+} oxides (component 2). Initial oxidation of the as-made sample can be attributed to its storage in ethanol, encouraging passivation of the iron nanoparticle's highly reactive surface, before measurement. After 72 hours of aging, the α-Fe intensity decreased to 35% and Fe^{3+} oxide intensity increased to 65%. After 2 weeks of aging, α-Fe intensity and Fe^{3+} oxide intensity held steady at approximately 35% and 65%, respectively. Mössbauer results show the sample experienced the entirety of its oxidation during the initial 72 hours following synthesis. This oxide layer shielded the crystalline iron nanoparticles' core from further oxidation over the subsequent 2 weeks.

AE007: Dropwise $FeCl_3$ Reduction in Argon Flow

Since AE001 experienced the entirety of its oxidation in the first three days post synthesis, another ambient oxidation experiment was conducted on a briefer time scale. Metallic iron nanoparticles were synthesized, separated into batches, and left to oxidize in air at room temperature. Mössbauer measurements were collected immediately post synthesis, after 2 hours aging, and after 48 hours aging. The room temperature ^{57}Fe Mössbauer spectra of AE007 iron

nanoparticles at these three separate time intervals are shown in Figure 50. Hyperfine parameters can be seen in Table 21.

The spectra of the as-made sample are composed of two components, whereas the 2-hour and 48-hour aged samples are composed of three components. The narrow sextet (component 1) is characteristic of crystalline α-Fe in the nanoparticles' core and has magnetic hyperfine field ~33.0 T, isomer shift 0.00 mm/s, and quadrupole splitting 0.00 mm/s. The broad sextet (component 2) with magnetic hyperfine field ~24.0 T and isomer shift ~0.07 mm/s can be attributed to amorphous zero-valent iron nanoparticles [26, 33, 35, 50, 53, 54, 58]. The split doublet (component 3) has isomer shift 0.32 mm/s and quadrupole splitting ~0.81 mm/s and is indicative of superparamagnetic Fe^{3+} oxides/hydroxides like in the previous oxidation test.

The relative percentage of each iron species changed as the sample oxidized. Mössbauer spectra of the as-made iron nanoparticle sample in Figure 50 showed a 14% relative intensity for α-Fe (component 1) and an 86% relative intensity for amorphous ZVI nanoparticles (component 2). After 2 hours of aging, α-Fe intensity increased to 18%, ZVI iron intensity decreased to 75%, and Fe^{3+} oxide (component 3) intensity increased to 7%. The increase in surface oxide content comes at the expense of ZVI intensity. After 48 hours of aging, α-Fe intensity decreased to 15%, amorphous iron decreased to 73%, and Fe^{3+} oxide intensity increased to 12%. Mössbauer results show the sample experienced most of its oxidation during the first 2 hours post synthesis.

AE003: Syringe Pump $FeCl_3$ Reduction in Nitrogen Flow

Because AE007's particles experienced most of their oxidation in the first 2 hours post synthesis, another ambient oxidation experiment was conducted on a similar scale.

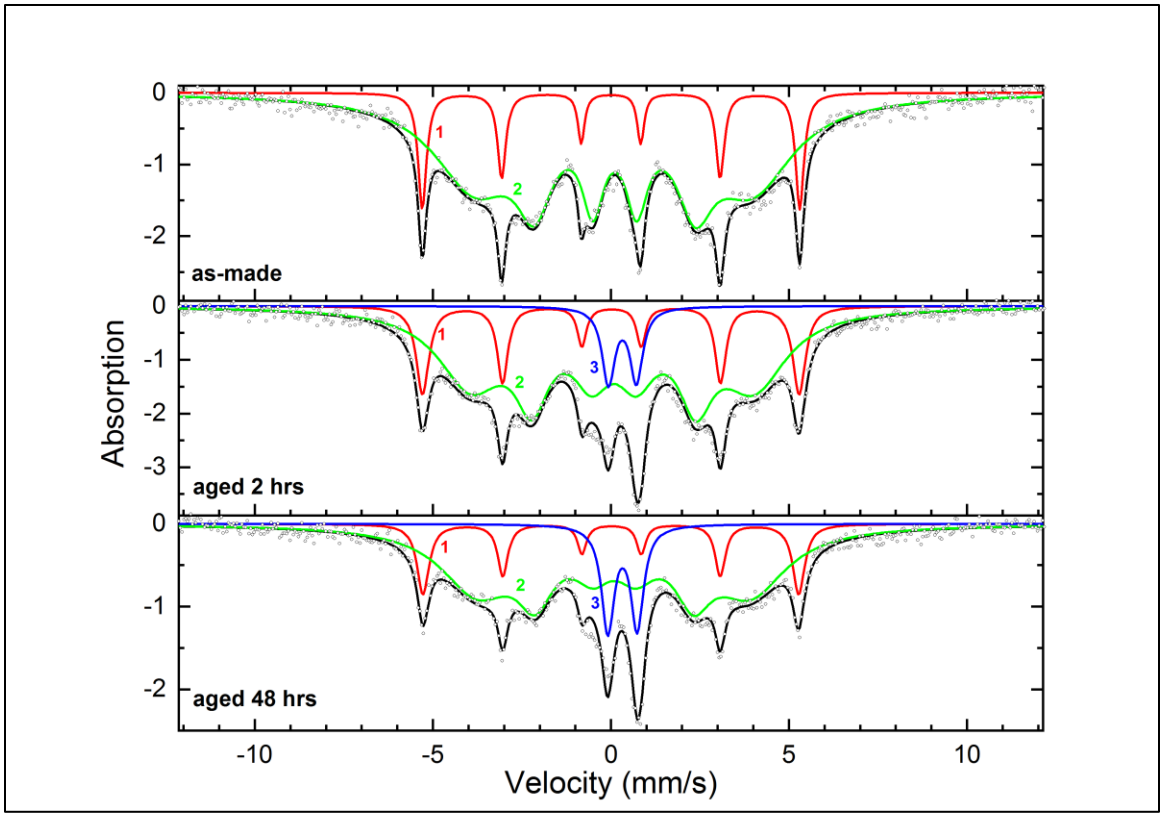


Figure 50. Stacked ^{57}Fe Mössbauer spectra of AE007 FeNPs at three time intervals (as-made, 2-hrs, 48-hrs) throughout an oxidation process in air, measured at 293 K

Table 21. Values of hyperfine parameters derived from fitting AE007 metallic iron nanoparticles prepared at lengths of room temperature ambient oxidation. B_{hf} is the hyperfine magnetic field, δ is the isomer shift, ΔE_Q is the quadrupole splitting, and Γ is the linewidth (FWHM). Typical errors are ±0.5 mm/s for B_{hf}, ±0.02 mm/s for δ, ΔE_Q, and Γ and ±3% for relative area

Sample	Component	B_{hf} (T)	δ (mm/s)	ΔE_Q (mm/s)	Γ (mm/s)	Relative area (%)	Attribution
as-made	1	32.8	0.00	0.00	0.28	14	α-Fe
	2	24.2	0.09	-0.03	2.84	86	amorphous ZVI
2 hours	1	32.8	0.00	-0.02	0.43	18	α-Fe
	2	24.7	0.06	-0.04	2.24	75	amorphous ZVI
	3	-	0.32	0.79	0.43	7	Fe^{3+} oxides
48 hours	1	32.7	0.00	-0.02	0.41	15	α-Fe
	2	23.8	0.09	-0.01	2.52	73	amorphous ZVI
	3	-	0.32	0.83	0.43	12	Fe^{3+} oxides

Metallic iron nanoparticles were synthesized, separated into samples, and left to oxidize in air at room temperature for the appropriate period. Mössbauer measurements were collected immediately post synthesis and after 1, 2, 4, and 5 hours of aging. A 3 hours aged sample measurement was lost due to experimental error. The room temperature ^{57}Fe Mössbauer spectra of these iron nanoparticles at five separate time intervals are shown in Figure 51. Hyperfine parameters can be seen in Table 22.

The spectra of all samples are composed of four spectral components. The narrow sextet (component 1) is characteristic of crystalline α-Fe in the nanoparticle's core and has magnetic hyperfine field ~33.2 T, isomer shift 0.00 mm/s, and quadrupole splitting 0.00 mm/s. The broad sextet (component 2) with magnetic hyperfine field ~27.0 T is attributed to amorphous zero-valent iron. The split doublet (component 3) with isomer shifts ranging from 0.25-0.55 mm/s and quadrupole splitting ~0.60 mm/s is indicative of superparamagnetic Fe^{3+} oxides. Another split doublet (component 4) with isomer shift 1.10 mm/s and quadrupole splitting ~2.27 mm/s corresponds to partially oxidized iron ions caused by impurities during synthesis [26].

The relative percentage of each iron species changed as the sample oxidized. Mössbauer spectra of the as-made iron nanoparticle sample in Figure 51 showed a 45% relative intensity for α-Fe (component 1), a 36% relative intensity for zero-valent iron (component 2), a 4% Fe^{3+} oxide (component 3) intensity, and a 15% Fe^{2+} oxide (component 4) relative intensity, showing an overall ratio of ~80%/20% iron/iron oxide. For the final time interval, 5 hours of aging, α-Fe intensity totaled 27%, zero-valent iron intensity decreased to 25%, Fe^{3+} oxide intensity increased to 14%, and Fe^{2+} increased to 34%, totaling an overall ratio of ~52%/48% iron/iron oxide.

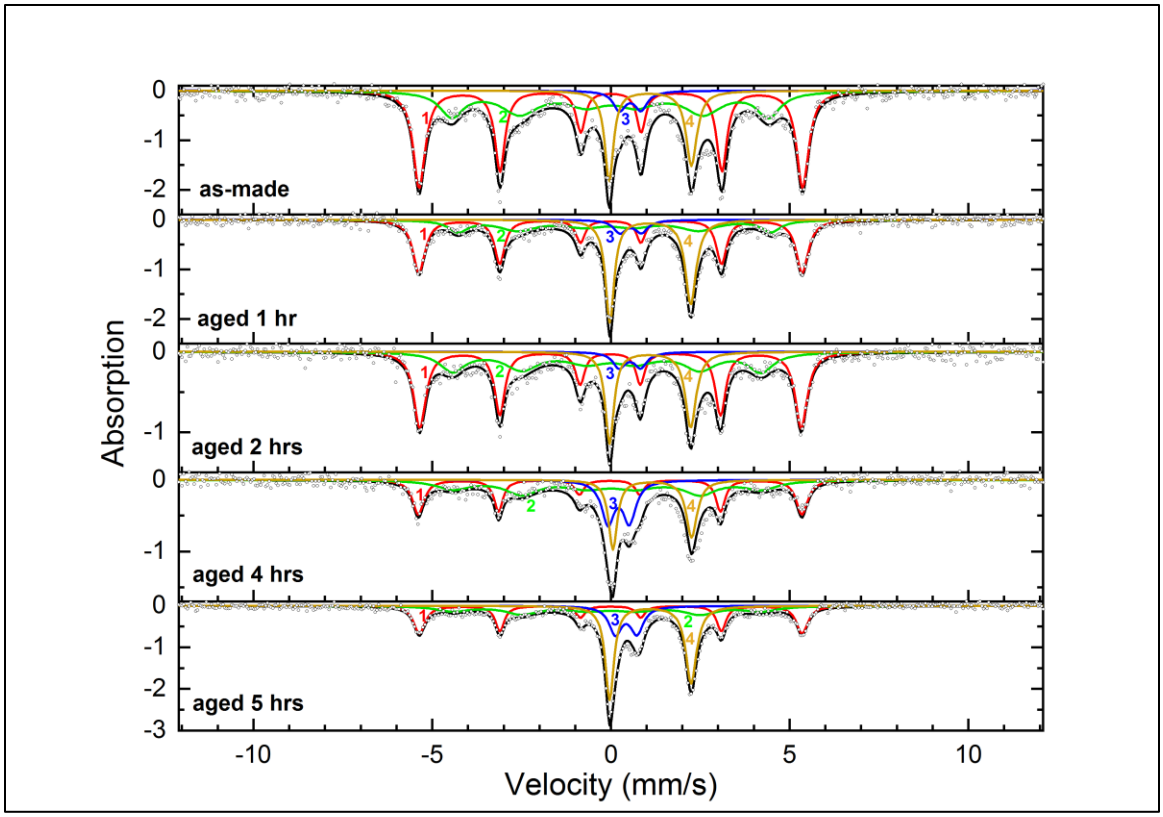


Figure 51. Stacked ^{57}Fe Mössbauer spectra of AE003 iron nanoparticles at one-hour intervals throughout an aging process in air, measured at 293 K

Table 22. Values of hyperfine parameters derived from fitting AE003 metallic iron nanoparticles prepared at one-hour intervals of room temperature ambient oxidation. B_{hf} is the hyperfine magnetic field, δ is the isomer shift, ΔE_Q is the quadrupole splitting, and Γ is the linewidth (FWHM). Typical errors are ±0.5 mm/s for B_{hf}, ±0.02 mm/s for δ, ΔE_Q, and Γ and ±3% for relative area

Sample	Component	B_{hf} (T)	δ (mm/s)	ΔE_Q (mm/s)	Γ (mm/s)	Relative area (%)	Attribution
as-made	1	33.3	0.00	0.00	0.41	45	α-Fe
	2	27.5	0.00	-0.03	0.80	36	amorphous ZVI
	3	-	0.54	0.60	0.43	4	Fe^{3+} oxides
	4	-	1.10	2.31	0.36	15	Fe^{2+} impurities
aged 1 hour	1	33.1	-0.02	0.01	0.41	43	α-Fe
	2	26.8	-0.06	-0.11	0.65	33	amorphous ZVI
	3	-	0.53	0.60	0.43	5	Fe^{3+} oxides
	4	-	1.10	2.27	0.36	19	Fe^{2+} impurities
aged 2 hours	1	33.1	0.00	0.00	0.41	41	α-Fe
	2	27.1	0.02	-0.18	0.85	26	amorphous ZVI
	3	-	0.55	0.60	0.43	5	Fe^{3+} oxides
	4	-	1.10	2.27	0.36	28	Fe^{2+} impurities
aged 4 hours	1	33.3	-0.03	0.02	0.41	24	α-Fe
	2	26.8	-0.06	-0.11	1.15	39	amorphous ZVI
	3	-	0.25	0.60	0.43	14	Fe^{3+} oxides
	4	-	1.15	2.22	0.40	23	Fe^{2+} impurities
aged 5 hours	1	33.2	-0.01	0.01	0.39	27	α-Fe
	2	26.7	-0.05	-0.11	1.14	25	amorphous ZVI
	3	-	0.43	0.60	0.43	14	Fe^{3+} oxides
	4	-	1.10	2.29	0.36	34	Fe^{2+} impurities

There was a large amount of variation among individual spectral components between each time interval (most likely attributed to varying degrees of Fe^{2+} impurities once the nanoparticle powder was split into different samples), but the general trend of oxidation percentage increasing with exposure time was maintained across the series and was determined to be approximately 5.3%/hour by linear fitting of oxidation data in origin (Appendix Figure A61). Fe^{3+} oxide percentage had its largest increase between the 2 and 4-hour oxidation intervals.

AE013A/B: Syringe Pump $FeCl_3$ Reduction in Argon Flow with PEG Coating

Following the oxidation results from both syringe pump $FeCl_3$ reduction in air (AE001, AE003) and dropwise $FeCl_3$ reduction in argon (AE007) syntheses, another ambient oxidation experiment was conducted in order to investigate the efficacy of coating iron nanoparticles with polyethylene glycol (PEG) for deterring oxidation. Metallic iron nanoparticles were synthesized and coated, separated into coated and uncoated samples, and left to oxidize in air at room temperature for one hour. Mössbauer measurements were collected immediately following synthesis and 1-hour after synthesis.

The room-temperature Mössbauer spectra of PEG-coated AE013A can be seen below in Figure 52. The chemical composition of as-made AE013A nanoparticles was previously discussed in the general Mössbauer results section on pages 79-81. As-made AE013A nanoparticles were shown to be comprised of 23% α-Fe (component 1), 65% amorphous zero-valent iron nanoparticles (component 2), 10% ferric oxides/hydroxides (component 3), 2% Fe^{2+} impurities / partially reacted iron (component 4).

The room-temperature Mössbauer spectra of PEG-coated AE013A nanoparticles after one hour of ambient oxidation can be seen in Figure 52. The spectra is composed of five components, a narrow sextet (component 1, red line), a broad interior sextet (component 2, green line),

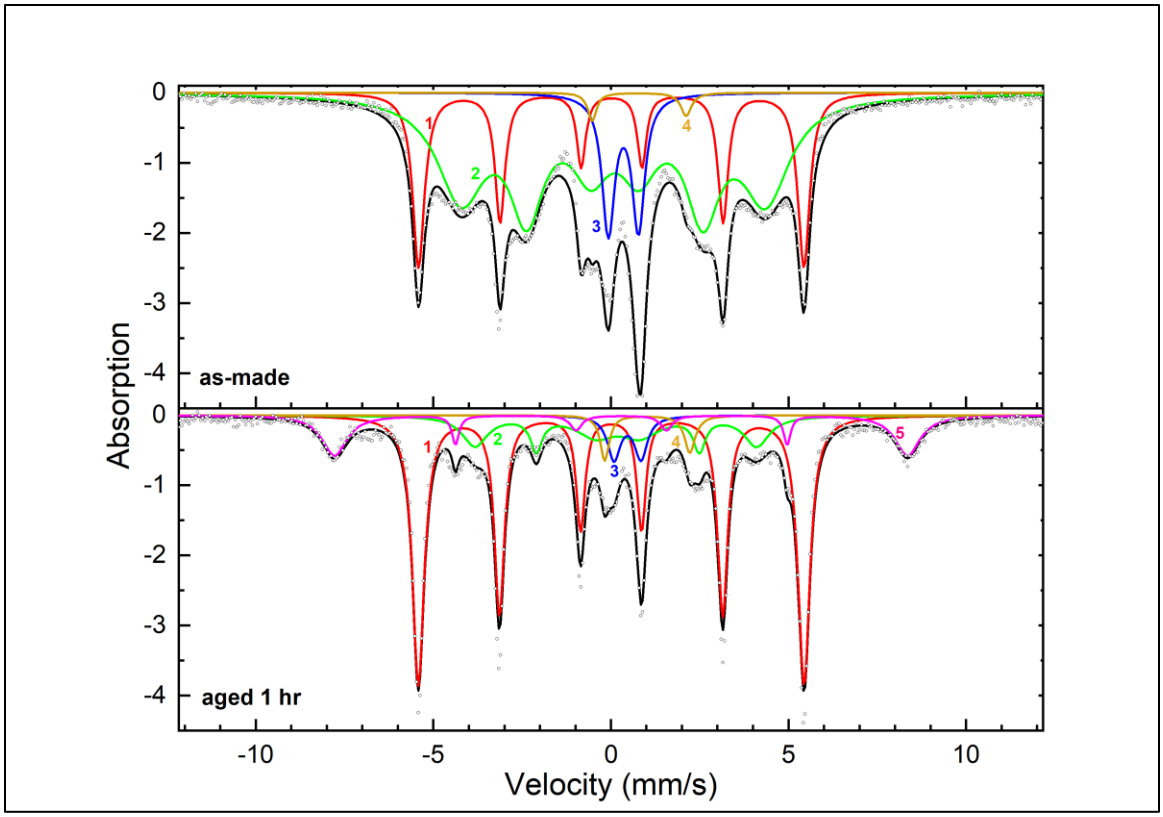


Figure 52. Stacked ^{57}Fe Mössbauer spectra of as-made AE013A PEG-coated iron nanoparticles and one hour oxidized nanoparticles in air, measured at 293 K

Finally, the exterior broad sextet (component 5) with hyperfine field 49.7 T, isomer shift 0.28 mm/s, and quadrupole splitting -0.01 mm/s is representative of Fe^{3+} ions in γ-Fe_2O_3 in the shell of larger nanoparticles or agglomerates [60, 61]. two split doublets (component 3, blue line)/(component 4, yellow line), and a broad exterior sextet (component 5, pink line). The narrow sextet (component 1) with magnetic hyperfine field 33.4 T, isomer shift 0.00 mm/s, and quadrupole splitting 0.00 mm/s is characteristic of crystalline α-Fe in the core. The interior broad sextet (component 2) with hyperfine field 24.4 T, isomer shift 0.15 mm/s, and quadrupole splitting -0.06 mm/s corresponds to amorphous zero-valent iron nanoparticles. The split doublet (component 3) with isomer shift 0.45 mm/s and quadrupole splitting 0.76 mm/s can be attributed to Fe^{3+} ions in the oxide or hydroxide phase such as superparamagnetic γ-Fe_2O_3 or ferrihydrite. These ions are typically located at the particle's outer surface as the shell interacts with the outer environs. The split doublet with isomer shift 1.01 mm/s and quadrupole splitting 2.38 mm/s corresponds to partially reacted/oxidized iron oxide phases that occurred during sample synthesis.

Table 23 shows a 60% relative intensity for α-Fe (component 1), 18% relative intensity for amorphous zero-valent iron nanoparticles (component 2), a 5% relative intensity for superparamagnetic ferric oxide/hydroxide (component 3), a 4% relative intensity for Fe^{2+} impurities / partially reacted iron (component 4), and a 13% relative intensity for larger shell oxides like γ-Fe_2O_3.

The room-temperature Mössbauer spectra of uncoated AE013B can be seen below in Figure 53. The chemical composition of as-made AE013B nanoparticles was previously discussed in the general Mössbauer results section on pages 82-84. As-made AE013B nanoparticles were shown to be comprised of 38% α-Fe (component 1), 39% amorphous zero-valent iron nanoparticles (component 2), 21% ferric oxide/hydroxide (component 3), and 2% Fe^{2+} impurities/partially reacted iron (component 4).

Table 23. Values of hyperfine parameters derived from fitting AE013A PEG-coated metallic iron nanoparticles and after one hour of ambient oxidation. B_{hf} is the hyperfine magnetic field, δ is the isomer shift, ΔE_Q is the quadrupole splitting, and Γ is the linewidth (FWHM). Typical errors are ±0.5 mm/s for B_{hf}, ±0.02 mm/s for δ, ΔE_Q, and Γ and ±3% for relative area

Sample	Component	B_{hf} (T)	δ (mm/s)	ΔE_Q (mm/s)	Γ (mm/s)	Relative area (%)	Attribution
as-made	1	33.6	0.01	-0.01	0.41	23	α-Fe
	2	26.6	0.09	-0.04	1.62	65	amorphous ZVI
	3	-	0.35	0.85	0.43	10	Fe^{3+} oxides
	4	-	0.79	2.65	0.36	2	Fe^{2+} impurities
aged 1-hr	1	33.4	0.00	0.00	0.41	60	α-Fe
	2	24.4	0.16	-0.06	0.85	18	amorphous ZVI
	3	-	0.45	0.76	0.43	5	Fe^{3+} oxides
	4	-	1.01	2.38	0.36	4	Fe^{2+} impurities
	5	49.7	0.28	0.00	0.85	13	γ-Fe_2O_3

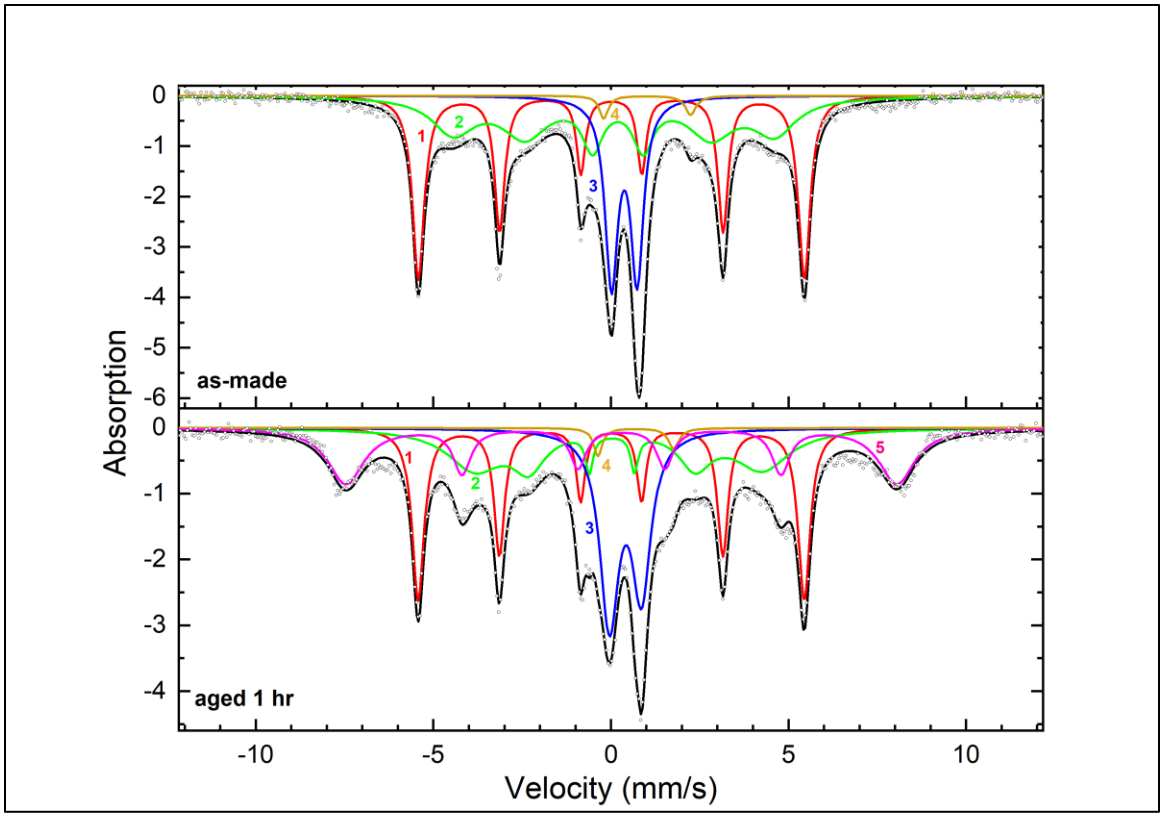


Figure 53. Stacked ^{57}Fe Mössbauer spectra of as-made AE013B uncoated iron nanoparticles and one hour oxidized nanoparticles in air, measured at 293 K

The room-temperature Mössbauer spectra of uncoated AE013B nanoparticles after one hour of ambient oxidation can be seen in Figure 53. The spectrum is composed of five components, a narrow sextet (component 1, red line), a broad interior sextet (component 2, green line), two split doublets (component 3, blue line)/(component 4, yellow line), and a broad exterior sextet (component 5, pink line).

The narrow sextet (component 1) with magnetic hyperfine field 33.4 T, isomer shift 0.00 mm/s, and quadrupole splitting 0.00 mm/s is characteristic of crystalline α-Fe in the core. The interior broad sextet (component 2) with hyperfine field 24.9 T, isomer shift 0.11 mm/s, and quadrupole splitting 0.19 mm/s corresponds to amorphous zero-valent iron nanoparticles. The split doublet (component 3) with isomer shift 0.39 mm/s and quadrupole splitting 0.90 mm/s can be attributed to Fe^{3+} ions in oxide or hydroxide phases such as superparamagnetic γ-Fe_2O_3 or ferrihydrite. These ions are typically located at the particle's outer surface as the shell interacts with the outer environs. The split doublet with isomer shift 0.69 mm/s and quadrupole splitting 2.12 mm/s corresponds to partially reacted/oxidized iron oxide phases that occurred during sample synthesis. Finally, the exterior broad sextet (component 5) with hyperfine field 47.8 T, isomer shift 0.28 mm/s, and quadrupole splitting 0.00 mm/s is representative of Fe^{3+} ions γ-Fe_2O_3 in the shell of larger nanoparticles or agglomerates.

Table 24 shows a 28% relative intensity for α-Fe (component 1), 25% relative intensity for amorphous zero-valent iron nanoparticles (component 2), a 22% relative intensity for ferric oxides/hydroxides (component 3), a 2% relative intensity for Fe^{2+} impurities / partially reacted iron (component 4), and a 23% relative intensity for larger shell oxides like γ-Fe_2O_3.

When comparing as-made and one-hour aged nanoparticle samples, significantly more oxidation occurred over the course of aging for uncoated samples..

Table 24. Values of hyperfine parameters derived from fitting AE013B uncoated metallic iron nanoparticles and after one hour of ambient oxidation. B_{hf} is the hyperfine magnetic field, δ is the isomer shift, ΔE_Q is the quadrupole splitting, and Γ is the linewidth (FWHM). Typical errors are ±0.5 mm/s for B_{hf}, ±0.02 mm/s for δ, ΔE_Q, and Γ and ±3% for relative area

Sample	Component	B_{hf} (T)	δ (mm/s)	ΔE_Q (mm/s)	Γ (mm/s)	Relative area (%)	Attribution
as-made	1	33.7	0.01	-0.02	0.41	38	α-Fe
	2	28.1	0.14	-0.11	1.44	39	amorphous ZVI
	3	-	0.38	0.73	0.43	21	Fe^{3+} oxides
	4	-	1.02	2.45	0.36	2	Fe^{2+} impurities
aged 1-hr	1	33.4	0.00	0.00	0.41	28	α-Fe
	2	24.9	0.11	0.19	1.87	25	amorphous ZVI
	3	-	039	0.90	0.64	22	Fe^{3+} oxides
	4	-	0.69	2.12	0.36	2	Fe^{2+} impurities
	5	47.8	0.28	0.00	0.60	23	γ-Fe_2O_3

After combining all metallic iron (α-Fe, amorphous ZVI) and all iron oxides (components 3-5) into a single category, the AE013A PEG-coated nanoparticle sample went from an 88%/12% total iron/iron oxide ratio to a 78%/22% ratio of iron/iron oxides after one hour of ambient oxidation. The AE013B uncoated sample experienced a reduction of 77%/23% iron/iron oxides to a 53%/47% ratio of iron/iron oxides over a similar period of oxidation.

The increased oxide content came at the expense of decreased amorphous ZVI content. Polyethylene glycol coating shielded the nanoparticles from interacting with oxygen in the synthesis flask and atmosphere, helping to preserve metallic iron content in both the as-made sample and the one-hour oxidized sample. A stacked comparison of Mössbauer spectra for as-made AE013A/AE013B and one-hour oxidized AE013A/AE013B be seen in Figures A63 and A64 and Tables A34 and A35, respectively in the Appendix.

AE014A/B: Syringe Pump $FeCl_3$ Reduction in Argon Flow with PEG Coating

Following the oxidation results from AE013A and AE013B, another ambient oxidation experiment was conducted in order to investigate the efficacy of coating iron nanoparticles with polyethylene glycol (PEG) for deterring oxidation on a longer timescale with more intermediary measurements. A larger amount of metallic iron nanoparticles was synthesized and coated, separated into coated and uncoated samples, and left to oxidize in air at room temperature. Mössbauer measurements were collected immediately post synthesis and in 30-minute intervals of ambient oxidation up to 2 hours.

The room-temperature Mössbauer spectra of uncoated AE014A nanoparticles at various stages of ambient oxidation can be seen below in Figure 54. The spectra are composed of five components, a narrow sextet (component 1, red line), a broad interior sextet (component 2, green line),

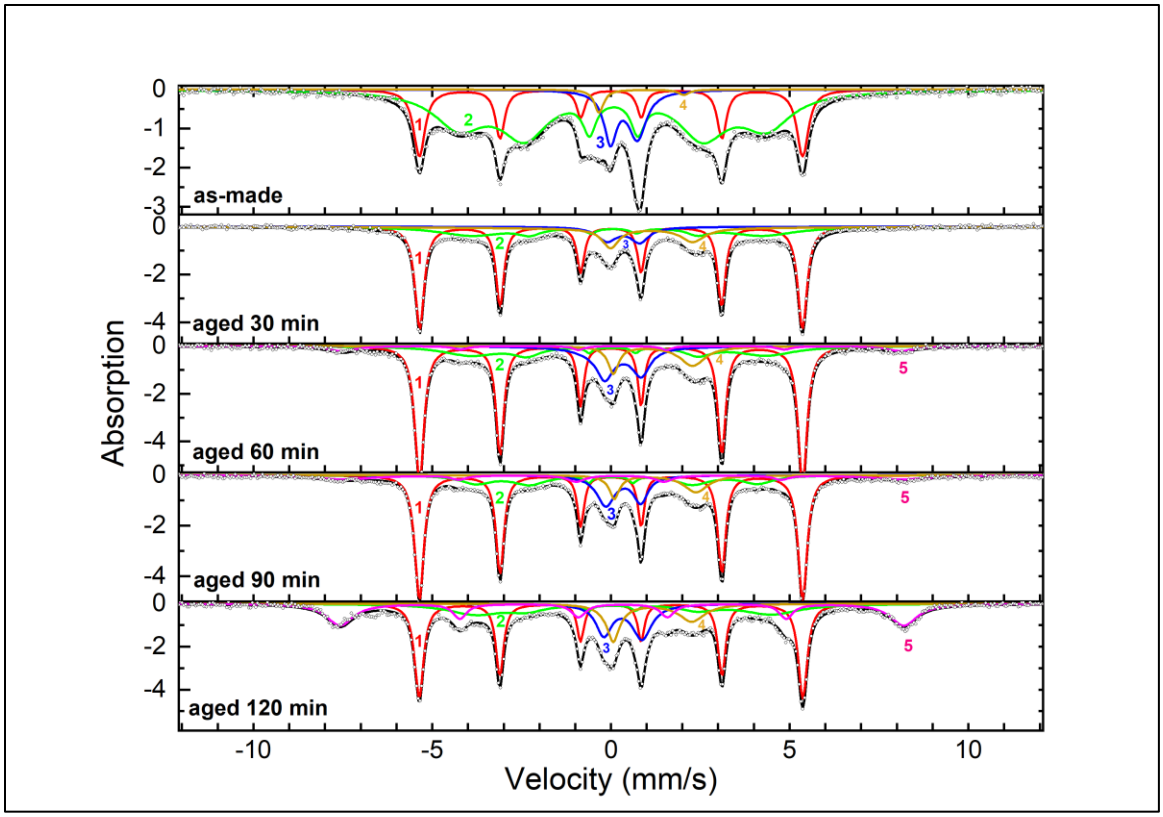


Figure 54. Stacked time series ^{57}Fe Mössbauer spectra of as-made AE014A PEG-coated iron nanoparticles oxidized at 30-minute intervals in air, measured at 293 K

two split doublets (component 3, blue line)/(component 4, yellow line), and a broad exterior sextet (component 5, pink line). Hyperfine parameters can be seen in Table 25.

At all stages of oxidative progression, AE014A's narrow sextets (component 1) with magnetic hyperfine field ~33.2 T, isomer shift 0.00 mm/s, and quadrupole splitting 0.00 mm/s are characteristic of crystalline α-Fe in the core. The interior broad sextets (component 2) with hyperfine field 24.4-26.7 T, isomer shift 0.06-0.19 mm/s, and quadrupole splitting ~0.17 mm/s correspond to amorphous zero-valent iron nanoparticles. The split doublets (component 3) with isomer shift 0.35 mm/s and quadrupole splitting ~0.93 mm/s can be attributed to Fe^{3+} ions in oxide or hydroxide phases such as superparamagnetic γ-Fe_2O_3 or ferrihydrite.

These ions are typically located at the particle's outer surface as the shell interacts with the outer environs. The split doublets with isomer shift ~1.16 mm/s and quadrupole splitting ~2.30 mm/s correspond to partially reacted/oxidized iron oxide phases that occurred during sample synthesis. Finally, the exterior broad sextets (component 5) with hyperfine field 48.5 T, isomer shift 0.30 mm/s, and quadrupole splitting -0.03 mm/s are representative of Fe^{3+} ions in γ-Fe_2O_3 in the shell of larger nanoparticles or agglomerates.

Table 26 shows the breakdown of AE014A's total metallic iron and iron oxide content over the course of ambient oxidation. AE014A experienced a steady progression of oxidation equal to approximately 14%/hour (determined with linear fitting, seen in Appendix Figure A62) throughout each time period, from an initial 86%/13% iron/iron oxide ratio to 55%/45% after 120 minutes of ambient atmosphere exposure.

Table 25. Values of hyperfine parameters derived from fitting AE014A PEG-coated metallic iron nanoparticles prepared at 30-min intervals of room temperature ambient oxidation. B_{hf} is the hyperfine magnetic field, δ is the isomer shift, ΔE_Q is the quadrupole splitting, and Γ is the linewidth (FWHM). Typical errors are ±0.5 mm/s for B_{hf}, ±0.02 mm/s for δ, ΔE_Q, and Γ and ±3% for relative area

Sample	Component	B_{hf} (T)	δ (mm/s)	ΔE_Q (mm/s)	Γ (mm/s)	Relative area (%)	Attribution
as-made	1	33.2	0.00	0.00	0.38	22	α-Fe
	2	26.7	0.06	-0.02	1.67	65	amorphous ZVI
	3	-	0.36	0.76	0.61	11	Fe^{3+} oxides
	4	-	0.85	2.37	0.37	2	Fe^{2+} impurities
aged 30 min	1	33.2	0.00	0.00	0.31	54	α-Fe
	2	25.2	0.12	0.09	2.21	22	amorphous ZVI
	3	-	0.35	0.93	0.61	8	Fe^{3+} oxides
	4	-	1.14	2.31	0.80	16	Fe^{2+} impurities
aged 60 min	1	33.2	0.00	0.00	0.30	55	α-Fe
	2	25.6	0.12	0.17	1.06	17	amorphous ZVI
	3	-	0.34	1.03	0.48	14	Fe^{3+} oxides
	4	-	1.18	2.22	0.82	9	Fe^{2+} impurities
	5	48.5	0.30	-0.03	2.04	5	γ-Fe_2O_3
aged 90 min	1	33.3	0.00	0.00	0.30	55	α-Fe
	2	24.4	0.08	0.17	1.88	15	amorphous ZVI
	3	-	0.34	0.98	0.64	12	Fe^{3+} oxides
	4	-	1.24	2.29	0.86	8	Fe^{2+} impurities
	5	48.3	0.28	-0.07	0.92	10	γ-Fe_2O_3
aged 120 min	1	33.2	0.00	0.00	0.30	36	α-Fe
	2	25.6	0.19	0.32	1.86	18	amorphous ZVI
	3	-	0.33	1.07	0.60	13	Fe^{3+} oxides
	4	-	1.16	2.20	0.85	11	Fe^{2+} impurities
	5	48.9	0.32	-0.03	0.94	22	γ-Fe_2O_3

Table 26. Breakdown of AE014A's total metallic iron and iron oxide percentages over time

AE014A	Component	Total %
as-made	Iron	87
	Iron Oxides	13
aged 30 min	Iron	76
	Iron Oxides	24
aged 60 min	Iron	72
	Iron Oxides	28
aged 90 min	Iron	69
	Iron Oxides	31
aged 120 min	Iron	55
	Iron Oxides	45

The room-temperature Mössbauer spectra of uncoated AE014B nanoparticles after one hour of ambient oxidation can be seen below in Figure 55. The spectrum is composed of five components, a narrow sextet (component 1, red line), a broad interior sextet (component 2, green line), two split doublets (component 3, blue line)/(component 4, yellow line), and a broad exterior sextet (component 5, pink line). Hyperfine parameters can be seen in Table 27.

At all stages of aging, AE014B's narrow sextets (component 1) with magnetic hyperfine field ~33.4 T, isomer shift 0.00 mm/s, and quadrupole splitting 0.00 mm/s are characteristic of crystalline α-Fe in the core. The interior broad sextets (component 2) with hyperfine field 24.5-27.0 T, isomer shift 0.08-0.22 mm/s, and quadrupole splitting ~0.22 mm/s correspond to amorphous zero-valent iron nanoparticles. The split doublets (component 3) with isomer shift 0.35-0.44 mm/s and quadrupole splitting ~0.86 mm/s can be attributed to Fe^{3+} ions in oxide phases such as superparamagnetic γ-Fe_2O_3.

These ions are typically located at the particle's outer surface as the shell interacts with the outer environs. The split doublets with isomer shift ~0.85 mm/s and quadrupole splitting ~2.36 mm/s correspond to partially reacted/oxidized iron oxide phases that occurred during sample synthesis. Finally, the exterior broad sextets (component 5) with hyperfine field 48.1 T, isomer shift 0.33 mm/s, and quadrupole splitting -0.01 mm/s are representative of Fe^{3+} ions in γ-Fe_2O_3 in the shell of larger nanoparticles or agglomerates.

Table 28 shows the breakdown of AE014B's total metallic iron and iron oxide content over the course of ambient oxidation. AE014B experienced the entirety of its oxidation in the first 30-minute interval, from a 77%/23% to a 35%/65% iron/iron oxide ratio, and largely held steady over the rest of the oxidation experiment.

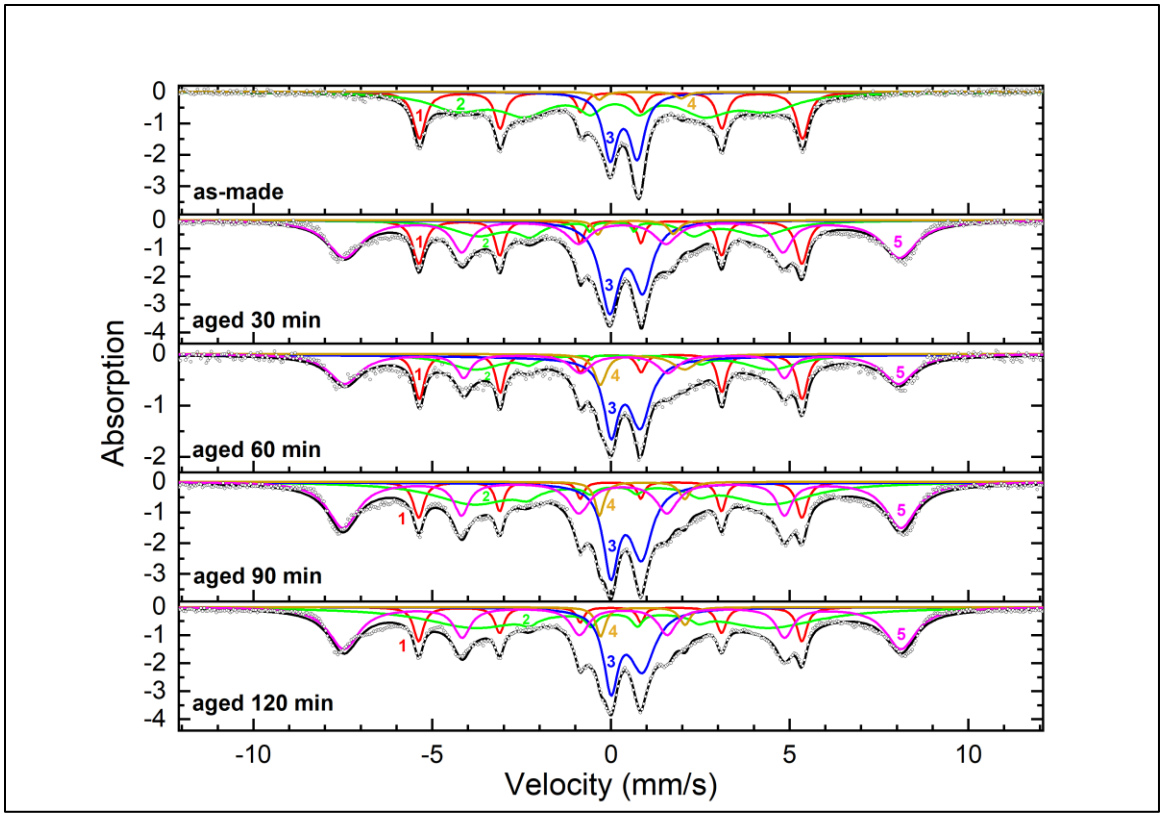


Figure 55. Stacked time series ^{57}Fe Mössbauer spectra of as-made AE014B uncoated iron nanoparticles oxidized at 30-minute intervals in air, measured at 293 K

Table 27. Values of hyperfine parameters derived from fitting AE014B uncoated metallic iron nanoparticles prepared at 30-min intervals of room temperature ambient oxidation. B_{hf} is the hyperfine magnetic field, δ is the isomer shift, ΔE_Q is the quadrupole splitting, and Γ is the linewidth (FWHM). Typical errors are ±0.5 mm/s for B_{hf}, ±0.02 mm/s for δ, ΔE_Q, and Γ and ±3% for relative area

Sample	Component	B_{hf} (T)	δ (mm/s)	ΔE_Q (mm/s)	Γ (mm/s)	Relative area (%)	Attribution
as-made	1	33.2	0.00	0.00	0.41	25	α-Fe
	2	27.0	0.08	-0.05	1.89	52	amorphous ZVI
	3	-	0.35	0.76	0.50	21	Fe^{3+} oxides
	4	-	0.82	2.29	0.37	2	Fe^{2+} impurities
aged 30 min	1	33.2	-0.01	-0.01	0.40	17	α-Fe
	2	24.5	0.13	0.21	1.69	18	amorphous ZVI
	3	-	0.43	0.93	0.64	24	Fe^{3+} oxides
	4	-	0.69	2.12	0.36	2	Fe^{2+} impurities
	5	48.1	0.32	-0.01	1.17	39	γ-Fe_2O_3
aged 60 min	1	33.2	0.00	-0.01	0.35	17	α-Fe
	2	25.7	0.22	0.22	1.86	17	amorphous ZVI
	3	-	0.41	0.82	0.71	32	Fe^{3+} oxides
	4	-	0.88	2.36	0.83	6	Fe^{2+} impurities
	5	48.1	0.33	-0.06	1.08	28	γ-Fe_2O_3
aged 90 min	1	33.3	-0.02	-0.01	0.36	10	α-Fe
	2	25.8	0.20	0.27	2.75	26	amorphous ZVI
	3	-	0.42	0.86	0.73	28	Fe^{3+} oxides
	4	-	0.87	2.38	0.36	3	Fe^{2+} impurities
	5	48.4	0.33	-0.03	1.04	33	γ-Fe_2O_3
aged 120 min	1	33.3	-0.02	-0.01	0.33	10	α-Fe
	2	25.5	0.20	0.22	3.39	33	amorphous ZVI
	3	-	0.44	0.88	0.86	21	Fe^{3+} oxides
	4	-	0.89	2,36	0.36	3	Fe^{2+} impurities
	5	48.3	0.33	-0.02	1.03	33	γ-Fe_2O_3

Table 28. Breakdown of AE014B's total metallic iron and iron oxide percentages over time

AE014B	Component	Total %
as-made	Iron	77
	Iron Oxides	23
aged 30 min	Iron	35
	Iron Oxides	65
aged 60 min	Iron	33
	Iron Oxides	67
aged 90 min	Iron	36
	Iron Oxides	64
aged 120 min	Iron	44
	Iron Oxides	56

When comparing polyethylene glycol coated (AE014A) and uncoated (AE014B) metallic iron nanoparticles, PEG coating preserves metallic iron content not only immediately following synthesis, but also at each subsequent 30-minute measurement interval. Metallic iron preservation is important for maintaining the desirable magnetic properties of the iron nanoparticles for applications in hyperthermia and MRI contrast.

Relaxometry

A visual map detailing the magnetic resonance response of AE001 and AE002 nanoparticle sample solutions to a 4.7 T field can be seen below in Figure 56. When used in tandem with the recorded relaxation times shown in Table 29, it becomes apparent that all concentrations of AE001 nanoparticles had a significantly different visual and numerical relaxation response than the deionized water control sample. This was true for both T_2 and T_1 measurements, with the T_2 differences being more discernible.

AE002 samples had recorded relaxation times similar to deionized water and cannot be visually differentiated on the T_2/T_1 map. Because the recorded signal response of AE001 nanoparticles significantly differed from the deionized water control, this result serves as a proof of concept for use of the nanoparticles as a potential MRI contrast agent.

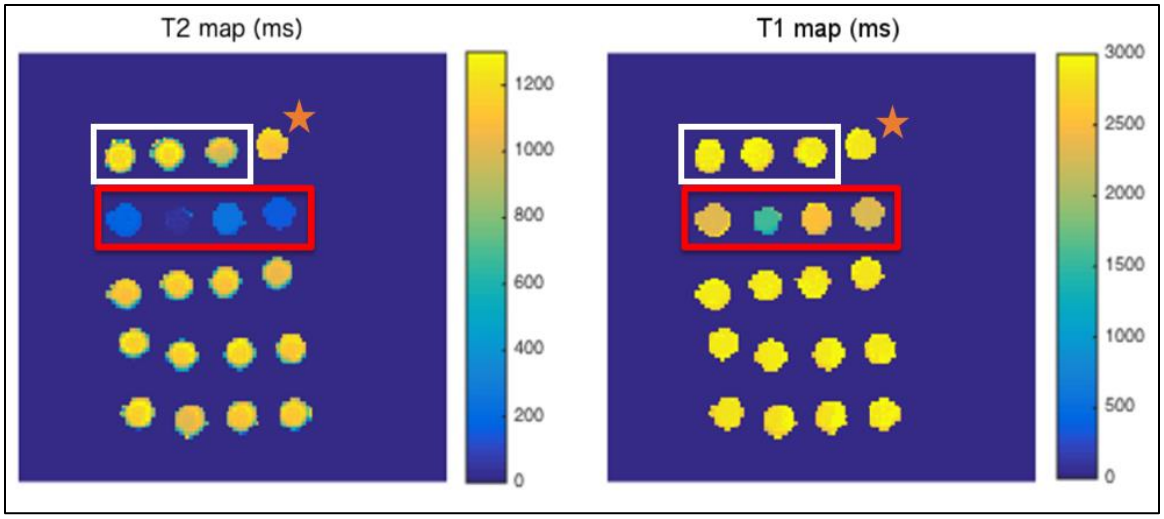


Figure 56. T_2 and T_1 map with varying concentrations of metallic iron nanoparticle samples. Samples denoted with a red box are AE001 nanoparticles increasing in concentration from left to right. Samples denoted with a white box are AE002 nanoparticles increasing in concentration from left to right. A deionized water control is denoted with an orange star

Table 29. Table of T_2 and T_1 relaxation time results

Sample	Concentration	T_2 (ms)	T_2 std (ms)	T_1 (ms)	T_1 std (ms)
AE001	1 (lowest)	182.6	3.23	2332	31.9
	2	45.7	8.67	1563	10.3
	3	250.5	3.28	2514	22.6
	4 (highest)	158.6	2.74	2290	18.8
AE002	1 (lowest)	1192	30.9	2899	45.5
	2	1187	29.9	2922	66.7
	3 (highest)	992	39.5	2906	77.3
DI Water	1	1190	36.7	2962	13.3

CHAPTER IV
CONCLUSIONS

Nanoscale metallic iron nanoparticles with applications as magnetic resonance imaging (MRI) contrast agents or as a medium for hyperthermia treatment of cancer were synthesized through a facile Fe^{3+} reduction reaction with sodium borohydride. Silica and polyethylene glycol (PEG) coatings were investigated for imparting biocompatibility and reducing oxidation of the nanoparticles, thereby preserving metallic iron content and desired magnetic properties. The synthesis route produced metallic iron nanoparticles that aggregated as spheroids or arranged as sintered aggregates/chains. Final morphology was determined by whether nanoparticles were stored in ethanol (spheroids) or dried and stored as powder (sintered aggregates/chains).

TEM of spheroid nanoparticles stored in ethanol showed nanoparticles ranging between 10-80 nm in diameter. SEM of dried nanoparticle powder revealed chains on the order of 50-80 nm that had a core-shell structure containing a crystalline α-Fe core surrounded by a combination of amorphous iron and various iron oxides and oxide-hydroxides (maghemite, ferrihydrite). Shell iron oxides formed through the oxidation of the highly reactive iron surface with oxygen and moisture in the ambient atmosphere.

Mössbauer spectroscopy experiments confirmed the chemical existence of these various iron and oxide species and quantified their change in proportion over multiple time intervals. The majority of uncoated nanoscale iron's oxidation occurs within the first several hours following synthesis. Oxidation rate, however, slows once an adequate passivation layer is formed. Polyethylene glycol (PEG) coating was shown to retard oxidation rate when compared to uncoated analogues. Relaxometry showed that compared to the deionized water control, as-made metallic iron nanoparticles generated a significantly different magnetic resonance signal in a 4.7 T field, demonstrating promise as a potential T_2 MRI contrast agent.

REFERENCES

1. Hacliipanayis, C.G., et al., *Metallic Iron Nanoparticles for MRI Contrast Enhancement and Local Hyperthermia.* Small, 2008. **4**(11): p. 1925-1929.
2. Bakhtiary, Z., et al., *Targeted superparamagnetic iron oxide nanoparticles for early detection of cancer: Possibilities and challenges.* Nanomedicine-Nanotechnology Biology and Medicine, 2016. **12**(2): p. 287-307.
3. Huber, D.L., *Synthesis, Properties, and Applications of Iron Nanoparticles.* Small, 2005. **1**(5): p. 482-501.
4. Babes, L., et al., *Synthesis of Iron Oxide Nanoparticles Used as MRI Contrast Agents: A Parametric Study.* Journal of Colloid and Interface Science, 1999. **212**(2): p. 474-482.
5. Neuberger, T., et al., *Superparamagnetic nanoparticles for biomedical applications: Possibilities and limitations of a new drug delivery system.* Journal of Magnetism and Magnetic Materials, 2005. **293**(1): p. 483-496.
6. Gupta, A.K. and M. Gupta, *Synthesis and surface engineering of iron oxide nanoparticles for biomedical applications.* Biomaterials, 2005. **26**(18): p. 3995-4021.
7. Sun, C., J.S.H. Lee, and M. Zhang, *Magnetic nanoparticles in MR imaging and drug delivery.* Advanced Drug Delivery Reviews, 2008. **60**(11): p. 1252-1265.
8. Berry, C.C. and A.S.G. Curtis, *Functionalisation of magnetic nanoparticles for applications in biomedicine.* Journal of Physics D: Applied Physics, 2003. **36**(13): p. R198-R206.
9. Laurent, S., et al., *Magnetic Iron Oxide Nanoparticles: Synthesis, Stabilization, Vectorization, Physicochemical Characterizations, and Biological Applications.* Chemical Reviews, 2008. **108**(6): p. 2064-2110.
10. Wu, K., et al., *Magnetic nanoparticles in nanomedicine: a review of recent advances.* Nanotechnology, 2019. **30**(50): p. 47.
11. Ghosh, N., B.K. Mandal, and K. Mohan Kumar, *Magnetic memory effect in chelated zero valent iron nanoparticles.* Journal of Magnetism and Magnetic Materials, 2012. **324**(22): p. 3839-3841.
12. Zhang, X.Y., et al., *Template synthesis of well-graphitized carbon nanotube arrays.* Materials Science and Engineering: A, 2001. **308**(1): p. 9-12.
13. Lastella, S., et al., *Density control of single-walled carbon nanotubes using patterned iron nanoparticle catalysts derived from phase-separated thin films of a polyferrocene block copolymer.* Journal of Materials Chemistry, 2004. **14**(12): p. 1791-1794.
14. Torres Galvis, H.M., et al., *Supported Iron Nanoparticles as Catalysts for Sustainable Production of Lower Olefins.* Science, 2012. **335**(6070): p. 835.
15. Tartaj, P., et al., *The Iron Oxides Strike Back: From Biomedical Applications to Energy Storage Devices and Photoelectrochemical Water Splitting.* Advanced Materials, 2011. **23**(44): p. 5243-5249.

16. Manikandan, A., et al., *One-Pot Low Temperature Synthesis and Characterization Studies of Nanocrystalline α-Fe2O3 Based Dye Sensitized Solar Cells.* Journal of Nanoscience and Nanotechnology, 2015. **15**(6): p. 4358-4366.
17. Koo, B., et al., *Hollow Iron Oxide Nanoparticles for Application in Lithium Ion Batteries.* Nano Letters, 2012. **12**(5): p. 2429-2435.
18. Li, X.-q., D.W. Elliott, and W.-x. Zhang, *Zero-Valent Iron Nanoparticles for Abatement of Environmental Pollutants: Materials and Engineering Aspects.* Critical Reviews in Solid State and Materials Sciences, 2006. **31**(4): p. 111-122.
19. Noubactep, C., *A CRITICAL REVIEW ON THE PROCESS OF CONTAMINANT REMOVAL IN FE0–H2O SYSTEMS.* Environmental Technology, 2008. **29**(8): p. 909-920.
20. Sun, Y.-P., et al., *Characterization of zero-valent iron nanoparticles.* Advances in Colloid and Interface Science, 2006. **120**(1): p. 47-56.
21. Zhang, W.-x., *Nanoscale Iron Particles for Environmental Remediation: An Overview.* Journal of Nanoparticle Research, 2003. **5**(3): p. 323-332.
22. Üzüm, Ç., et al., *Application of zero-valent iron nanoparticles for the removal of aqueous Co2+ ions under various experimental conditions.* Chemical Engineering Journal, 2008. **144**(2): p. 213-220.
23. Nurmi, J.T., et al., *Characterization and Properties of Metallic Iron Nanoparticles: Spectroscopy, Electrochemistry, and Kinetics.* Environmental Science & Technology, 2005. **39**(5): p. 1221-1230.
24. Alymov, M.I., et al., *Synthesis and characterization of passivated iron nanoparticles.* Mendeleev Communications, 2016. **26**(6): p. 549-551.
25. Pullin, H., et al., *The effect of aqueous corrosion on the structure and reactivity of zero-valent iron nanoparticles.* Chemical Engineering Journal, 2017. **308**: p. 568-577.
26. Petala, E., et al., *Nanoscale zero-valent iron supported on mesoporous silica: Characterization and reactivity for Cr(VI) removal from aqueous solution.* Journal of Hazardous Materials, 2013. **261**: p. 295-306.
27. Kubuki, S., et al., *Mössbauer study of metallic iron and iron oxide nanoparticles having environmental purifying ability.* AIP Conference Proceedings, 2014. **1622**(1): p. 134-141.
28. Pankhurst, Q.A., et al., *Applications of magnetic nanoparticles in biomedicine.* Journal of Physics D: Applied Physics, 2003. **36**(13): p. R167-R181.
29. Pankhurst, Q.A., et al., *Progress in applications of magnetic nanoparticles in biomedicine.* Journal of Physics D: Applied Physics, 2009. **42**(22): p. 224001.
30. Zhang, C.J., et al., *Superparamagnetic iron oxide nanoparticles for MR imaging of pancreatic cancer: Potential for early diagnosis through targeted strategies.* Asia-Pacific Journal of Clinical Oncology, 2016. **12**(1): p. 13-21.

31. Qiao, R.R., C.H. Yang, and M.Y. Gao, *Superparamagnetic iron oxide nanoparticles: from preparations to in vivo MRI applications.* Journal of Materials Chemistry, 2009. **19**(35): p. 6274-6293.
32. Maenosono, S., T. Suzuki, and S. Saita, *Superparamagnetic FePt nanoparticles as excellent MRI contrast agents.* Journal of Magnetism and Magnetic Materials, 2008. **320**(9): p. L79-L83.
33. King, J.E., et al., *Synthesis of Iron Nanoparticles for Enhanced MRI Contrast Agents.* Journal of Nanoscience with Advanced Technology, 2018. **2**(3).
34. Hah, H.Y., *Mössbauer Spectroscopy of Iron Oxide Nanoparticles: Materials for Biomedical Applications*, in *Mechanical, Aerospace, and Biomedical Engineering*. 2018, University of Tennessee.
35. King, J.E., *Development of Iron Nanoparticles for Medical Imaging and Therapeutic Treatments of Glioblastoma Multiforme*, in *Mechanical, Aerospace, and Biomedical Engineering*. 2019, University of Tennessee.
36. van der Zee, J., *Heating the patient: a promising approach?* Ann Oncol, 2002. **13**(8): p. 1173-84.
37. Rosensweig, R.E., *Heating magnetic fluid with alternating magnetic field.* Journal of Magnetism and Magnetic Materials, 2002. **252**: p. 370-374.
38. Blanco-Andujar, C., et al., *High performance multi-core iron oxide nanoparticles for magnetic hyperthermia: microwave synthesis, and the role of core-to-core interactions.* Nanoscale, 2015. **7**(5): p. 1768-1775.
39. Maier-Hauff, K., et al., *Intracranial thermotherapy using magnetic nanoparticles combined with external beam radiotherapy: results of a feasibility study on patients with glioblastoma multiforme.* J Neurooncol, 2007. **81**(1): p. 53-60.
40. Johannsen, M., et al., *Thermotherapy of Prostate Cancer Using Magnetic Nanoparticles: Feasibility, Imaging, and Three-Dimensional Temperature Distribution.* European Urology, 2007. **52**(6): p. 1653-1662.
41. Harvey, P.R. and E. Katznelson, *Modular gradient coil: A new concept in high-performance whole-body gradient coil design.* Magnetic Resonance in Medicine, 1999. **42**(3): p. 561-570.
42. Gneveckow, U., et al., *Description and characterization of the novel hyperthermia- and thermoablation-system MFH 300F for clinical magnetic fluid hyperthermia.* Med Phys, 2004. **31**(6): p. 1444-51.
43. Park, J., et al., *Ultra-large-scale syntheses of monodisperse nanocrystals.* Nature Materials, 2004. **3**(12): p. 891-895.
44. Peng, S., et al., *Synthesis and stabilization of monodisperse Fe nanoparticles.* J Am Chem Soc, 2006. **128**(33): p. 10676-7.
45. Yuvakkumar, R., et al., *PREPARATION AND CHARACTERIZATION OF ZERO VALENT IRON NANOPARTICLES.* Digest Journal of Nanomaterials and Biostructures, 2011. **6**(4): p. 1771-1776.
46. Postek, M.T. and A.E. Vladár, *Does Your SEM Really Tell the Truth?-How Would You Know? Part 4: Charging and its Mitigation.* Proceedings of

SPIE--the International Society for Optical Engineering, 2015. **9636**: p. 963605 (October 21, 2015); doi:10.1117/12.2195344 Text Size: A A A.
47. de Goede, M., *Multi-Energy Deconvolution Scanning Electron Microscopy: The 3D Imaging of Nanostructures using Backscattered Electrons*, in *Physics*. 2014, Vrije Universiteit.
48. Jamei, M.R., M.R. Khosravi, and B. Anvaripour, *Investigation of ultrasonic effect on synthesis of nano zero valent iron particles and comparison with conventional method.* Asia-Pacific Journal of Chemical Engineering, 2013. **8**(5): p. 767-774.
49. Anbouhi, T.S., et al., *Albumin binding, anticancer and antibacterial properties of synthesized zero valent iron nanoparticles.* International Journal of Nanomedicine, 2019. **14**: p. 243-256.
50. Krajewski, M., et al., *Impact of thermal oxidation on chemical composition and magnetic properties of iron nanoparticles.* Journal of Magnetism and Magnetic Materials, 2018. **458**: p. 346-354.
51. Lei, X.-f. and J.-x. Ma, *Synthesis and electrochemical performance of aluminum based composites.* Journal of the Brazilian Chemical Society, 2010. **21**: p. 209-213.
52. Liu, A.R., J. Liu, and W.X. Zhang, *Transformation and composition evolution of nanoscale zero valent iron (nZVI) synthesized by borohydride reduction in static water.* Chemosphere, 2015. **119**: p. 1068-1074.
53. Krajewski, M., et al., *Structural and magnetic properties of iron nanowires and iron nanoparticles fabricated through a reduction reaction.* Beilstein Journal of Nanotechnology, 2015. **6**: p. 1652-1660.
54. Brzozka, K., et al., *Phase Evolution of Iron Nanoparticles Subjected to Thermal Treatment.* Acta Physica Polonica A, 2018. **134**(5): p. 1015-1020.
55. Sharma, V.K., G. ; Nishida, T. , *Mössbauer Spectroscopy: Applications in Chemistry, Biology, and Nanotechnology*. 2013: Wiley.
56. Douvalis, A.P., et al., *A facile synthetic route toward air-stable magnetic nanoalloys with Fe-Ni/Fe-Co core and iron oxide shell.* Journal of Nanoparticle Research, 2012. **14**(9): p. 16.
57. Siddique, M., E. Ahmed, and N.M. Butt, *Particle size effect on Mössbauer parameters in γ-Fe2O3 nanoparticles.* Physica B: Condensed Matter, 2010. **405**(18): p. 3964-3967.
58. Long, G.J., et al., *Mossbauer-Bauer-effect and x-ray-absorption spectral study of sonochemically prepared amorphous iron.* Physical Review B, 1998. **57**(17): p. 10716-10722.
59. Khalil, H., et al., *Synthesis of zerovalent nanophase metal particles stabilized with poly(ethylene glycol).* Langmuir, 2004. **20**(16): p. 6896-6903.
60. Muxworthy, A.R., E. Schmidbauer, and N. Petersen, *Magnetic properties and Mössbauer spectra of urban atmospheric particulate matter: a case study from Munich, Germany.* Geophysical Journal International, 2002. **150**(2): p. 558-570.

61. Morris, R.V., et al., *Spectral and other physicochemical properties of submicron powders of hematite (α-Fe2O3), maghemite (γ-Fe2O3), magnetite (Fe3O4), goethite (α-FeOOH), and lepidocrocite (γ-FeOOH).* Journal of Geophysical Research: Solid Earth, 1985. **90**(B4): p. 3126-3144.

APPENDIX

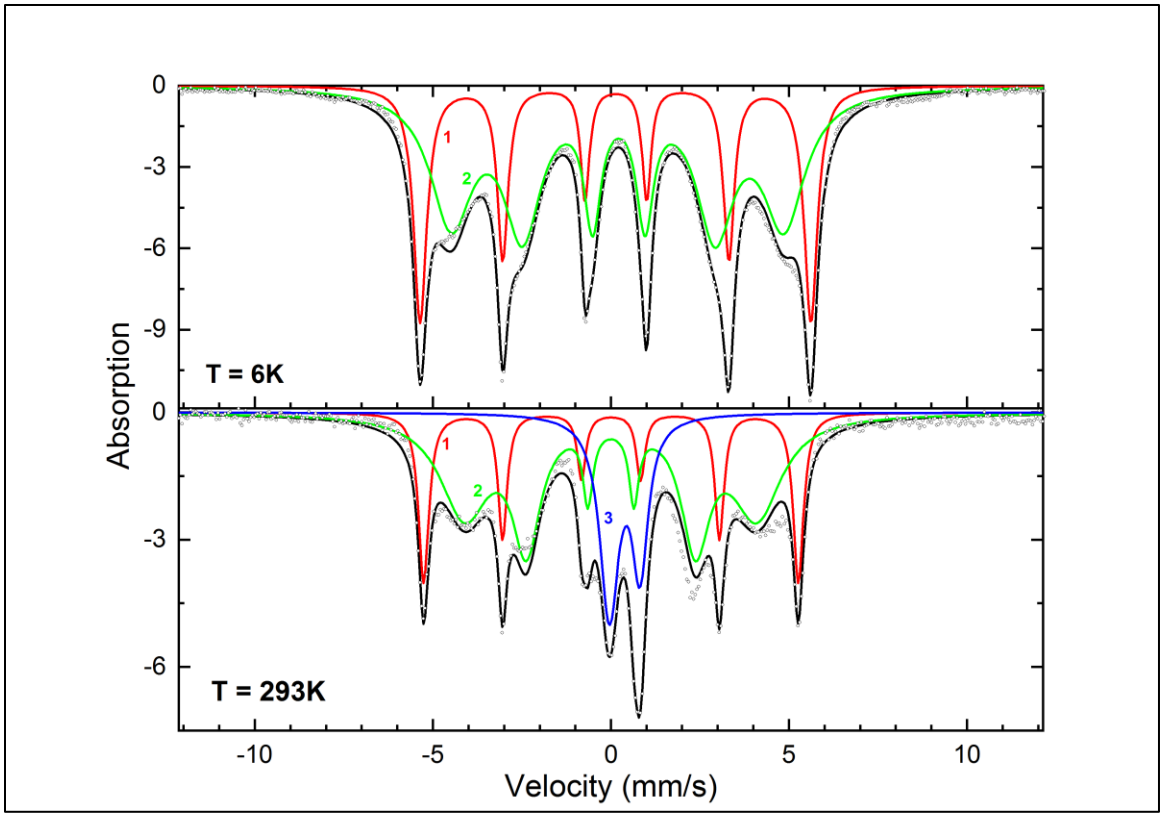


Figure A57. Stacked ^{57}Fe Mössbauer spectra of as-made AE005 uncoated metallic iron nanoparticles, measured at 6K and 293K

Table A30. Values of hyperfine parameters derived from fitting as-made AE005 uncoated metallic iron nanoparticles at 6K and 293K. B_{hf} is the hyperfine magnetic field, δ is the isomer shift, ΔE_Q is the quadrupole splitting, and Γ is the linewidth (FWHM). Typical errors are ±0.5 mm/s for B_{hf}, ±0.02 mm/s for δ, ΔE_Q, and Γ and ±3% for relative area

Sample	Component	B_{hf} (T)	δ (mm/s)	ΔE_Q (mm/s)	Γ (mm/s)	Relative area (%)	Attribution
AE005 6K	1	34.0	0.13	-0.01	0.45	32	α-Fe
	2	29.0	0.20	-0.03	1.44	68	amorphous ZVI
AE005 293K	1	32.6	0.00	0.00	0.35	22	α-Fe
	2	25.5	0.00	0.00	1.68	58	amorphous ZVI
	3	-	0.38	0.86	0.54	20	Fe^{3+} oxides

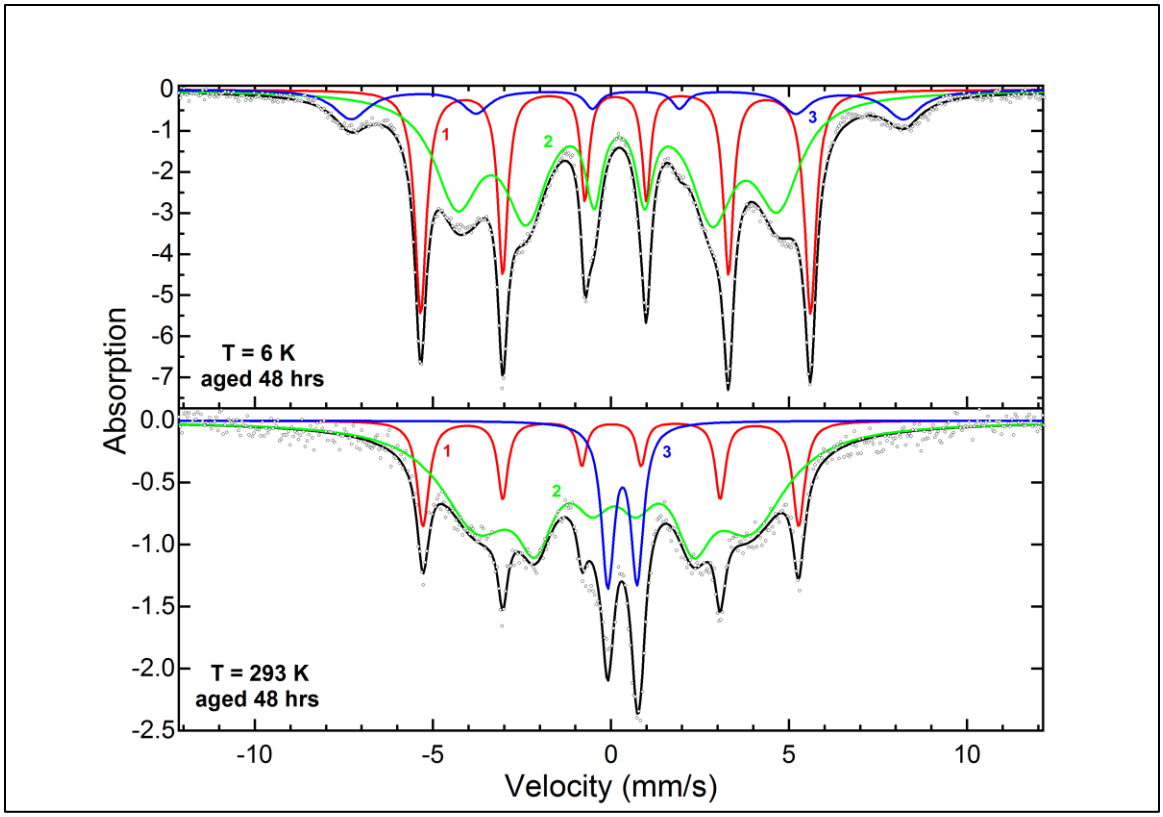


Figure A58. Stacked ^{57}Fe Mössbauer spectra of 48-hour oxidized AE007 metallic iron nanoparticles, measured at 6K and 293K

Table A31. Values of hyperfine parameters derived from fitting AE007 48-hour oxidized metallic iron nanoparticles at 6K and 293K. B_{hf} is the hyperfine magnetic field, δ is the isomer shift, ΔE_Q is the quadrupole splitting, and Γ is the linewidth (FWHM). Typical errors are ±0.5 mm/s for B_{hf}, ±0.02 mm/s for δ, ΔE_Q, and Γ and ±3% for relative area

Sample	Component	B_{hf} (T)	δ (mm/s)	ΔE_Q (mm/s)	Γ (mm/s)	Relative area (%)	Attribution
AE007 48 hr 6K	1	33.9	0.13	0.00	0.39	29	α-Fe
	2	27.9	0.21	-0.05	1.56	61	amorphous ZVI
	3	48.1	0.58	-0.24	1.18	10	Fe^{3+} oxides
AE007 48 hr 293K	1	32.7	0.00	-0.02	0.41	15	α-Fe
	2	23.7	0.09	-0.01	2.52	73	amorphous ZVI
	3	-	0.32	0.83	0.43	12	Fe^{3+} oxides

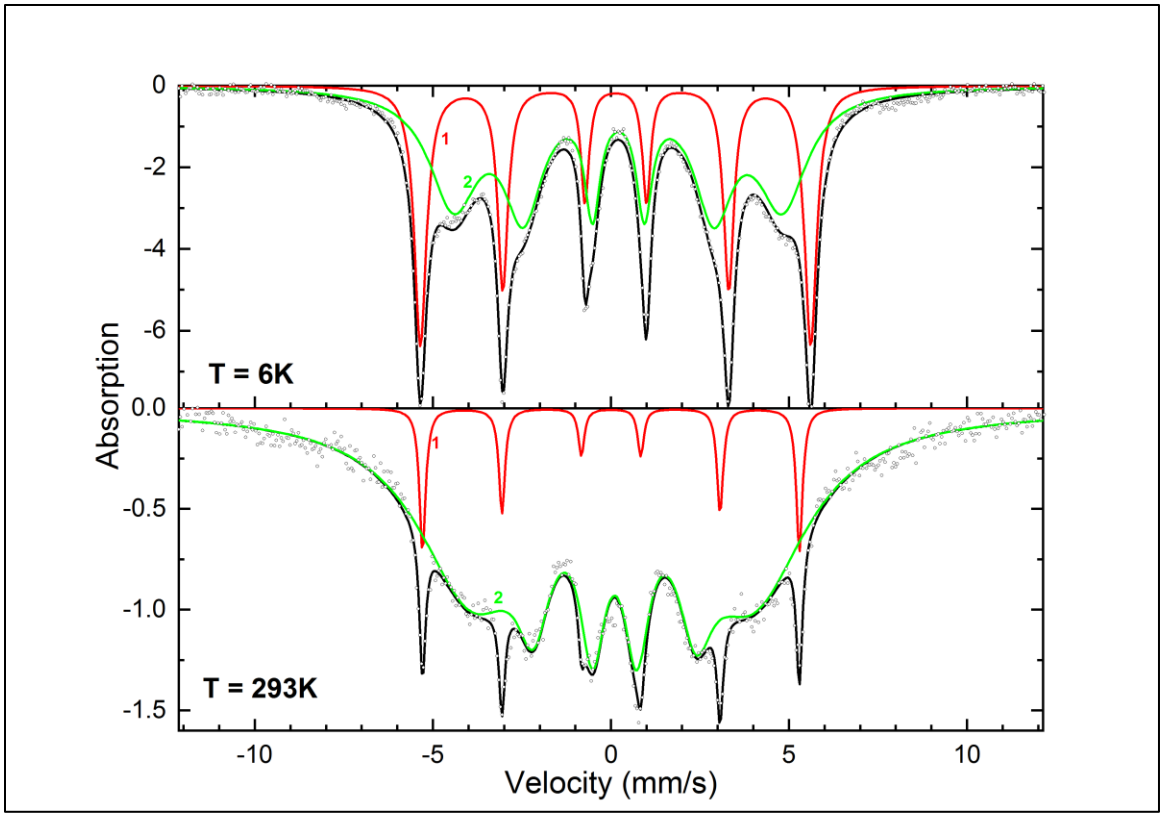


Figure A59. Stacked ^{57}Fe Mössbauer spectra of AE008 uncoated metallic iron nanoparticles, measured at 6K and 293K

Table A32. Values of hyperfine parameters derived from fitting as-made AE008 uncoated metallic iron nanoparticles at 6K and 293K. B_{hf} is the hyperfine magnetic field, δ is the isomer shift, ΔE_Q is the quadrupole splitting, and Γ is the linewidth (FWHM). Typical errors are ±0.5 mm/s for B_{hf}, ±0.02 mm/s for δ, ΔE_Q, and Γ and ±3% for relative area

Sample	Component	B_{hf} (T)	δ (mm/s)	ΔE_Q (mm/s)	Γ (mm/s)	Relative area (%)	Attribution
AE008 6K	1	34.0	0.13	0.00	0.41	34	α-Fe
	2	28.6	0.20	-0.01	1.67	66	amorphous ZVI
AE008 293K	1	32.8	0.00	0.00	0.21	6	α-Fe
	2	24.4	0.07	-0.06	3.75	94	amorphous ZVI

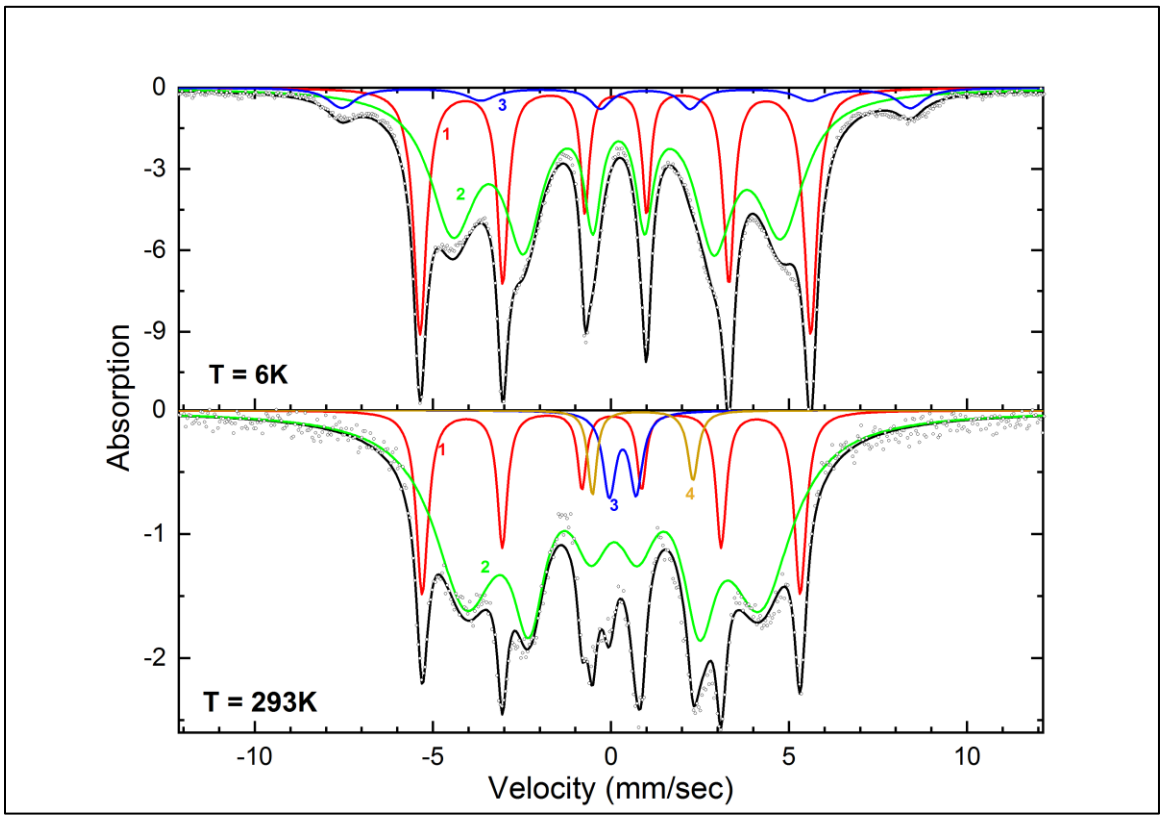


Figure A60. Stacked ^{57}Fe Mössbauer spectra of AE011 uncoated metallic iron nanoparticles, measured at 6K and 293K

Table A33. Values of hyperfine parameters derived from fitting as-made AE011 uncoated metallic iron nanoparticles at 6K and 293K. B_{hf} is the hyperfine magnetic field, δ is the isomer shift, ΔE_Q is the quadrupole splitting, and Γ is the linewidth (FWHM). Typical errors are ±0.5 mm/s for B_{hf}, ±0.02 mm/s for δ, ΔE_Q, and Γ and ±3% for relative area

Sample	Component	B_{hf} (T)	δ (mm/s)	ΔE_Q (mm/s)	Γ (mm/s)	Relative area (%)	Attribution
AE011 6K	1	34.0	0.13	-0.01	0.44	30	α-Fe
	2	28.6	0.19	-0.04	1.56	64	amorphous ZVI
	3	49.5	0.69	-0.54	0.93	6	Fe^{3+} oxides
AE011 293K	1	33.0	0.02	-0.02	0.41	16	α-Fe
	2	25.7	0.08	-0.03	2.20	77	amorphous ZVI
	3	-	0.34	0.76	0.43	4	Fe^{3+} oxides
	4	-	0.90	2.84	0.36	3	$Fe2^{+}$ impurities

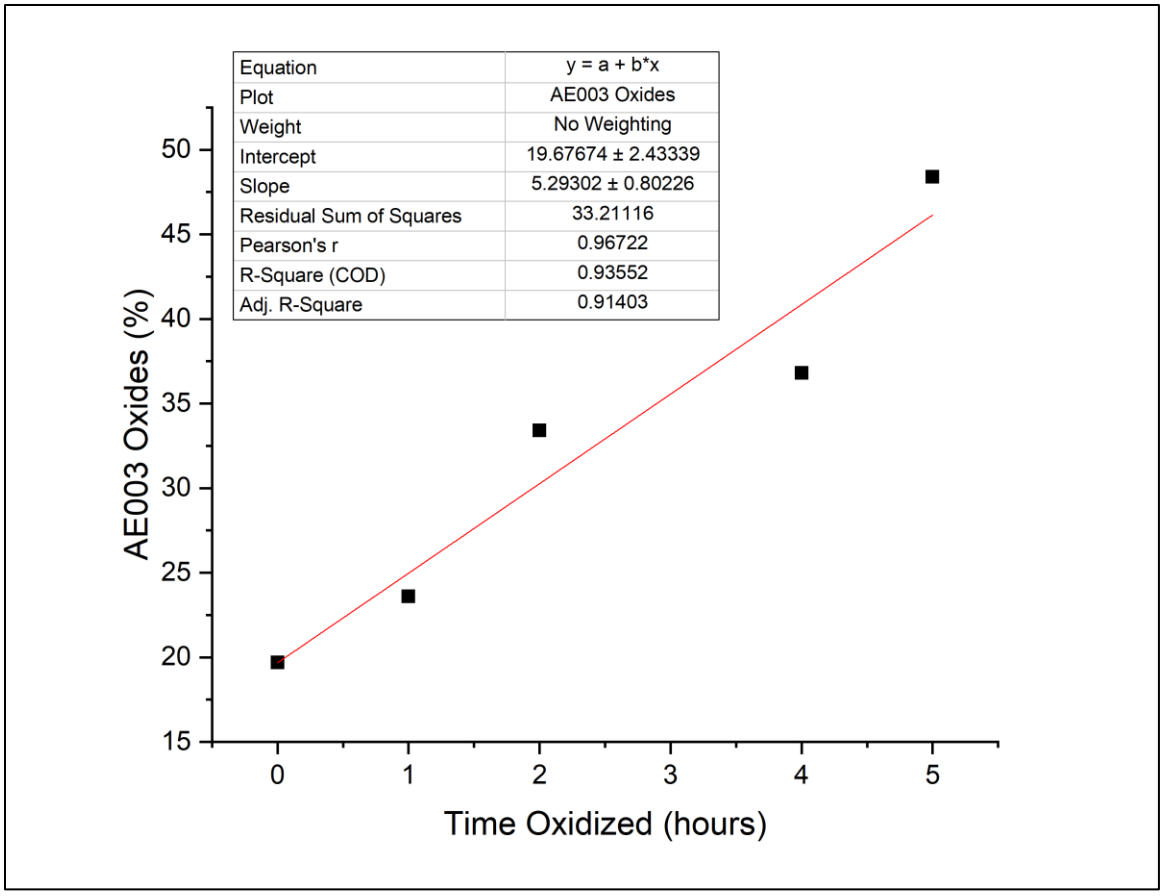


Figure A61. Oxidation rate of AE003 calculated through linear fit of oxide percentage over time. Oxidation rate was found to be 5.3%/hour

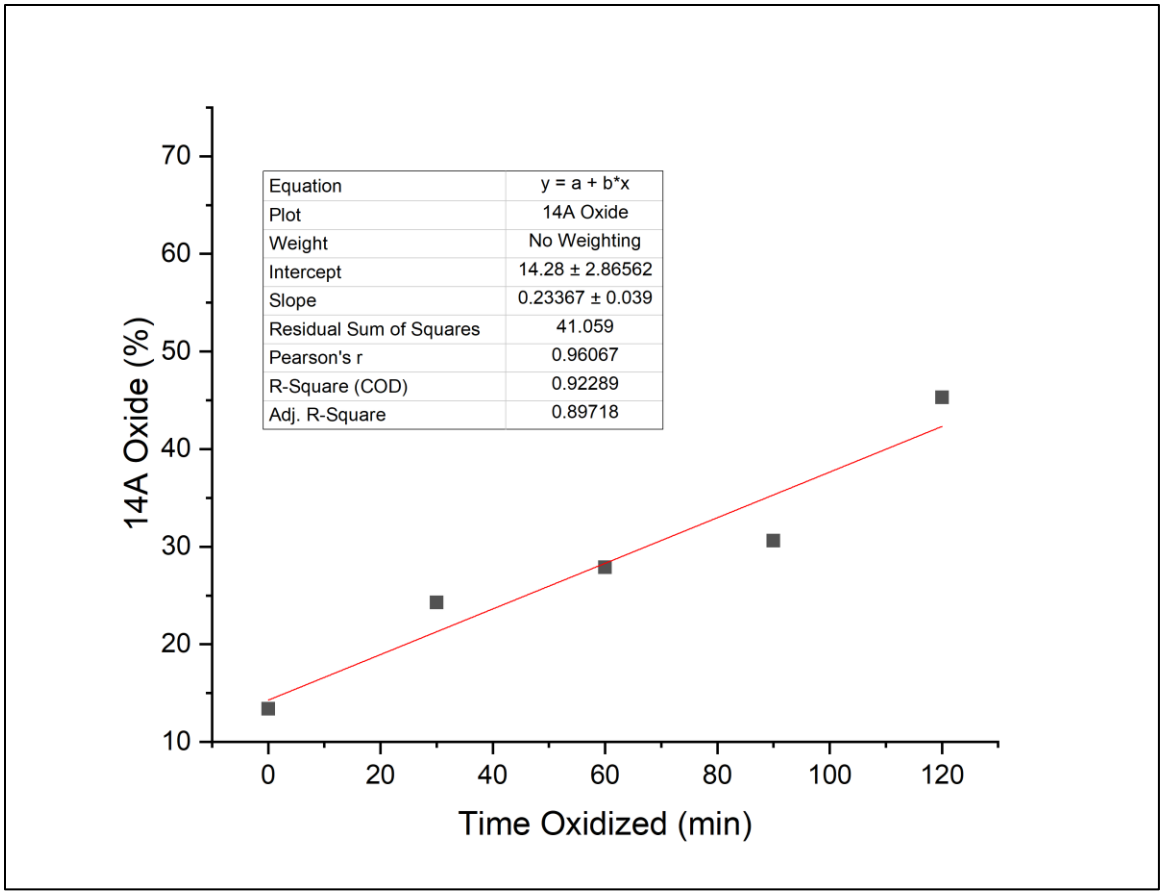


Figure A62. Oxidation rate of AE014A calculated through linear fit of oxide percentage over time. Oxidation rate was found to be 7%/30-min, 14%/hour

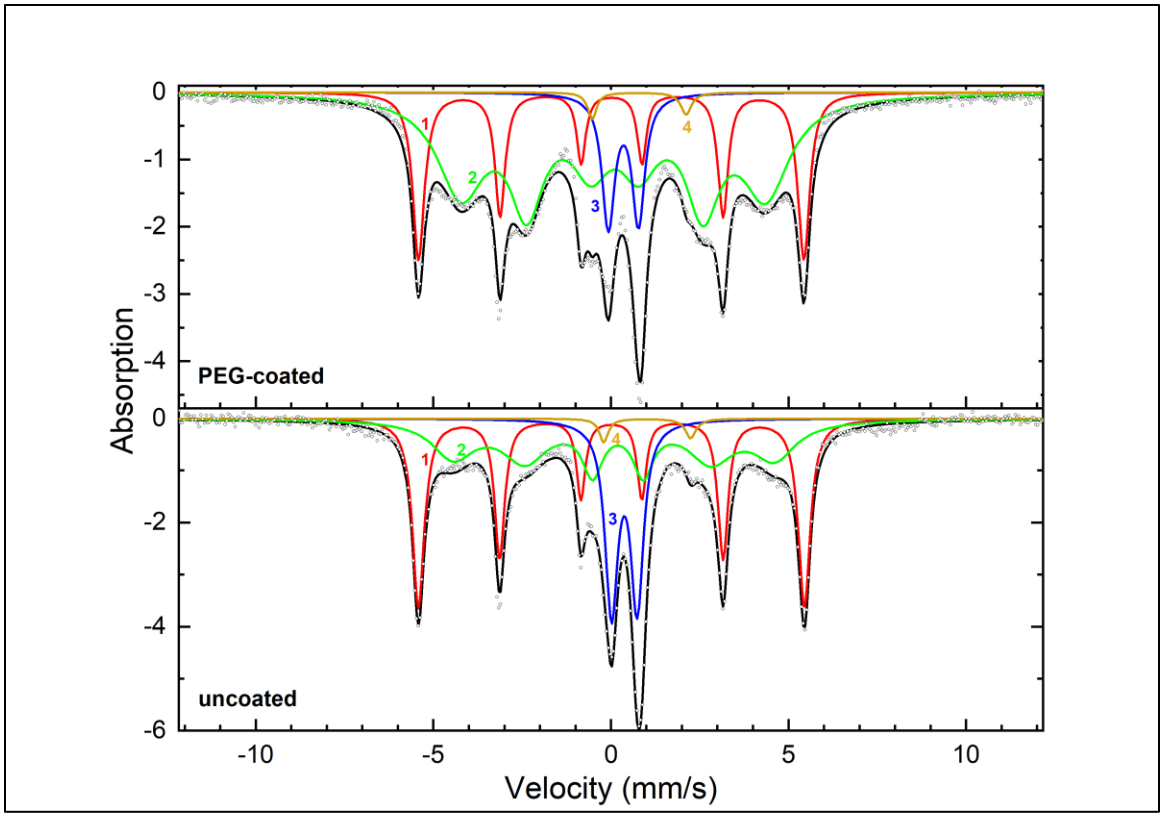


Figure A63. Stacked ^{57}Fe Mössbauer spectra of as-made PEG-coated (AE013A) and uncoated (AE013B) metallic iron nanoparticles, measured at 293 K

Table A34. Values of hyperfine parameters derived from fitting as-made AE013A PEG-coated and as-made AE013B uncoated metallic iron nanoparticles. B_{hf} is the hyperfine magnetic field, δ is the isomer shift, ΔE_Q is the quadrupole splitting, and Γ is the linewidth (FWHM). Typical errors are ±0.03 mm/s for B_{hf}, ±0.02 mm/s for δ, ΔE_Q, and Γ and ±3% for relative area

Sample	Component	B_{hf} (T)	δ (mm/s)	ΔE_Q (mm/s)	Relative area (%)	Attribution
PEG-coated	1	33.6	0.01	-0.01	23	α-Fe
	2	26.6	0.09	-0.04	65	small ZVI NP
	3	-	0.35	0.85	10	Fe^{3+} oxides
	4	-	0.79	2.65	2	Fe^{2+} impurities
uncoated	1	33.7	0.01	-0.02	38	α-Fe
	2	28.1	0.14	-0.11	39	small ZVI NP
	3	-	0.38	0.73	21	Fe^{3+} oxides
	4	-	1.02	2.45	2	Fe^{2+} impurities

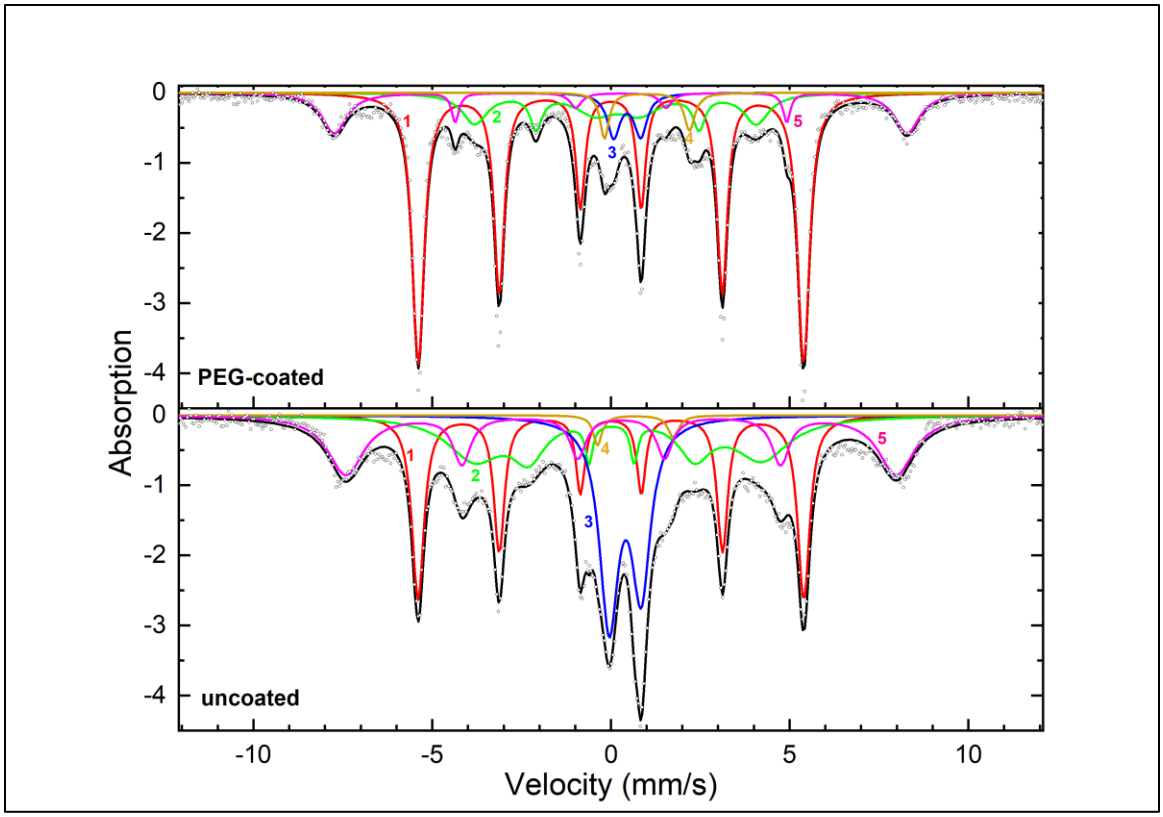


Figure A64. Stacked ^{57}Fe Mössbauer spectra of PEG-coated (AE013A) and uncoated (AE013B) metallic iron nanoparticles after one hour ambient oxidation, measured at 293 K

Table A35. Values of hyperfine parameters derived from fitting AE013A PEG-coated and uncoated metallic iron nanoparticles after one hour of ambient oxidation. B_{hf} is the hyperfine magnetic field, δ is the isomer shift, ΔE_Q is the quadrupole splitting, and Γ is the linewidth (FWHM). Typical errors are ±0.03 mm/s for B_{hf}, ±0.02 mm/s for δ, ΔE_Q, and Γ and ±3% for relative area

Sample	Component	B_{hf} (T)	δ (mm/s)	ΔE_Q (mm/s)	Relative area (%)	Attribution
PEG-coated	1	33.4	0.00	0.00	60	α-Fe
aged 1-hr	2	24.4	0.16	-0.06	18	small ZVI NP
	3	-	0.45	0.76	5	Fe^{3+} oxides
	4	-	1.01	2.38	4	Fe^{2+} impurities
	5	49.7	0.28	0.00	13	γ-Fe_2O_3
uncoated	1	33.4	0.00	0.00	28	α-Fe
aged 1-hr	2	24.9	0.11	0.19	25	small ZVI NP
	3	-	039	0.90	22	Fe^{3+} oxides
	4	-	0.69	2.12	2	Fe^{2+} impurities
	5	47.8	0.28	0.00	23	γ-Fe_2O_3

VITA

Adam Wesley Evans was born in Knoxville, Tennessee on June 30, 1990 to Steve and Pansie Evans. He was raised in Knoxville, where he graduated from Bearden High School in 2009. He graduated from the University of Tennessee, Knoxville with a Bachelor of Science Degree in Biomedical Engineering in 2013. After a gap year, Adam began his post-baccalaureate education at the University of Tennessee Space Institute in 2014. He received a Master of Science Degree in Biomedical Engineering in 2016 and continued to work toward his Doctor of Philosophy Degree in Biomedical Engineering at the same institution.